UNIVERSITY OF EXETER

Hand in Hand Tropical Cyclones and Climate Change: Investigating the Response of Tropical Cyclones to the Warming World

by

Kopal Arora

A thesis submitted in partial fulfillment for the degree of
Master of Philosophy in Mathematics

in the
Faculty of Mathematics
College of Engineering, Mathematics and Physical Sciences

12 February 2018

Declaration of Authorship

"Hand in Hand Tropical Cyclones and Climate Change: Investigating the Response of Tropical Cyclones to the Warming World" is submitted by Kopal Arora, to the University of Exeter as a thesis for the degree of Master of Philosophy, submitted on October 29, 2018, for examination.

This thesis is available for Library use on the understanding that it is copyright material and that no quotation from the thesis may be published without proper acknowledgement.

I certify that all material in this thesis which is not my own work has been identified and that no material has previously been submitted and approved for the award of a degree by this or any other University.

Signed:

Date:
October 29, 2018

UNIVERSITY OF EXETER

Abstract

Faculty of Mathematics
College of Engineering, Mathematics and Physical Sciences

Master of Philosophy in Mathematics

by Kopal Arora

What are the primary factors governing Tropical Cyclone Potential Intensity (TCPI) and how does the TCPI vary with the change in CO_2 concentration are the two fundamental questions we investigated here.

In the first part, a strong spatial correlation between the TCPI and the ocean temperature underneath was used to develop a statistical model to quantify the TCPI over the remote regions where the TC related observations are difficult to acquire. The model revealed an overall increase in the TCPI when the atmospheric CO_2 concentration was doubled.

Finally, the study examines the TCPI's sensitivity on the ocean temperature (at the spatial scales). Two independent models (HADCM3 from Met Office, UK and GFDL-CM3 from GFDL, NOAA, USA) on an average reveals an increase in the TCPI between 8 to 10 m/s per unit increase in the ocean temperature (in ^oC).

The key finding to emerge from this study is that the increase in the TCPI responds comparatively weakly to the increasing ocean temperature when CO_2 amount is increased. We call this observation as, "the sensitivity saturation effect".

According to our findings, the TCPI responds weakly (become less sensitive) to the ocean temperature on doubling the CO_2 concentration. This effect was observed in all the ocean basins and in both the considered climate models. Though the TCPI show a rise on increasing the CO_2 concentration but, its response to the SST decreases. This observation leads to a set of next level questions for instance, will there be a sensitivity saturation effect, analogous to the well-known "Band Saturation effect", on increasing the CO_2 levels and if it does, will the TCPI's sensitivity plateau? If it plateaus, at what cut-off CO_2 levels would that happen? These emerging questions open up a new area of investigation for the climatologists and the enthusiasts in the related fields.

In this manner, this part of the research provides a framework for the future exploration of the subject.

Acknowledgements

Firstly, I would like to express my gratitude to my advisors, Prof. Matthew Collins and Prof. David Stephenson for their continuous support. I am grateful to my academic mentor, Dr Chris Ferro for his insightful suggestions and encouragement throughout the endeavour.

The highest thanks and praise to my mother Mrs Sneh Arora, the most inspirational person I've ever met. My deepest gratitude to my father, Late Mr Surendra Arora for his everlasting encouragement. I am deeply grateful to my siblings, Sachin and Anshuman for their support and encouragement. My heartfelt appreciation goes to my husband, Abhinav Sharma, for his support, understanding and patience throughout this long process.

A very special gratitude goes out to my friend, Dr Prasanjith Dash (from NOAA) for sharing his insightful knowledge and experience on the subject and extending his warm encouragement and constructive comments.

A warm thanks to my lovely friends from Church, Ruth, Christopher, Dorothy and Rachael for their moral and emotional support during my stay in Exeter.

I particularly like to thank Chinna, Deepthi & jagadish (Reading), Asmi, Haroon, Shalini, Madhav, Harish, Varun and Anusha for making my stay in U.K. pleasant and lively.

A special thanks to my colleagues and students at, INTO, Exeter. This is where I spent my spare time very productively.

And finally, last but by no means least, I owe my deepest gratitude to my office colleagues for making the place delightful.

Contents

Declaration of Authorship i

Abstract ii

Acknowledgements iv

List of Figures ix

List of Tables xiv

1 Introduction and Motivation 1
- 1.1 Introduction and Motivation . . . 1
  - 1.1.1 Challenges . . . 3
  - 1.1.2 Classification . . . 4
  - 1.1.3 Formation . . . 4
    - 1.1.3.1 Metrics for Intensity . . . 5
- 1.2 Effects of Tropical Cyclones on climate . . . 5
    - 1.2.0.1 Tropical Cyclogenesis . . . 5
  - 1.2.1 Warm ocean temperature, above 26.5 °C, extended 50 meters deep . . . 6
  - 1.2.2 Sufficient humidity in the troposphere . . . 7
- 1.3 Quantifying Tropical Cyclone Intensity Using Emanuel's Approach . 8
  - 1.3.1 Thesis Aims and Outline . . . 17

2 Methodology and Data Used 22
- 2.1 Model Output . . . 22
  - 2.1.1 Global Climate Model (GCM) an Introduction and Model Physics . . . 23
  - 2.1.2 GCMs and Tropical Cyclones . . . 24
  - 2.1.3 Perturbed Physics Ensembles (PPE) and Multi Model Ensembles (MME) Explained . . . 24
- 2.2 Observational Data . . . 25

2.2.1 IBTrACS Data 25
2.2.1.1 Advantages and Limitations of IBTrACS Dataset . 25
2.3 HadISST Dataset 26
2.3.0.1 Data Assimilation Technique, HadISST 26
2.3.0.2 Strengths and Weaknesses of HadISST Dataset . . 26
2.3.0.3 Climate Model Intercomparison Project version-5 (CMIP5) Dataset 27
2.3.1 Atmospheric Reanalysis Dataset 28
2.4 Tropical Cyclone Scales 28
2.5 Methods Applied 32
2.5.1 Pearson's Correlation coefficient and Bootstrap Methods . . 32
2.5.2 Regression Analysis 33
2.5.3 Partial Least Square Regression 34
2.5.3.1 Goals of partial least square regression 35
2.5.3.2 Simultaneous decomposition of predictors and dependent variables 36
2.5.4 Ensemble Empirical Mode Decomposition (EEMD) 36
2.5.5 Bilinear Interpolation 38

3 Simple Methods for Estimating Tropical Cyclone Intensities 40
3.1 Introduction 40
3.1.1 Modeling TC Intensification 41
3.2 Theoretical Background: A steady state analytical TC model 44
3.3 Data and Methods Used 46
3.3.1 Methodology 46
3.3.1.1 Similarity and Differences between COBE and ERSST.V3b 47
3.3.1.2 Computation of sustained wind speeds 48
3.3.2 Data Used 49
3.3.3 Tropical Distribution of SST From Three Different Datasets 51
3.4 Results and Discussion 52
3.4.1 Development of a linear V_{max} Model and its validation against an established model 52
3.5 Spatial Distribution of SST 58
3.6 Model Verification: ACE vs V_{maxNw} 59
3.7 Model Limitation and Possible Explanation 61
3.8 Summary and Conclusions 63

4 Saturation of Tropical Cyclone Strength under a doubled CO_2 scenario 66
4.1 Introduction 67
4.2 Data and Methods Used 70
4.2.1 Data Used 70
4.2.1.1 UKMO's HadCM3 70
4.2.1.2 GFDL's ESM-CM3 73
4.2.2 Methodology 74

4.2.2.1 Partial Least Square Regression (PLSR) 74
4.2.2.2 Sensitivity Analysis 76
4.3 Results and Discussions 77
4.3.1 Analysis Using Partial Least Square Regression 77
4.3.2 Analysis Using Histograms 80
4.3.2.1 Histogram of sensitivity to V_{max} in the Tropical Ocean Basin 81
4.3.2.2 Histogram of sensitivity to V_{max} in the North Indian Ocean 82
4.3.2.3 Histogram of sensitivity to V_{max} in the South Indian Ocean 82
4.3.2.4 Histogram of sensitivity to V_{max} in the Northwest Pacific Ocean 83
4.3.2.5 Histogram of sensitivity to V_{max} in the Northeast Pacific Ocean and North Atlantic Ocean 85
4.3.3 Sensitivity Analysis 88
4.3.4 Detailed Explanation of the Tables from Sensitivity Analysis section: 90
4.4 Conclusions 92
4.5 Weakness and Limitations 93

5 Summary, Conclusions and Recommendations 95
5.1 Introduction 95
5.2 The Questions 96
5.3 The Answers 97
5.4 Limitations & Prospective Suggestions 99
5.5 Contributions 100

A Supplimentary Figures, Tables and Explanations 102
A.1 Chapter 3 102
A.1.1 Dependence of V_{max} on SST and AT 102
A.1.2 Computing V_{maxNw} using SST 104
A.1.3 Application of Linear Model Outputs to HadCM3 Model . . 105
A.1.4 Understanding the role of Sustained Wind Speed through Enthalpy 109
A.1.5 Potential of SST Alone in Describing TC Potential Energy . 113
A.2 Model application on temporal resolution 114
A.2.1 Patterns in the V_{maxNw} 115
A.2.1.1 North Indian Ocean 115
A.2.1.2 South West Pacific Ocean 115
A.2.1.3 North Atlantic Ocean 115
A.2.1.4 Northwest Pacific 116
A.2.1.5 Southern Indian Ocean 116

A.2.2 Time series trends 116
A.2.2.1 North Indian Ocean 116
A.2.2.2 South West Pacific 116
A.2.2.3 North Atlantic Ocean 117
A.2.2.4 North West Pacific 117
A.2.2.5 South Indian Ocean 117
A.3 Supplementary Figures from time series analysis 118

Bibliography **128**

List of Figures

1.1 Figure depicts recognized distribution of TC tracks from 1851 to 2006 (Image courtesy NASA). 2
1.2 Mature TC as a Carnot Heat Engine. Source: Divine Winds by K. Emanuel. Colours, in the figure above, represents entropy distribution where cooler colours signify low entropy and warm shades shows higher entropy.(Figure courtesy: Emanuel, 1986) 11
1.3 Hurricane Structure. Source: COMET Program (COMET [2011]) . 17
1.4 Hurricane Structure. Source: The COMET program (COMET [2011]) 18

2.1 Processes and interactions involved in the global climate system (Courtesey Treut et al. [2007]) 23

3.1 Methodology to compute spatial distribution (gridded) of V_{maxNw} from SST (gridded). 47
3.2 Tropical distribution of monthly mean SST. The SST values are averaged between 1982 (January) through 2013 (December). Tropical distribution of SST is obtained from $ERSST.V3b$ dataset(Smith et al. [2007]) 48
3.3 Departure of SST.COBE data set from SST.V3b. On an average, SST.V3b shows lower temperature than the SST.COBE data with a few exceptions in the North Atlantic and the West Pacific. 49
3.4 Departure of OISST.V2 data set from SST.V3b. On an average, SST.V3b and SST data sets presents similar values, with a few exceptions in the North Atlantic and the West Pacific. 50
3.5 Spatial distribution of the difference between the peak winds speeds as derived from thermodynamical model and that obtained from the linear statistical model developed here. (Using SST.V3b) 51
3.6 Tropical distribution of SST from COBE dataset (COBE-NOAA [2015]) 51

3.7 Comparison of cyclone wind speed V_{max} obtained from Emanuel's model and our simplistic empirical approach with only SST as input. Row-1: V_{max} employing Emanuel's model with reanalysis datasets as inputs: SLP, specific humidity and atmospheric temperature profile and ERSST.V3B (SST); Row-2: V_{maxNw} employing our approach (Equation 3) with ERSST.V3b (SST); Row-3: Spatial distribution of V_{maxNw} minus V_{max} to visually identify areas of disagreement, considering V_{max} as a benchmark (reference), Row-4: Probability density function (PDF) of 'δ V_{max} = V_{maxNw} - V_{max}'. Statistical parameters (number of V_{max} matches, minimum, maximum, mean, standard deviation, root mean square difference), a Gaussian fit, X N(mean, Std Dev) and number of grids beyond " Mean ± 4xStd Deviation", henceforth called 'extreme grids', are also annotated on the PDF. 55

3.8 Standardized variation of ACE and V^2_{maxNw} between 1970 through 2017 (X-axis). The overall correlation between the ACE and V^2_{maxNw} can be seen in the table, 3.2. The two signals vary comparatively closely in the North Atlantic, North Indian Ocean and the Southern Hemisphere. 60

3.9 Spatial distribution of the difference of SST and AT at lowest layer of the atmosphere. Considered regions, where the model fails are indicated with an outline. 63

4.1 Graph shows comparison of SST spread as obtained from reanalysis (panel (a)) and that obtained from model runs ((b)-(h)). 72

4.2 The figure illustrates PLSR method. X and Y are decomposed into their principal components (Xs and Ys) and loading matrices (P,Q) along with their corresponding error matrices (E,F). The correlation and hence the inner relationship between the scores (Xs & Ys) is stated as, "inner-relationship" ($Ys = B * Xs$) in the figure. 76

4.3 A Schematic representation of the methodology to compute ΔV. . 79

4.4 A Schematic representation of the methodology to compute ΔV under present and doubled CO_2 concentration. 80

4.5 Under present day CO_2 scenario, change in maximum wind speed, V_{max}, on increased SST by 1 °C averaged over tropics is highest between the range of $8.5ms^{-1}$ to 10.6 ms^{-1}, which is significantly high (at 5% significance level). 81

4.6 Histogram of ΔV as response to 1 °C rise in SST. Y-axis denotes the number of grid points possessing ΔV demarcated on abscissa. On an average, increase in V_{max} as response to increase in SST by 1 °C is 9 (ms^{-1}). 83

4.7 Histogram representing ΔV in Northwest Pacific Ocean as a result to 1 °C rise in SST. Ordinate denotes the number of grid points possessing ΔV demarcated on X-axis. In Northwest Pacific, all the ΔV values are above 7 (ms^{-1}) with expected increase in ΔV on increasing SST by 1 °C to be 8.4 (ms^{-1}). 83

4.8 In Northeast Pacific, distribution of ΔV in Northeast Pacific Ocean is far from Gaussian and it also appears that it is a bimodal distribution. Bimodal characteristic in the distribution is indicative of two merged distributions. The two distributions could be due to overlapping of two ocean basins prone to tropical cyclone formation giving rise to two distributions of ΔV, one corresponding to each basin. V_{max} increase by 8.4 (ms^{-1}) in Northeast Pacific Ocean as response to 1 °C upswing in SST. 84
4.9 Histogram of ΔV in North Atlantic Ocean as a response to 1 °C rise in SST. Y-axis denotes the number of grid points possessing ΔV demarcated on X-axis. In North Atlantic Ocean, all the ΔV values are above 9 (ms^{-1}). This distribution is very close to Gaussian with kurtosis of 3.1. 84
4.10 Histogram of ΔV in South Indian Ocean as a response to 1 °C rise in SST. Y-axis denotes the number of grid points possessing ΔV demarcated on the abscissa. In South Indian Ocean, increase in ΔV ranges between 0 to 14 (ms^{-1}). This distribution show even arrangement of ΔV values across the bins (X-axis values) between 0 to 13 (ms^{-1}). Average increase in ΔV over South Indian Ocean is 11 ms^{-1}. 86
4.11 Histogram of ΔV in Southwest Pacific Ocean as a response to 1 °C rise in SST. Y-axis denotes the number of grid points possessing ΔV demarcated on X-axis. Typical increase in ΔV over Southwest Pacific Ocean is 9.8 (ms^{-1}). 86
4.12 The figure illustrates scatter plots between TCPI and four input variables, SST, MR, SLP, and AT. The figure indicates a better connection between TCPI and SST (panel 1) as compared to other variables. 90

A.1 Change in tropical cyclone wind speeds, V_{max}, on doubling CO_2 scenario 107
A.2 Tropical spread of SST, from $SST - OI$ dataset(NOAA [2014]) . . 107
A.3 Comparison of the Cyclone wind speed, V_{max} and V_{maxNew} as, obtained from reanalysis datasets; ERSST-V3b (SST), SLP, Specic Humidity & Atmospheric temperature profile. The Modeled tropical cyclone wind speed, VmaxNew, w.r.t. ERSST-V3b (SST), as input to Eq(3.5). Peak wind speed distribution as derived from an algorithm based on thermodynamics and that obtained from our simple linear model match well in tropics. 108
A.4 Cyclone wind speed, V_{max}, obtained from reanalysis datasets; OI.SST (SST) (NOAA [2014]), SLP, Specific Humidity & Atmospheric temperature profile. Modeled cyclone wind speed, V_{maxNew}, as obtained from OI.SST (SST) dataset(NOAA [2014]) 108

A.5 Comparison of cyclone wind speed V_{max} obtained from Emanuel's model and our simplistic empirical approach with only SST as input. Row-1: V_{max} employing Emanuel's model with reanalysis datasets as inputs: SLP, specific humidity and atmospheric temperature profile and COBE SST; Row-2: V_{maxNew} employing our approach (Equation 3) with COBE SST; Row-3: Spatial distribution of V_{maxNew} minus V_{max} to visually identify areas of disagreement, considering V_{max} as a benchmark (reference), Row-4: Probability density function (PDF) of 'δ V_{max} = V_{maxNew} - V_{max}'. Statistical parameters (number of Vmax matches, minimum, maximum, mean, standard deviation, root mean square difference), a Gaussian fit, X N(mean, Std Dev) and number of grids beyond " Mean ± 4*Std Deviation", henceforth called 'extreme grids', are also annotated on the PDF. 109

A.6 Comparison of cyclone wind speed V_{max} obtained from Emanuel's model and our simplistic empirical approach with only SST as input. Row-1: V_{max} employing Emanuel's model with reanalysis datasets as inputs: SLP, specific humidity and atmospheric temperature profile and OISST.V2 (SST); Row-2: V_{maxNew} employing our approach (Equation 3) with OISST.V2 (SST); Row-3: Spatial distribution of V_{maxNew} minus V_{max} to visually identify areas of disagreement, considering V_{max} as a benchmark (reference), Row-4: Probability density function (PDF) of 'δ V_{max} = V_{maxNew} - V_{max}'. Statistical parameters (number of Vmax matches, minimum, maximum, mean, standard deviation, root mean square difference), a Gaussian fit, X N(mean, Std Dev) and number of grids beyond " Mean ± 4xStd Deviation", henceforth called 'extreme grids', are also annotated on the PDF. 110

A.7 SST errors in HadCM3 as when compared with ERA-15 (annual mean), Courtsey: Connolley [June, 2005] 111

A.8 Cyclone wind speed, V_{max}, obtained from reanalysis datasets; COBE (SST), SLP, Specific Humidity & Atmospheric temperature profile (COBE-NOAA [2015]) and the Modeled tropical cyclone wind speed, V_{maxNew}, w.r.t. COBE (SST) (COBE-NOAA [2015]), as input to Eq.(3.5). Peak wind speed distribution as derived from algorithm based on thermodynamics and that obtained from our simple linear model matches well. 111

A.9 Control experiment with changing only SST values and keeping other variables constant (Fig 1b, Fig 2b) and the case when both, SST and AT varies while keeping rest of the input variables unchanged (Figure (A.9(a)), Figure (A.9) 2a) for both, 1X, 2XCO_2 scenarios 114

A.10 Wavelet power spectrum of VmaxNew in the North Indian Ocean highlighting temporal patterns of occurrence of maximum wind speeds. 117

A.11 Wavelet power spectrum of VmaxNew in the South West Pacific Ocean highlighting temporal patterns of occurrence of maximum wind speeds. 118
A.12 Wavelet power spectrum of VmaxNew in the North Atlantic Ocean highlighting temporal patterns of occurrence of maximum wind speeds. 118
A.13 Wavelet power spectrum of VmaxNew in the North West Pacific Ocean highlighting temporal patterns of occurrence of maximum wind speeds. 119
A.14 Same as in Figure (A.13) but for the Southern Indian Ocean. 119
A.15 Time series of Simulated TC wind speed VmaxNew in the North Indian Ocean 120
A.16 Same as in Figure (A.15) but for the Southern West Pacific. 120
A.17 Time series of simulated TC wind speed VmaxNew in the North Atlantic Ocean 121
A.18 Time series of simulated TC wind speed VmaxNew in the North West Pacific Ocean 121
A.19 Time series of simulated TC wind speed VmaxNew in the South Indian Ocean 122
A.20 EEMD of the AT in the North Indian Ocean. 122
A.21 EEMD of the AT in the North West Pacific Ocean. 123
A.22 EEMD of the AT in the North Atlantic Ocean. 123
A.23 EEMD of the AT in the South Indian Ocean. 124
A.24 EEMD of the AT in the South West Pacific Ocean. 124
A.25 EEMD of the MR in the North Indian Ocean. 125
A.26 EEMD of the MR in the North West Pacific Ocean. 125
A.27 EEMD of the MR in the North Atlantic Ocean. 126
A.28 EEMD of the MR in the South Indian Ocean. 126
A.29 EEMD of the MR in the South West Pacific Ocean. 127

List of Tables

1.1 Assumptions, working mechanism, similarities, and differences of CISK and WISHE theories.(Image source - Comet programme: http://comet.ucar.edu/) 20
1.2 Summary of the primary TC genesis parameters 21

3.1 Summary and intercomparison of tropical cyclone wind speed obtained from Emanuel's model and our approach with only SST as input. Comparisons are performed for three different SST inputs: SST.COBE, ERSST.V3b and OISST.V2. Other parameters (SLP, specific humidity, atmospheric temperature profile) required for implementing Emanuel's model are from NCEP reanalysis datasets. . 58
3.2 Pearson's moment correlation coefficients (r) between the observed index, ACE, ${V_{max}}^2$ and ${V_{maxNw}}^2$. ACE, which is traditionally documented in units of $Knots^2$ has been changed to $(ms^{-1})^2$ by taking its product with the factor of 0.544^2 to match the units of ${V_{maxNw}}^2$ and ${V_{max}}^2$. The indices are considered over the North Indian Ocean, North Atlantic, Northwest Pacific and Southern Hemisphere. The reasonable correlation between the observed and the theoretical parameters proliferate our confidence in the usability of the model. The table compares the correlation coefficients of the observed seasonal ACE data with the V^2_{maxNw} and ${V_{max}}^2$ 61
3.3 Convective heat rate at the 5 regions where the V_{maxNw} failed . . . 63

4.1 Pearson moment correlation coefficients (r) and coefficient of determination (r^2) between SST from reanalysis and HadCM3's ensemble members. The Higher correlation coefficient between the reanalysis and the model parameters increase our confidence considering the later for our analysis. 72
4.2 PLSR coefficients (β) corresponding to SST, SLP, mixing ratio (lowest level), and AT (lowest level) from reanalysis and model (HadCM3) datasets 78
4.3 Pearson's Moment Correlation Coefficients between TCPI and SST, SLP, MR, & AT derived from model data (GFDL) under present day and doubled CO_2 scenario 80
4.4 Statistics of change in tropical cyclone 85
4.5 Statistics of change in tropical cyclone for doubled CO_2 scenario . . 87

4.6 The decrease in sensitivity of TC strength towards SST with increased CO_2 concentration. On an average, we can notice highest effect in North Indian Ocean and least in South Indian Ocean. North and Southwest Pacific add an exception to this, while the exception is quite small in the southern part of the West Pacific Ocean. Data used, **HadCM3, UK Met Office** 87
4.7 Table compares ΔV in six tropical oceans (averaged over equal areas), under present and doubled CO_2 concentrations. Lower values of ΔV represents the lower sensitivity of change in ΔV to a unit increase in SST. All the tropical ocean basins stated in the table above, North Indian Ocean, Northwest Pacific, North Atlantic Ocean, Northeast Pacific, South Indian Ocean, and Southwest Pacific, illustrates the reduced sensitivity of ΔV (towards SST) on doubling CO_2 concentration. Data used, **CMIP5, GFDL** 87
4.8 The table presents the Pearson's moment correlation coefficient (r) and the coefficient of determination (r^2) between TCPI and the four input variables (SST, SLP, MR, and AT, from reanalysis dataset). TCPI in the table above shows best connection with SST as compared with other three variables. This link can be visualised in the scatter plots between the same set of variables shown in the figure (4.12), which agrees with the values displayed in this table. 89
4.9 The table above illustrates the sensitivity of ΔV towards an increase in AT in tropics under present and doubled levels of CO_2. Where NIO refers to the North Indian Ocean, NWPC stands for Northwest PacifiC, NATL corresponds to North Atlantic Ocean, NEPC can be expanded as Northeast Pacific Ocean, SIO indicate South Indian Ocean, and SWPC represents Southwest Pacific Ocean 89
4.10 The table above illustrates the sensitivity of ΔV towards an increase in SLP in tropical ocean basins under present and doubled levels of CO_2. Where, NIO refers to the North Indian Ocean, NWPC stands for Northwest PacifiC, NATL corresponds to North Atlantic Ocean, NEPC can be expanded as Northeast Pacific Ocean, SIO indicate South Indian Ocean, and SWPC represents Southwest Pacific Ocean 89
4.11 Table above compares ΔV obtained from using perturbed model runs under present-day and doubled CO_2 amount. The ΔV values presented in this table are averaged over tropics. Individual oceans are also considered and are shown in other *e.g.* tables (4.12) which agree with the sensitivity saturation effect shown in the table above. 91
4.12 CMIP5 Dataset: Table above illustrates the sensitivity of ΔV towards an increase in SST in tropical ocean basins under present and doubled levels of CO_2. Where, NIO refers to the North Indian Ocean, NWPC stands for Northwest PacifiC, NATL corresponds to North Atlantic Ocean, NEPC can be expanded as Northeast Pacific Ocean, SIO indicate South Indian Ocean, and SWPC represents Southwest Pacific Ocen 91

*I dedicate this thesis to **my parents** who have been a great source of inspiration and support.*

Chapter 1

Introduction and Motivation

1.1 Introduction and Motivation

There are two popular methods used so far to compute TC intensification. First was proposed by Miller in 1958 (Miller [1958]) and Holland (Holland [1997a]) in 1996. The approach estimates the maximum temperature that can be achieved in the eye-wall of a tropical cyclone provided the thermodynamic properties of air near the sea surface are known.

Next step in the technique involves finding the maximum temperature that can be achieved in the tropical cyclone's eye by compressional warming of the sinking air. However, a second method, developed by Emanuel in 1995 (Emanuel [1986]) (Emanuel [1995]) uses energy cycle of a tropical cyclone to estimate the maximum surface wind speeds that could be achieved. The minimum achievable pressure in a cyclone is another measure of storm intensity. To compute the parameter we assume a particular radial profile of azimuthal wind inside the eye of the storm.

This work primarily focuses on sea surface temperature driven imperial strength that tropical cyclones (TC) possess and how is it they are impacted by humans since the advent of industrial era.

Climate models mostly continue to predict a decrease in the TC frequency and an increase in its intensities of stronger storms and the associated rainfall rates (Mendelsohn et al. [2012]). Sea level rise has been predicted to cause the inundation of low coastal areas (Walsh et al. [2015]). Increasing per capita income has

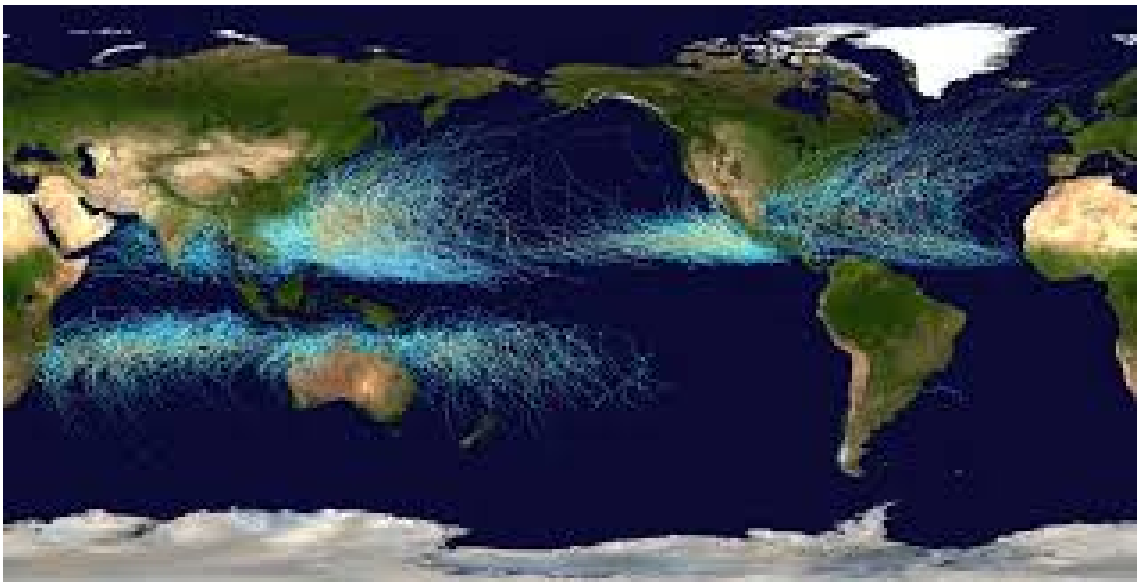

FIGURE 1.1: Figure depicts recognized distribution of TC tracks from 1851 to 2006 (Image courtesy NASA).

shown to cause increased losses due to TC related damage even without introducing the climate change into the picture. Climate change has shown to increase the intensity of storms and double the related damage (Mendelsohn et al. [2012]). This however depends on the model employed for the analysis and the TC regions, for example, North America, East Asia Carribean and Central America are subjected to doubled TC related losses (Mendelsohn et al. [January 2012]).

Tropical cyclones (TC) constitute an important component of the climate system and have an enormous effect on society and economies of tropical countries. Well-known TCs like, Tracy in Australia, Bhola in Bangladesh, Mitchell and Katrina in the Caribbean, Mexico, Central America and the US remind us of calamity influencing life and property throughout the globe. Loss of 81 to 82 billion dollars is estimated from hurricane Katrina in 2005 (Pielke et al. [2008]). The next hurricanes following similar losses are the triplet, Harvey, Irma and Jose (September 2017).
300,000 people died in a cyclone surge in Bangladesh in 1970. Increasing coastal population and construction with time ensures intense damage and losses from cyclones in future (Emanuel [2005a]).

The increase in the likelihood of hurricane intensification with the climate change has attracted much media attention. Hurricane "Sandy" (2012) had wind field of more than 100 miles/hr and is known to be one of the largest typhoon on record so far. A couple of intriguing questions then arising are about the likelihood of

observing more such storms in future. This study has been prompted by my natural interest as a climate student. In specific, the subject qualitatively and quantitatively draws my inclination towards the study of the influence of climate change on tropical cyclone intensity.

1.1.1 Challenges

Tropical cyclones are one of the most lethal natural phenomena that cause loss of life and property (Anthes [1982]). It is thus very important to issue an advance warning to the densely populated regions across the globe to ensure safer future of civilisation. The Indian subcontinent and the land in its vicinity situated in the Indian Ocean are heavily populated. This makes the region vulnerable to destruction by a natural catastrophe like TC. Thus, it is very important to provide adequate warning in this region and the regions alike. Regions prone to TC formation are shown in figure(1.1)). In order to produce reliable warnings, it is very important to understand tropical cyclone genesis, development, and the associated consequences. It is hypothesised, that climate change will influence tropical cyclones by increasing their intensity and the frequency of the intense storms. (Bister and Emanuel [1998], Evans and Watterson [1992]). According to a report on post-IPCC assessment, cyclone's Maximum Potential Intensity (MPI) will either continue to remain the same or show a moderate surge of about 10% to 20% (Henderson Sellers [1998]). The report also state that climate change will influence tropical cyclones by increasing their intensity but decreasing their frequency of occurrence.

This has resulted in increased attention towards cyclone genesis and warnings. The link between the climate change and tropical cyclones is of great practical importance (Henderson Sellers and Holbrook [2000]).
It is interesting to note that storm track forecast is the best predictable aspect of a TC these days but its intensity prediction is much more challenging. This is because the cyclone track is governed by larger scale motions in the atmosphere which have relatively much longer reliable predictability (NHC [2014]). Intensity forecast, on the other hand, depends upon small scales in the centre of the storm. It has been particularly difficult to observe early stages of hurricane development phase because of the region of their origin is far away from land. Even the observations from satellites are unable to decipher this aspect too well, as of now. The

US National Hurricane Center and few others are in the process to send aircraft loaded with modern equipment like radiosonde, microwave temperature profiler, over the ocean basins early enough to observe beginning stages of vortex formation in order to have this piece of information (NHC [2014]). However, due to technical constraints and hazardous nature of these, the success has been rather limited.

1.1.2 Classification

Technically, a whirlwind, rotating storm with horizontal scales of the order of 100 to 1000 Km extending through the troposphere to a depth of about 15 Km is known as a tropical cyclone (Emanuel [2005b]). Depending upon the 10-minute average sustained wind speed, tropical cyclones can be classified as a tropical depression, tropical storm, hurricane, typhoon or a tropical cyclone. The storms, reaching a maximum speed of about 16 m/s are known as tropical depressions. The ones attaining a maximum speed in the range of 17 m/s to 32 m/s, are classified as tropical storms. A storm sustaining a wind speed of 33 m/s or greater is defined as a hurricane when in the North Atlantic or North Pacific, as a typhoon when in the Northwest Pacific and a tropical cyclone in the Indian Ocean (Emanuel [2005b]).

1.1.3 Formation

A TC derives its energy from the latent heat liberated during condensation of water vapour in deep convective clouds. One of the striking difference between a TC and its extra-tropical counterparts is that TC is more axisymmetric, intense, and tend to live longer.

When oceans and seas get heated up, primarily by solar energy, moist air begins to rise. This rising air draws more warm and moist air which strengthens the storm. The rising air cools and condenses and gives out the latent heat of vaporisation which energises the storm more and more. TCs occur primarily in the summers and are shown to be affected by the Sea Surface Temperature (SST), El-Niño, Madden-Julian Oscillation (MJO)'s and other weather conditions favourable to its origin. The storms occur further in the east (and less in the West Pacific Ocean) during El-Niño (Klotzbach [2014]). TCs reaching a maximum wind speed of 33 m/s or greater have a clear and warm region at the centre, which makes its detection easier with passive infrared radiometers, called the "eye" which is

surrounded by the spiral bands of cumulus and cumulonimbus clouds extending out to 1000 Kms from the centre (Hawkins and Imbembo [1976]).

There are two renowned schools of thought that explain the TC intensification mechanism. The first theory, CISK, is an acronym for Convective Instability of the Second Kind. The theory has the convective chimney as their working basis. The second theory, WISHE expands to, Wind-Induced Surface Heat Exchange. Similarities, differences, and limitations of both the theories are presented in the table(1.1)

1.1.3.1 Metrics for Intensity

Several scales have been introduced to rank the tropical cyclones. For instance, Saffir-Simpson Hurricane Scale, Japan Meteorological Agency's scale, along with a few alternate scales like Accumulated Cyclone Energy (ACE), Power Dissipation Index (PDI), Integrated Kinetic Energy Index, and Hurricane Severity Index (Yu et al. [2009]). The scales are generally governed by the intensity of the sustained wind speed. The sustained wind speed as stated by the World Meteorological Organization (WMO) is defined as the wind speed at a height of 10 m for 10 minutes on an average. This definition is used by most of the weather agencies.

1.2 Effects of Tropical Cyclones on climate

1.2.0.1 Tropical Cyclogenesis

The term Tropical Cyclogenesis encapsulates formation and intensification of TC in the atmosphere (Climatology and Meteorology [2006]. TC climatology was formulated by (Gray [1968]) in 1986 and the mechanism was devised in a cyclone-prone region called, the main development region. Intensive research on the similar work in connection with TC and synoptic scale environment was carried out in detail (Camargo et al. [2010]) and (Tory and Frank [2010]).
TCs form over warm tropical ocean basins. Warm air is more capable of holding water vapour. The tendency to capture waver vapour is given by Clausius-Clapeyron equation:

$$\frac{1}{q_s}\frac{dq_s}{dT} \approx \frac{1}{e_s}\frac{de_s}{dT} = \frac{L}{R_v T^2} \tag{1.1}$$

where, q_s is the saturation specific humidity in kg water vapour per kg moist air, e_s represents the saturation water vapour pressure, T the air temperature, L denotes the latent heat of vapourisation, and R_v defines the gas constant for water vapour. Then, the first term approximates to the second term (Ambaum, 2010 and Allan, 2011). Latent heat release acts as an energy source for a TC. The SST should be above 26.5 °C to support tropospheric deep convection (Palmen [1948a]). Also, air temperature over SST up to 10 m altitude should be lesser than the SST for TC intensification to take place (Arora and Dash [2016], Cione [2012]). This is because, certain lapse rate is required to force the atmosphere to be unstable enough for convection. The warm core characteristic of TC is due to convection (Goldenberg [2008]. Cyclone formation requires six major conditions to be satisfied that are necessary but not sufficient. The six requirements are briefly explained in table(1.2): (Gray [1975], Landsea [2006]).

1. Warm ocean temperature, above 26.5 °C, extended 60 meters deep inside the ocean basin
2. Sufficient humidity in the troposphere
3. Unstable atmosphere
4. Sufficient coriolis force to give rise to low pressure in the cyclone's core
5. Low vertical wind shear
6. Low level disturbances

1.2.1 Warm ocean temperature, above 26.5 °C, extended 50 meters deep

This can be understood in terms of the ocean thermal potential (Cal/cm^2). This is defined as the sum of ocean thermal energy above $26°C$ or down to a depth of 60 m.

$$E = \int_{Sfc}^{60m\ or\ where\ T=26°C} \rho_w C_w (T - 26) dz \tag{1.2}$$

1.2.2 Sufficient humidity in the troposphere

It has been observed that TC genesis occurs mainly in the regions of seasonally high tropospheric humidity. High level humidity is more conductive to deep cumulus convection and greater vertical coupling of the troposphere than is in a dry middle level environment. This is also conductive to high cloud precipitation efficiency. Over oceans, high middle level vapour content appears to be a strong enhancer rather than inhibitor of deep convection. TC development is not possible if seasonal 500 to 700 mb humidity is less than 40%.

$$Humidity\,parameter = \frac{\bar{RH} - 40}{30} \tag{1.3}$$

where, the humidity parameter $\bar{RH}$ lies between 40 to 70 %.

Known climatic oscillations like El-Nino Southern oscillations (ENSO) and Madden Julian oscillations (MJO) influence TC activity, its frequency and occurrence timings (Avila and Pasch [1995]). Warm water is required to fuel TC's warm core thus the warm ocean temperatures summed up to 50 meters below the sea surface is an important factor for TC genesis (Briegel and Frank [1997]). Convection is ensured by warm ocean temperature but is sustained by warm ocean waters in the upper levels of the tropical ocean, also known as the thermocline. If SST summed over a column comes to 26 °C isotherm has 30 KJ/cm^2 or higher heat amount, the probability of TC to intensify increases (Goni et al. [2003]). It can also influence the dynamics of a tropical cyclone by creating convective asymmetries. Vertical wind shear is a wind gradient or the difference in velocity, speed and direction of the flowing air close to the surface and the wind above. Vertical wind shear between surface and tropopause under 10 m/s is supportive of TC evolution (Landsea [2006]). Stronger vertical wind shear would dissipate the storm by hindering TC maturation (of Illinois [2006]). According to the technical definition of the wind shear, difference in wind speeds between 200mb, top of the troposphere (40,000 feet) and 850mb, (5000 feet) above the ground level is considered. Wind shear is calculated over a circular area, with the TC placed in the center, of about 700 meters in diameter. The reason for considering 850 MB and 200 MB pressure levels is possibly denser and more reliable cloud track winds at these levels (Nicholls and Pielke [April 1995]). Wind shear is responsible for distorting cyclone profile but its influence (if any) on TC intensity is still not well understood. One mechanism explains the impact of wind shear on cyclone intensity as a drying out behaviour.

According to this mechanism, wind shear leads to drying of troposphere which hinders TC maturation. Apart from drying out behavior, wind shear can also create convective asymmetries (Tang Brian and Emanuel [2010]) which may dissipate energy from the TC that acts as a heat engine. Apart from negative effects of vertical wind shear on TC development, in limitation, it can enhance formation of convective cells and hence assist in TC expansion (Paterson et al. [2005], (Zhang and Tao [2013]).

1.3 Quantifying Tropical Cyclone Intensity Using Emanuel's Approach

Limit calculation for TC intensity: A weak vortex is placed over this neutral state. The added vortex is a warm core and a cyclone diminishing in intensity with height. This preliminary vortex satisfies hydrostatic and gradient wind balances. Consider a fluid flowing from high to a low pressure. Let, it's specific volume be, α. The pressure gradient is then given by,

$$-\alpha\nabla p \tag{1.4}$$

If p is a vertical coordinate, we define it in terms of $\nabla\Phi$ where, Φ is geo-potential which is integral of gravitational acceleration over altitude. Circular vortex is equilibrium state if,

$$\frac{\partial\Phi}{\partial p} = -\alpha \tag{1.5}$$

$$\frac{\partial\phi}{\partial r} = \left(\frac{v^2}{r} + f * v\right) \tag{1.6}$$

Here, f is the coriolis parameter which is expressed in terms of angular velocity of earth's rotation and the latitude, θ

$$f \equiv 2 * \Omega sin(\theta) \tag{1.7}$$

Also, from ideal gas equation, we approximately have,

$$\alpha = \frac{R_d * T}{p} \tag{1.8}$$

Eliminating $\partial\Phi$ from Hydrostatic 1.5 and wind gradient 1.6 equations, we obtain

$$-\alpha\frac{\partial p}{\partial r} = \left(\frac{v^2}{r} + f * v\right) \tag{1.9}$$

Cross-differencing equation, 1.9, and using ideal gas equation, 1.8.

$$\left(\frac{2 * v}{r} + f\right)\frac{\partial v}{\partial p} = \frac{R_d}{p}\frac{\partial T}{\partial r} \tag{1.10}$$

The radiatively inward temperature gradient, $\frac{\partial T}{\partial r}$ is proportional to the upward lowering of azimuthal wind speed, $\frac{\partial v}{\partial p}$
The weighted mean specific entropy for liquid, vapour and ice content in TC is,

$$M * s = M_d * s_d + M_v * s_v + M_l * s_l \tag{1.11}$$

Where, M refers to the sample mass, $M_s, M_l, \& M_v$ denotes the masses of dry air, liquid and water vapour, respectively. Now,

$$s = (1 - q_t) * s_d + q_v * s_v + q_l * s_l \tag{1.12}$$

Where, $q_t = q_v + q_l$, such that q_v refers to specific humidity (M_v/M_{air}), q_l indicates specific liquid water amount, M_l/M_{air} and q_t is the total specific water amount. Clausius-Clapeyron equation relates specific entropies of liquid water and water vapour as :

$$s_v^* - s_l = \frac{L_v}{T} \tag{1.13}$$

Where, specific entropy of water vapour s_v^*, and latent hear of vaporization, L_v in equation 1.13 can be associated to the net entropy in equation, 1.12 to give,

$$s = (1 - q(t))s_d + q_l * \left(s_v^* - \frac{L_v}{T}\right) + q_v s_v \tag{1.14}$$

Using definition of specific entropies of gases and liquid water,

$$s_d = c_{pd} * \ln(T) - R_d * \ln(p_d) \tag{1.15}$$

$$s_v = c_{pv} * \ln(T) - R_v * \ln(e) \tag{1.16}$$

$$s_l = c_l \ln(T) \tag{1.17}$$

Where, R_d and R_v represents the universal gas constant divided by the mean

molecular weight of dry air and the water in respective cases. The heat capacity of dry air at constant pressure is C_{pd} and the heat capacity of water at constant pressure is, C_{pv}. C_l is the heat capacity of liquid water and sum of partial pressures of all the gases, dis-including water vapour is P_d. e denotes the partial pressure of water vapour. Using s_d, s_v, and s_l in equation, 1.14 gives:

$$s = (C_{pd}(1 - q_t) + C_l q_t)\ln(T) - R_d \ln(P_d) + \frac{L_v q_v}{T} - q_v R_v \ln(H) \tag{1.18}$$

where, $H = \frac{e}{e^*}$, and e^* being the saturation vapour pressure. Equivalent potential temperature, θ_B, can be used in place of s. Thus,

$$s = (C_{pd}(1 - q(t)) + C_l q_t) * \ln(\theta_B) = s + R_d \ln(P_0) \tag{1.19}$$

In the case of radiative equilibrium, land surface and the air over it are not in thermal equilibrium which brings energy for the convective heat transport away from the surface. Specific volume, α (inverse of density), conserved entropy in a reversible adiabatic displacement, $\alpha = \alpha(p, s)$. Difference between specific volume of a parcel and its environment at the same pressure level is,

$$\alpha_p - \alpha \simeq \left(\frac{\partial \alpha}{\partial s}\right)_p * (s_p - s) \tag{1.20}$$

Since adiabatic lapse rate is positive, the atmosphere is unstable if its entropy decreases upwards. A stable atmosphere possesses increasing entropy with height. A parcel displaced from a layer of higher entropy to lower one will have greater entropy. An important condition for convective instability is that entropy decreases upwards.

Consider a saturated sample at the same T & P ($\therefore H = 1 \Rightarrow \ln(H) = 0 \Rightarrow q \longrightarrow q^*$). In tropics, lapse rate of a parcel is close to the adiabatic lapse rate. About 30% of the incoming solar energy is reflected by clouds, vegetation, oceans and snow on earth. We can divide turbulent heat transport into (1) sensible and (2) latent heat. Latent heat flux is given by the evaporation rate of water from the surface into the air above. In tropics, most of the heat is due to latent flux than sensible heat or the net long wave radiative flux from the surface. So, we can safely assume that solar radiation absorbed by the tropical ocean is in equilibrium with the evaporation related cooling. Evaporation rate from over the ocean surface is given by,

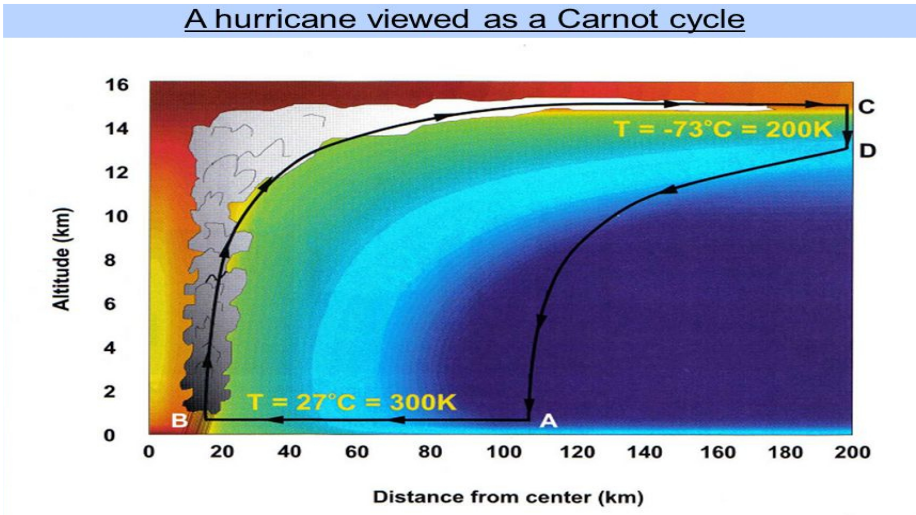

FIGURE 1.2: Mature TC as a Carnot Heat Engine. Source: Divine Winds by K. Emanuel. Colours, in the figure above, represents entropy distribution where cooler colours signify low entropy and warm shades shows higher entropy.(Figure courtesy: Emanuel, 1986)

$$E \simeq C_q \rho |V| (q_0^* - q) \tag{1.21}$$

Where, exchange coefficient, C_q, density of air, ρ, wind speed magnitude, $|V|$, specific humidity of air, q, saturation specific humidity of air, q_0^*, at SST and sea level pressure defines the evaporation rate over the sea surface. C_q is calibrated at $10m$ over the surface and it is convenient to quantify all the quantities in equation (1.3) except q_0^*. The difference between the saturated and unsaturated specific humidity causes disequilibrium in the atmosphere and fuel TC. As seen in the figure(1.2), energy cycle of a mature TC, it can exist in steady state for several days considering axi-symmetric steady storm formation. A turbulent boundary layer where storm air initially runs in is about $1km$ wide and $100m$ on depth. The spiralling air subjected to slight fluctuation in its net entropy is due to ocean heat flux which increases entropy in the boundary layer. Downdrafts in storm's spiral band along with chaotic entrainment at the top of the boundary layer take place. Both of these processes take place in low entropy air from above layers of the troposphere. This entrainment of low entropy air stops near the eyewall convection and high winds from over the surface cause entropy to rise sharply. Wind energy which dissipates as the cube of average wind speed leads to the rise

of entropy in the boundary air, the only source for tropical cyclone activity is the surface heat content. It should be noted that dissipation of kinetic energy increases the entropy of incoming air while keeping its enthalpy the same. Air coming in towards the storm centre spirals out to larger radii. Loss of heat from SST is compensated by export through the outer wall of the storm as shown in the figure(1.2).

$$\dot{s_{inflow}} = \frac{2 * \pi}{T_a} \int_{r_e}^{r_0} [C_k |V_a| (k_0^* - k_a)] \rho_a r dr \tag{1.22}$$

This integral ranging from r_a which covers the area of the control volume is the inner radius towards, r_0 which denotes the outer radius. Surface exchange coefficient, C_k, average wind speed $10m$ above the land and ρ_a, the air density at the altitude along with the specific enthalpy of moist air defines the inflow entropy for the cyclone.

Specific enthalpy can be written as,

$$k \equiv [C_{pd}(1 - q_t) + C_l q_t]T + L_v q \tag{1.23}$$

Where, k_0^* is the enthalpy of air which is saturated at SST and pressure, k_a ascribe to the enthalpy of air at $10m$ altitude above the surface, which is considered as reference altitude. Computing outflow energy involves rigorous treatment (Bister and Emanuel [1998]). Here, we simplify the calculations by safely assuming an artificial energy sink that removes heat energy which is then added in the boundary layer. Considering the outward energy flow at mean temperature, T_0, taking outflow far away from the centre in the region where kinetic energy diminishes so that the outflow heat energy is then equal to the total energy. With these assumptions, the outflow entropy is defined in terms of the outflow temperature as,

$$\dot{s_{outflow}} = \frac{2\pi}{T_0} \int_{r_e}^{r_0} [C_k |V_a| (k_0^* - k_0)] \rho_a r dr \tag{1.24}$$

Dissipation of kinetic energy in the boundary layer can be accounted to the dissipation of the kinetic energy of the wind which is an irreversible process. The boundary layer temperature here is defined by T_a. The irreversible entropy source originating from wind dissipation in the boundary layer can be integrated over the considered control volume of the storm as,

$$\dot{s_{dissipation}} = \frac{2\pi}{T_a} \int_{r_e}^{r_0} [C_D |V_a|^3] \rho_a r dr \tag{1.25}$$

here, C_D refers to the surface drag coefficient state variable, entropy, s, vanishes in a steady state system. Thus, considering it to be a steady state system, total s which is the sum of equations 1.24, 1.22 & 1.25 disappear. Thus, $\dot{s_{inflow}} + \dot{s_{outflow}} + \dot{s_{dissipation}} = 0$

$$\frac{2*\pi}{T_a}\int_{r_e}^{r_0}[C_k|V_a|(k_0^*-k_a)]\rho_a r dr + \frac{2\pi}{T_0}\int_{r_e}^{r_0}[C_k|V_a|(k_0^*-k_0)]\rho_a r dr + \frac{2\pi}{T_a}\int_{r_e}^{r_0}[C_D|V_a|^3]\rho_a r dr = 0 \tag{1.26}$$

Thus,

$$\frac{C_k}{T_a}|V_a|(k_0^*) + \frac{C_k}{T_0}|V_a|(k_0^* - k_a) + \frac{C_D}{T_a}|V_a|^3 = 0 \tag{1.27}$$

$$C_k|V_a|(k_0^* - k_a)\left(\frac{T_0 - T_a}{T_0}\right) = -C_D|V_a|^3 \tag{1.28}$$

We also assume that all the three integrations occurs at the radius of maximum winds where the dissipation rate are close to their maximum values. Thus, at the radius of maximum winds, the storm speed is,

$$|V_{max}|^2 = \frac{C_k}{C_D}\left(\frac{T_a - T_0}{T_0}\right)(k_0^* - k_a)|_m \tag{1.29}$$

From equation(1.29), we can make out a few vital points worth consideration in terms of thermodynamics and dynamics of the storms.

Fundamentally energy cycle of a TC is analogous to Carnot heat engine. This inflow entropy from the source, the SST, can be quantified as low entropy and warm shades show higher entropy.

1. Maximum wind speeds or specific kinetic energy of the winds is directly proportional to the disequilibrium. This thermal disequilibrium, (k_0^*), appears due to the thermal gradient and also inversely depends on the lower tropospheric wind speed.

2. Thermodynamic efficiency, given by, $\frac{T_a - T_0}{T_a}$ is multiplied with (k_0^*) and this makes cyclone's efficiency greater than a Carnot engine. This additional multiplicative term can be accounted to the use of a part of the dissipated in the cycle. This recycling of the dissipated energy increases storm's efficiency over Carnot engine.

3. Specific kinetic energy of the storm or its wind speeds depend on the ratio of the exchange coefficients of enthalpy and momentum and not on the variables themselves.

Using equation(1.29), we can estimate the value of cyclonic winds, provided values of other parameters are known. T_a which refers to the temperature close to the sea surface could get cooler owing to evaporation sea spray and adiabatic cooling. If we use equation(1.29) to determine maximum value of tropical cyclone intensity then we can take T_a as SST. Passage of TC over the sea surface decreases the SST by about 5 K. If we know the vertical profile of the atmosphere of the TC, its convenient to determine the outflow temperature, T_0. $\because$ TC move inertial gravity waves, caused owing to effect of buoyancy on a fluid parcel which then oscillate to the interface between the two fluids and hence act as sub-critical vortices. Sub-criticality of TC ensures that isentropic surfaces blend in well with the storm's unperturbed rings *i.e.* the air grows up to the region with temperature equal to the unperturbed environmental air of the TC lower stratosphere that has isothermal atmosphere. If these air parcels reaches up to the lower stratosphere layer, then we can assume the outflow temperature to be a constant value equal to that of the stratospheric layer. Finding C_k and C_D is difficult especially in wind speeds greater than 20 m/s due to froth and spray over the ocean surface.
For this situation of ocean, we do not have a suitable enthalpy and momentum theory. Thus, it poses a challenge to forecast the behaviour. Here, we consider the coefficients to be equal in strong winds. Difference of $(k_0^* - k_a)$, can be found out with the knowledge of surface pressure and humidity at the surface of maximum winds. Employing the definition of specific enthalpy 1.23, we can have,

$$(k_0^* - k_a) \simeq L_v(q_0^* - q_a) \tag{1.30}$$

Here, air temperature is taken as equal to the SST. Specific humidity is the ratio of water vapour mass to that of the air. Thus,

$$q = \frac{m_v}{m_d + m_v} = \frac{\rho_v}{\rho_d + \rho_v} = \varepsilon \frac{e}{p - (1 - \varepsilon)e} \tag{1.31}$$

Where, total air pressure is defined as, p; density of water vapour as, ρ, the density of dry air as, ρ_dS, the partial pressure of water vapour as , e, and molecular weight of water per unit molecular weight of dry air as, ε. In atmosphere, $e << p$. Thus,

$$(k_0^* - k_a) \simeq L_v * \left[\frac{(e_0^* - e_a) * \varepsilon}{p}\right] \tag{1.32}$$

Introducing, relative humidity, H as, e/e^*,

$$(k_0^* - k_a) \simeq \frac{\varepsilon L_v e^*(1 - H_a)}{p} \tag{1.33}$$

Substituting value of $(k_0^* - k_a)$ from 1.33 in 1.29, we get,

$$|V_{max}|^2 = \frac{C_k}{C_D}\Big(\frac{T_a - T_0}{T_0}\Big)\frac{\varepsilon L_v e^*(1 - H_a)}{p}|_m \tag{1.34}$$

Thus, by knowing the value of parameters on the right-hand side, we can compute a very useful expression for the maximum cyclonic winds and hence the cyclone intensity.

Both the methods give similar results. Here, the theory of the later approach is explained. As can be observed in the figure (1.3), spiralling in towards the storm centre acquires heat from the underlying ocean basin. This heat shows up as an increase in humidity instead of rising in air temperature. Evaporating water takes in ocean's heat which resides in the water vapour content of air and does not show as rising in air temperature and is hence known as latent heat. Once the air reaches the eyewall of the storm, it turns upwards and owing to inertia keep rising upwards to about 15 to 18 km of height, and then flow outwards from the cyclonic structure. The total increase in heat content on this leg1, figure(1.4), can be seen as a total rise in water vapour amount in the atmosphere and the decrease in pressure; this effect is called "heat input by isothermal expansion". Not all of the heat input into an engine turn to work. So, in our system, a TC, not all the added heat work out to cause wind gusts.The system (TC) is considered analogous to the thermodynamic engine and the fraction of useful heat is the efficiency of this system.

$$\varepsilon = \frac{T_s - T_0}{T_s} = \frac{\Delta T}{T_s} \tag{1.35}$$

Where, T_s denotes temperature of the source that here is ocean temperature, SST, in Kelvin. T_0 represents the temperature at which heat is exported from the system in Kelvin. The taller a cyclone is lower is the temperature at the top of the storm, higher is the temperature gradient, ΔT and hence, more is the thermodynamic efficiency. In order to compute, T_0, we need to know how much heat the eye-wall possess and the vertical profile of the air in the environment of the storm. We can then find out how high air can rise in the eye-wall and using this information, we

can find the magnitude of T_0. Using SST as the source temperature, T_s, a typical hurricane possess efficiency of approximately $\frac{1}{3}$. For each square meter of ocean surface area, the ate of energy fed into a storm system is given by, a parameter defined as generation rate, G.

$$G = \varepsilon C_k \rho v_s (k_0^* - k_a) \tag{1.36}$$

In equation, 1.36, parameter C_k denotes enthalpy transfer coefficient, v_s is the surface wind speed, k_0 defines enthalpy of the ocean surface, k_a again is the enthalpy but of the atmosphere in the vicinity of the storm. Close to the radius of maximum winds, v_s, is large. Once the storm has reached steady state, so that no intensification or change in it occur, most of the energy is consumed by friction between the winds and sea surface. Dissipation of this energy per unit square metre of sea surface is given by,

$$D = C_D \rho v_s^3 \tag{1.37}$$

Dissipation rate as exhibited in equation 1.37, show that the rate depends on upon the cube of maximum wind speed, drag coefficient, C_D, and ocean density, ρ.

Now, since frictional dissipation, D, depends heavily on v_s, which is maximum near the radius of maximum winds just like energy generation rate, G; we can equate D to G at the radius of maximum winds.

$$C_D \rho v_s^3 = \varepsilon C_k \rho v_s (k_0^* - k_a) \tag{1.38}$$

$$v_s^2 = \frac{C_k}{C_D} \varepsilon (k_0^* - k_a)|_m \tag{1.39}$$

Equation 1.39 gives cyclonic wind gusts in terms of enthalpy exchange ratio, efficiency and atmospheric-ocean enthalpy. Ratio $\frac{C_k}{C_D}$ express exchange of enthalpy and momentum between air and water. Thus, we need to know the fraction of oceanic heat exchange per unit momentum exchange, $\frac{C_k}{C_D}$. Also, the speed does not depend on the internal structure of the storm. Since, we do not have observational values of the ratio, $\frac{C_k}{C_D}$, it was assumed to be unity in the code used. Though, this assumption about the stated ratio is contradicted by several studies e.g. (Smith et al. [2014]) show that, ratio C_k/C_D less than 0.75 can cause cyclone formation it was not allowed following the theory. The physical explanation of such result

was given to be the regime shift of the structure of turbulence in the boundary layer where C_k values are high. The mechanism was explained using spectral analysis which showed that as the boundary layer approaches neutral stratification, smaller-scale eddies dominantly contributes to the turbulent transport of humidity and sensible heat Thus, C_k, values increase in the process.

This traditional thermodynamic approach to determine cyclone intensity provides a good beginning to our understanding of cyclones' strength. However, further detailed cyclone physics is required to determine PDI values closer to the observed ones. Present cyclone intensity model predicts cyclone intensity values which can be understood in terms of V_{max} and P_{min}. Cyclonic wind speed as given by Equation(1.39), shows the direct dependence of cyclone's intensification on its thermodynamic efficiency, which in turn depends on the ocean-atmospheric temperature gradient rather than ocean temperature merely. Further findings in this study unambiguously reveal that it's not the high sea surface temperature that influences cyclone strength but the difference between ocean and atmospheric temperature.

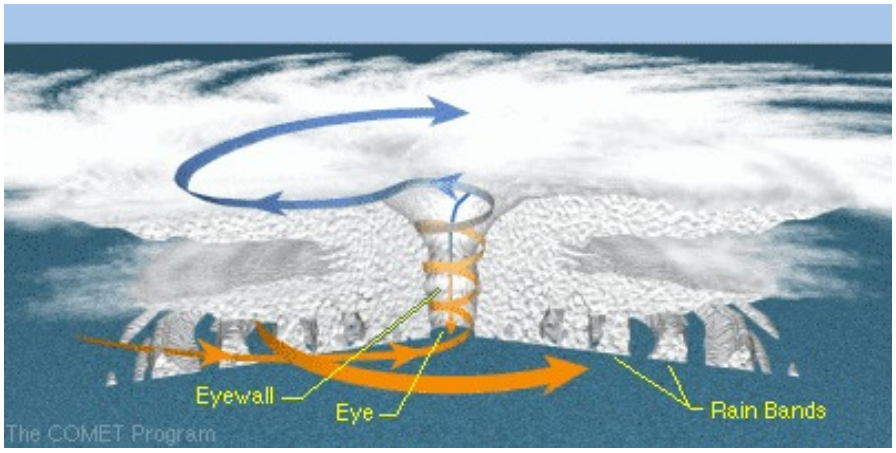

FIGURE 1.3: Hurricane Structure. Source: COMET Program (COMET [2011])

1.3.1 Thesis Aims and Outline

The main objective of this thesis is to understand changes in TC activity under climate change scenario. A thorough investigation into the nature of TC activity, focusing on Tropical Cyclone Intensity (TCI) under present and the climate change (2XCO_2) situation is conducted. An important part of the research is to quantify cyclones' sensitivity to global warming.

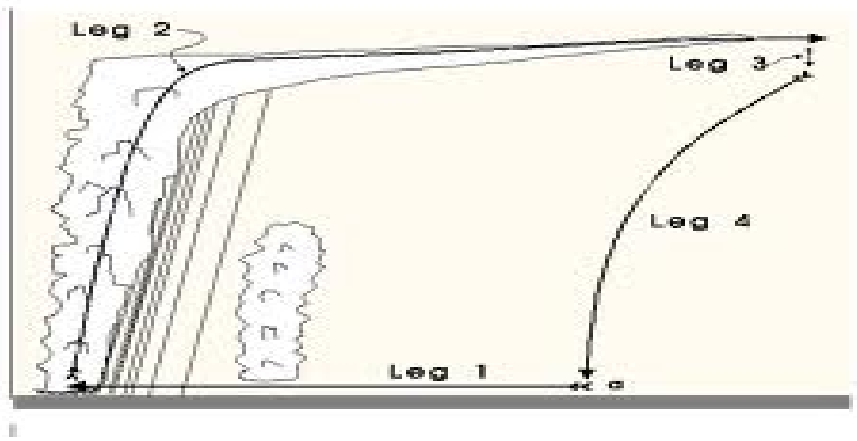

FIGURE 1.4: Hurricane Structure. Source: The COMET program (COMET [2011])

As the developed techniques like power dissipation index (PDI), to quantify TC intensity lack closeness to the observed values, an in-depth study is done to quantify the gap between theoretical values and the observed ones. The average value of the gap found in different ocean basins is then deducted from the model output under doubled CO_2 layout. So that we can compute and compare TCI under increased CO_2 situation which is closer to the observed value/s.
TCI deduced from theoretical cyclone PDI model (Bister and Emanuel [1998] with input from Met office Hadley center's global climate model (GCM) is evaluated for further analysis. Most of the climate change impact assessments account for climate change uncertainty by using scenario based approach.

Research questions investigated in this thesis are as follows:

1. How does tropical cyclone intensity respond to climate change? Is the response same in all the ocean basins?

2. How is tropical cyclone strength distributed over different ocean basins across the globe? Is this distribution homogeneous or it varies spatially with different ocean basins possessing storms of different strength.

3. Can we develop a simple statistical model to determine the distribution of tropical cyclone intensity?

4. How has tropical cyclone intensity changed over time?

5. What all natural processes are there that influence tropical cyclone intensity in different ocean basins? Which natural phenomenon is there that impacts tropical cyclone intensity in all the ocean basins?

6. How good is sea surface temperature in determining tropical cyclone intensity?

7. Amongst the various parameters responsible for tropical cyclone intensification, SST, SLP, atmospheric temperature, wind shear and moisture content, which input parameter has the strongest impact on cyclone intensification?

	CISK	WISHE
Expansion	Convective Instability of Second Kind	Wind Induced Surface Heat Exchange
Assumpations	Demands initial instability (like frontal low, tropical wave)	Initial instability is not needed. Evaporation from ocean, enhanced by winds cause instability
Working mechanism	Once a surface area of low pressure is established, air rises and in turn, makes atmosphere surrounding the disturbance more unstable. As instability increases, air rises faster causing thunderstorms and deep clouds.	Once a low-pressure region is in place, convergence at the surface is enhanced, resulting in faster wind and more evaporation.
Feedback mechanism	The end result is a positive feedback whereby clouds and thunderstorms continue to develop as long as ocean temperature is sufficiently warm.	Like in CISK, a positive feedback is established whereby TC continue to strengthen as long as the ocean temperature is warm enough.
Difference	Pre-existing convection is the driving mechanism	Surface wind is the driving mechanism
Similarities	1) End result is a positive mechanism.	2) Heat release from ocean aids TC air circulation.
Working mechanism (Pictorial representation)	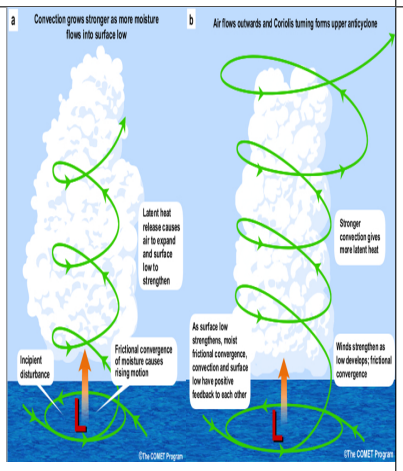	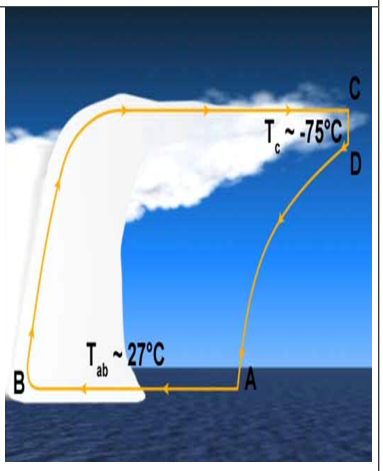

TABLE 1.1: Assumptions, working mechanism, similarities, and differences of CISK and WISHE theories.(Image source - Comet programme: http://comet.ucar.edu/)

Parameter	Favorable condition	Genesis Role
Warm ocean temperature or Ocean energy parameter, E	Large ($\geq 26.5°$C)	Maintains surface energy to assist large sea to air energy transfer assist large sea to air energy transfer
Tropospheric humidity: Humidity parameter $\bar{RH}$ between 500 to 700 mb	Large ($> 40\%$)	Allows for deep cumulus convection and high rainfall efficiency
Unstable atmosphere: Moist stability parameter, $\frac{d\theta_e}{dp}$ from surface to 500 mb	Large gradient $> 15°$C	Permits cumulus convection
Sufficient Coriolis force or f	Large (latitude $> 5°$)	Helps sustain pressure gradient & sustaining of BL BL winds against frictional dissipation
Low vertical wind shear Parameter, $\frac{1}{S_z+3}$ where $\frac{1}{S_Z}$ is in units of $(m/sec)^(-1)$ 750 mb	Vertical wind shear $< 10m/s$	Induce condensation warming to be concentrated over moving disturbance, inhibiting ventilation energy
Low level disturbance: defined by vorticity parameter at 950 mb in $10^{-6}(sec)^{-1}$	Large $> 40\%$ of normal	Allows low level mass moisture, & momentum convergence

Table 1.2: Summary of the primary TC genesis parameters

Chapter 2

Methodology and Data Used

Global Climate Models, GCMs, are sophisticated tool to understand our changing climate which when combined with advanced statistical methods to nurture our understanding of the intriguing natural phenomena.

2.1 Model Output

The research question investigated in the thesis use wide range of methods; statistical, spectral and numerical, and a collection of data sets which are introduced here in this chapter. This section presents a brief summary of the tools used; Global Climate Model (GCM) and Perturbed Physics Ensemble (PPE), statistical analysis methods like Partial Least Square Regression (PLSR), wavelet transform and least square regression method. An in depth explanation of specific methods applied under various scenarios is given in each chapter as needed.

Section 2.1.1 of this chapter describes the reanalysis data, as well as observed variables employed in this work. Ways to analyse our hypothesis or carry out a research is stated in the methodology section.

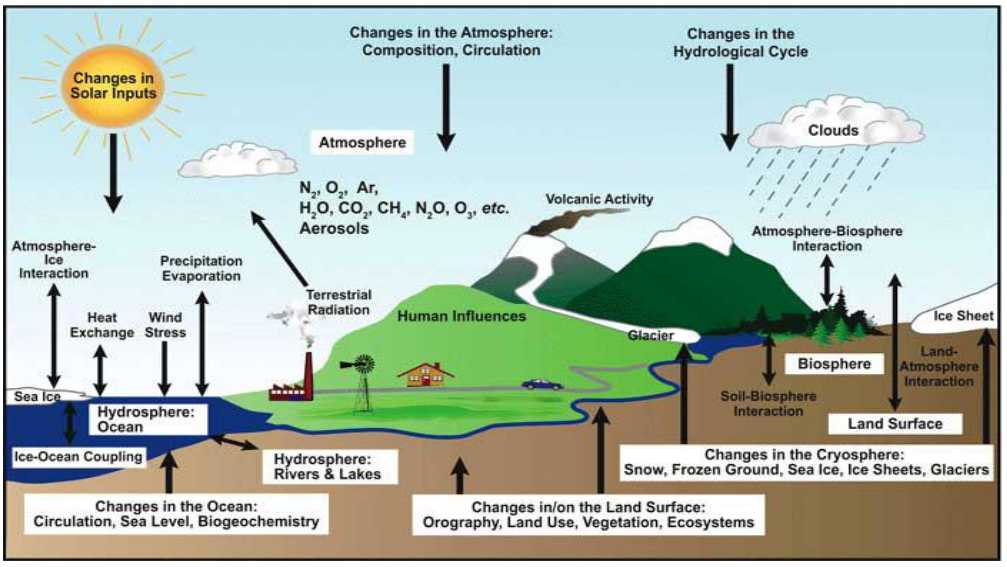

FIGURE 2.1: Processes and interactions involved in the global climate system (Courtesey Treut et al. [2007])

2.1.1 Global Climate Model (GCM) an Introduction and Model Physics

Global Climate models (GCMs) are numerical models representing physical processes in our atmosphere-ocean-cryosphere and land surfaces. These models can be put to use to simulate the response of increased green house gas concentration. These are widely applied for weather forecasting, understanding the climate, and projecting climate change. All the GCMs fragment the fluid dynamics equations to simpler forms that are easy to solve.

These climate models can be categorized into three types. Simple radiation heat transfer model, radiative convective models with more complexity included and finally the coupled atmosphere ocean sea ice global climate models which lie at top of the hierarchy of GCMs in terms of complexity Coupled models discretize and solve the full equations for mass and energy transfer along with the equations quantifying radiant exchanges.

In order to enhance our understanding of the earth system including atmosphere, land, ocean and cryosphere (snow, ice, permafrost) quantitatively, computer models are employed. These climate models try to mathematically replicate the components of earth system and their interactions. Various physical, chemical, and biological processes happening in our atmosphere, (Figure 2.1), are computed on

a grid. Despite the availability of supercomputers, it is still a computational challenge to simulate the grid scale good enough to resolve clouds, along with their subsequent rainfall, small ocean eddies, and other small scale processes involved in boundary layer & ocean-atmospheric exchange phenomena.

Parametrization provides a method to show these small scale phenomena on model grid. The computer models, weather forecasting models, used to simulate atmosphere are known as Atmospheric General Circulation Models (AGCM) just like the models that simulate ocean circulations and are termed as Ocean General Circulation Models (OGCM). Both types of models are used separately when ocean surface and sea ice amount is fed into AGCM and surface temperature, ocean salinity along with wind speeds are used as input to the OGCM Harvey et al. [1997]. However, owing to large heat capacity of ocean basins, which can strongly influence atmosphere via oceanic heat transfer, both models are coupled and are called AOGCM.

2.1.2 GCMs and Tropical Cyclones

Spatial scale involved in Tropical Cyclones (TC) formation and their activity is much finer than our present day GCMs. Convection and interaction between large and small scale vortices in storms pose a challenge to even finer GCM resolution, 12 to 30 Km Harvey et al. [1997]. GCMs consider many different physical phenomena and few of which are much smaller than the spatial scales of GCMs. To solve this problem, parametrization comes in handy.

2.1.3 Perturbed Physics Ensembles (PPE) and Multi Model Ensembles (MME) Explained

Perturbed physics ensemble is a collection of model runs from different model variants produced by varying the values of parameters in a given climate model configuration.

PPE is generated by changing the values of parameters involved in a climate model, thus creating a different version of that model. Parameterization values involved in GCMs, that account for the relationship between the large scale and

small scale processes may not be precisely known and can have a range of acceptable values. This type of uncertaininty source is called parameter error. By changing these variables with a range of plausible values creates different versions and may lead to different climate projections for each variation. Ideally, full range of variability of each model variable would be explored to generate a certain type of climate projections. Spread of results thus obtained are then examined Collins et al. [2011] Multi Model Ensemble (MME) is an alternative approach to weigh uncertaininty in the model output apart form using PPE. The technique employ different climate models that include different structures. In order to understand probability distribution of future climate change, results from PPE and MME are combined. PPE can be beneficial over MME; for instance, in case of the ocean, when inadequate amount of information makes it challenging to predict probability of future variations in marine sector, unlike in case of atmospheric and land surfaces. Beneficial insights about the future maritime climate can be obtained from the PPE and to a lesser extent MME.

2.2 Observational Data

2.2.1 IBTrACS Data

International Best Track Archive for Climate Stewardship abbreviated as, IBTrACS, supply global TC best track data in terms of cyclone distribution, frequency, and intensity. [1]

2.2.1.1 Advantages and Limitations of IBTrACS Dataset

Most importantly, this data archive combines global TC data at a central location. The required data can be extracted in one single file or multiple files as needed. IBTrACS repository is considered to be the most exhaustive global set of historical TCs data available and it includes data from 12 different agencies and historical databases. However, there are a few weaknesses of the archive. Firstly, multiple sources providing TC data could be conflicting. Secondly, North Indian Ocean data is limited and goes back to 1990 only. Finally, operational procedures and

[1] The data set is available in netCDF, ASCII and Shapefile formats.

observational systems update and vary over time which may lead to a significant discrepancy [Knapp R et al., 2010].

2.3 HadISST Dataset

The version 1.1 of Hadley Centre's global sea ice and sea surface temperature data used here constitutes global SST and sea ice field. The dataset has monthly time resolution starting from 1871 until present.

2.3.0.1 Data Assimilation Technique, HadISST

HadISST applies reduced space optimal interpolation to SSTs from the marine databank, primarily ship tracks and ICOADS (International Comprehensive Ocean-Atmosphere Data Set) through 1981 and a combination of in-situ and calibrated data acquired from satellites since 1982. SST data between 1871 and 1971 is fine tuned by utilizing "Bucket Correction". Grid boxes of the archived datasets which were fractionally covered with sea ice, were employed to use the statistical relationship between the sea ice and SST to fill in the missing gaps. If a gird box is covered by sea ice by over 90%, a constant value of -1.8 $°C$ is considered for the region. The dataset is mainly appointed to be used as boundary conditions for atmospheric models[2]. Spatial resolution of the dataset is 1° X 1° and constitutes ocean only data. Input data is obtained from Met office marine data bank, ICOADS, GTS, and AVHRR SSTs. The archive is maintained by the Computational and Informational Systems laboratory, CISL, at the National Centre for Atmospheric Research, NCAR, is sponsored by national science foundation, NSF. and the original data are available from the RDA in dataset number, ds277.3.(Solomon and Newman [2012],Deser et al. [2010],Rayner et al. [2003])

2.3.0.2 Strengths and Weaknesses of HadISST Dataset

The spatially exhaustive global dataset, however, possess few limitations valuable to be employed as a boundary condition for forecasting AMIP runs. Limitations of HadISST includes an absence of varying SST measurement methods after 1941,

[2]The data is available in netCDF and ASCII formats

which are not accounted for. Polar regions, especially Southern Ocean SST data is exiguous. SST in high northern latitudes also depends upon the sea ice analysis which has its own limitations. Thirdly, non-robust SST appearances have been noted; for instance, SST trends over the 20th century in the equatorial Pacific Ocean are miss interpreted owing to the interpolation methods applied Solomon et al. [2011] and/or due to ENSO variance Solomon and Newman [2012]. Schmidt et al. [2012]

2.3.0.3 Climate Model Intercomparison Project version-5 (CMIP5) Dataset

The TCPI was computed for the historical runs (which includes all natural and historical forcings). These are simulations of recent past between 1850 to 2005. Forcings included in the simulations were consistent with the observations. These forcings are atmospheric composition, due to human and volcanic activity, solar forcings, natural and anthropogenic aerosols and the land use change. The retrieved data set, GFDL-CM3, falls under the auspices of the Climate Model Intercomparison Project version-5 (CMIP5). This model is designed to serve as the physical component of ESM (discussed next) (Leo J. et al. [2011])

Advantages

1. 1. CM3 dataset shows notable improvements over its predecessors (CM2.1 and earlier) by including a modified SST bias pattern and reduced biases in the Arctic sea ice cover.
2. 2. Improved simulations in tropical land precipitation relative to previous GFDL models. ((Leo J. et al. [2011])

Disadvantages

1. Ocean interior simulations in CM3 is generally warmer than its predecessors which adversely impacts the interior bias (Griffies et al. [2011])

2.3.1 Atmospheric Reanalysis Dataset

Reanalysis involves a methodological approach to produce data sets for climate recording and research purposes. The methodology involved here is that the data sets are created by inputting observational data, "fixed" (6 to 12 hours collection for atmospheric datasets) into models which assimilate all the inputted observed data over the period of analysis. Since this approach is unvarying, it gives dynamically uniform approximation of the climate state at each time step. The only varying component of this framework, observations as input, is un-escapable since these raw values are obtained from radiosonde, satellite, buoy, aircraft, and ship reports but are not limited to these. About 7 to 9 million observations are absorbed at each time step in the reanalysis. These products have been used vastly and found helpful in research and climate monitoring. However, misleading trends and unreal variability can be produced owing to fluctuating observational blending. The dataset should not be considered same as real or treated as observational data Schreck [2013].

Advantages and Disadvantages of Reanalysis Datasets Reanalysis dataset involves the availability of global statistics. Importantly, it contains time and space resolution over three or more decades. There are over 100's of variables that are accessible for analysis and a better understanding of our climate. Reanalysis aims to continuously improve resolution and biases. The approach includes millions of observations into a consistent data assimilation methodology to enable rigorous analysis of a number of climate processes. Such assimilation would be almost unpractical for an individual to perform. Prominently, the data set is generally straightforward to extract from repositories. On the other hand, figures in reanalysis owing to varying blend of observations and biases in observations and models can lead to artificial changes and trends in the output values. Since reanalysis results heavily depend on the observation, constraint in the assimilated observational digits, spatially and temporally can then influence the confidence in reanalysis output.

2.4 Tropical Cyclone Scales

TC scales are defined based on the basis of its wind speed, size and intensity. The well known cyclone indices introduced so far are as follows:

1. Saffir-Simpson's Scales Williams [2007]
2. Accumulated Cyclone Energy (ACE) Saunders and Lea [2007]
3. Power Dissipation Index (PDI) Emanuel [2005c]
4. Track Integrated Kinetic Energy (TIKE) Misra [2013]
5. Integrated Kinetic Energy (IKE) Mark D and Timothy A [2007]

One of the well known TC classification done according to its wind speed is known as Saffir-Simnpson's scale. The index measure storm's maximum sustained wind speed, for at least 10 mins, above 10m of height from the sea surface. The major limitation of this measure of the storm are,

1. No consideration of storm's wind field
2. Absence of cyclone's capacity to cause coastal flooding

These limitations were taken into account to develop a new TC classification of scales. Based on the experience of the cyclone, Sandy reaching category 3 hurricane and which weakened to category 1 storm just before making landfall. This category classification based on Saffir-Simpson's scale lead many to underestimate its catastrophic capability. But when the storm made a landfall, it made record breading storm surge over Jersey bank and then into New York harbor, thereby inundating low lying areas. Lack of information about Sandy's size and energy caused a lot of destruction and the storm proved to be far more fierce than 2005's TC "Katrina". A new index was then introduced by scientists at Florida State University. This new scale takes into account cyclone's intensity, duration and size. This new ranking method is called, Track Integrated Kinetic Energy (TIKE) and is an extension to already known metric, storm's Integrated Kinetic Energy (IKE), which was defined in 2007. TIKE would help to add up to ACE and PDI, both of which represents exhaust energy of a storm.**TIKE** can be beneficial for warming duration storm surge risk at the time when sea levels are high and coastal population is rising It could help scientists to inspect storm size which might be connected to warming sea and air temperature. **IKE** index considers the life time of a cyclone over all the well known storms of the season and hence provide a measure to compare each storm in terms of its size, energy, wave, wind strength, relative to other storms of the season. TCs has the capacity to churn ocean water

during its movement over the ocean surface via waves and storm surge. Thus, it is vital to understand how storm winds affect structures in its course of motion and the index, IKE, includes that feature as well. It has been noticed that damage from coastal flooding far exceeds the damage due to strong winds. Hence, indices focusing on cyclone's intensity (PDI) part may not well alarm people for a catastrophic events Misra et al. [2013] **PDI** Power dissipation index is defined as the sum of cubes of maximum one minute sustained cyclonic wind speeds at six hourly intervals at all the time when a storm is at least tropical storm strength. The thermodynamic imbalance between the atmosphere and underlying tropical seas provide energy to cyclones for their intensification. More is the thermodynamic disequilibrium between tropical oceans and overlying atmosphere, more energy is fed into a cyclonic system. The stated imbalance act as a source and any factor example a colder land surface, colder SST, surface drag, frictional dissipation, would act as a sink for the cyclonic heat engine. Thus, TCs speed limit can be defined thermodynamically. Once we know the rate and the efficiency with which this reservoir can convert heat to wind energy, TCs speed bounds can be determined. This depend upon the contrast between the atmosphere and ocean temperatures. Interaction of tropical cyclones with their atmospheric and oceanic environment limits the intensity of most storms just below the theoretical value. Still, the limit could be useful for estimating the most intense storm/s falling over an area over a reasonably long period of time.

1. **Reanalysis Data**

   Reanalysis data is a comprehensive record of how weather and climate are changing over time. State of a system in reanalysis is estimated by combining observations and numerical model. This reanalysis project used state of art analysis system to perform data assimilation using data since 1948. The data has a global coverage (88.54N - 88.54S, 0E - 358.13 E).

   Monthly mean NCEP/NCAR reanalysis dataset is used as input to determine tropical cyclone strength using an algorithm based on a thermodynamic model for cyclone intensity. The algorithm (Bister and Emanuel [1998]) takes SST, SLP, atmospheric temperature, and mixing ratio as input variables and yield maximum achievable cyclone winds (V_{max}) & theoretically minimum TC pressure (P_{min}) attainable. Unlike SST (COBE-NOAA [2015],NOAA [2014],Smith et al. [2007]) and SLP (Kalnay [1996]) which are considered at surface level, atmospheric temperature and mixing ratio (Reanalysis [2014])

are considered in the vertical atmosphere. Atmospheric sounding is available for 17 pressure levels including the surface level up to lower stratosphere. 17 pressure levels considered are, 1000, 925, 850, 700, 600, 500, 400, 300, 200, 150, 100, 70, 50, 30, 20, & 10 mb. Data for the mixing ratio, on the other hand, range up to a lesser extent, up to 300 mb, which lies in the lower tropopause. SLP, atmospheric sounding, and mixing ratio datasets, used in developing statistical model, are considered from 1948 onwards. SST is expressed in °C, SLP in mb, atmospheric temperature in °C and the mixing ratio in g/kg. The value of mixing ratio ranges between 0 g/Kg in cold continents to 20 g/Kg in warm tropical areas (Levine [1995]). It's worth noting here that mixing ratio is also referred to as specific humidity in the reanalysis product used here. Three climatological SSTs (COBE-NOAA [2015],NOAA [2014],Smith et al. [2007]) used here were available at 2.5 degree x 2.5 degree global grids (144x73), ranging from 0.5 °E to 359.5 °E, 89.5°N to 89.5°S.

The first set of SST data, $ERSST.V3b$, is the NOAA's extended reconstruction made using most recently available comprehensive ocean-atmospheric dataset (COADS) and improved statistical methods that allow stable reconstructions using sparse data. $ERSST.V3b$ is an improved extended reconstruction over the second version. The second set of SST dataset used, $SST - COBE$, is a monthly mean of global dataset created in June, 2011 at ESRL/PSD using the grid data from JRA. Third SST dataset employed is NOAA's second version optimum interpolation SST, $SST - OI.V2$. $SST - OI.V2$ is an in-situ and satellite SST combined analysis for climate (R.W. et al. [2001]).

2. **Model Data**

   In order to explore influence of projected change of SST on cyclone intensity with enhanced levels of green house gases, we make use of climate model ensembles as derived from the third version of Hadley Centre climate model, HadCM3. Considered climate model ensembles taken from perturbed physics ensemble, are retrieved from HadCM3 Collins et al. [2011].

   HadCM3 simulations used here are done on the 1.25X1.25-degree grid. This enables better heat transport simulation. HadCM3, version 3 of the simulations is used here and is better than the previous one. The 3 primary improvements are as follows:

(a) The new version does not require flux adjustments to prevent large climate drifts.

(b) The improved atmosphere and ocean components.

(c) The newer version does not have spin up procedure.

2.5 Methods Applied

The standard statistical methods used in our investigation were as follows:

1. Pearson's Correlation coefficient and Bootstrap Methods
2. Regression Analysis
3. Partial Least Square Regression
4. Ensemble Empirical Mode Decomposition (EEMD)
5. Wavelet Transform
6. Bilinear Interpolation

2.5.1 Pearson's Correlation coefficient and Bootstrap Methods

`Correlation Coefficient` Correlation is an indicator of whether or how strongly pairs of variables relate to each other. +1 denotes a perfect association. 0 indicates no correlation and -1 shows that the variables are anti-correlated.

The correlation coefficients are essentially useful in the early stages of bivariate analysis (Trauth [2010]). A correlation coefficient is sensitive to outliers and thus should be used cautiously. The Pearson's moment Correlation Coefficient is one of the most popular correlation coefficient method used to estimate a population's correlation from a sample of data. For N number of pairs of X, Y data sets, having a univariate standard deviation of Sx and Sy respectively, the Pearson's moment Correlation Coefficient is given as,

$$R_{XY} = \frac{\sum_{i=1}^{N}(X_i - \overline{X})((Y_i - \overline{Y}))}{(N-1)S_X S_Y} \tag{2.1}$$

where the numerator represents the correlated sum of products of the which on dividing with (N-1) yields the sample covariance. The covariance is widely used measure in bivariate statistics. The Pearson's moment Correlation Coefficient can be tested for statistical significance by determining the probability of an R-value of a random sample from the population with a zero correlation coefficient. Using t-statistic, the significance can be computed as follows:

$$t = R\sqrt{\frac{N-2}{1-R^2}} \tag{2.2}$$

If thus computed t-value comes out to be higher than the critical t, with N-2 degrees of freedom and at α=0.05, the correlation coefficient could then be considered significant at the level α.

Apart from this, we have also used the bootstrap method to determine the significance of the correlation coefficient computed. The bootstrap method repeatedly resamples the sample data set of N data points by choosing an arbitrary set of sub-samples with replacement.

`Bootstrap Analysis` Bootstrap method uses here re-samples the data one thousand times, then computes the correlation coefficient and the regression coefficients for each new subsample. The re-sampling scheme selects an arbitrary set of sub-samples with replacement. Statistics of the obtained sub-samples administer improved knowledge about the characteristics of the population.

2.5.2 Regression Analysis

`Linear Regression` Classical linear regression method used here describes linear relationship and trend between V_m, SST, SAT[3], with time. A trend in cyclone intensity (m/s) is plotted here. Here, time (independent variable) is on the abscissa and tropical cyclone intensity (dependent variable) is on the ordinate axis. The regression technique aims to minimize the deviation in the dependent variable *i.e.* $\Delta V_m = minimum$. Trend of V_m is then predicted by the best fit line given by,

$$Y = b_0 + b_1 X \tag{2.3}$$

[3]**SAT** Here, we define difference between ocean and mean atmospheric temperature, (SST - mean(AT)), as SAT

Where, b_0 and b_1 are the regression coefficients. b_0 denotes the intercept with y-axis and b_1 represents the slope. Applying the least square criterion, sum of the deviation is minimized using,

$$\sum_{i=1}^{i=n}(\Delta y_i)^2 = \sum_{i=1}^{i=n}(y_i - (b_0 + b_1 x_i))^2 \tag{2.4}$$

In order to gain a better projection of the regression coefficients, we use the bootstrap method with 1000 samples. We notice that the statistic, standard deviation, of the regression line is small in the cases shown here. Regions with higher standard deviation, like Southeast Pacific Ocean, are not shown here since they signify not so good estimate of the fit. Small standard deviation (≤ 1) imply that we have a good estimate of the fit. Analysis of tropical cyclone intensity and its connection with various parameters studied here using Pearson's correlation coefficient is tested using the bootstrap method with one thousand re-samples taken. Only the reliable values are stated in the text.

2.5.3 Partial Least Square Regression

Partial least square regression is a combination of multiple linear regression and principle component analysis. The method aims to predict or analyze dependent predictors or variables. This is achieved by a set of input variables which are used to obtain a set of orthogonal factors called, latent variables which have the best predictive power. The method is particularly useful when we have a large set of independent variables.

Partial least square regression was interpreted in statistical framework in 1997 by Phatak and De-Jong as,

$$Y = IK \tag{2.5}$$

where I denotes the observations described by K dependent variables.

$$X = IJ \tag{2.6}$$

where, X represents the number predictors collected on these I observations.

2.5.3.1 Goals of partial least square regression

The aim of this method is to predict Y from X and to express the common features between the two. When Y is a vector and X is full rank *i.e* the number of predictors equals the number of observations made, multiple linear regression. However, there are cases when we do not have enough observations to match the number of variables in X. In such cases, X is likely to be a singular matrix and regression approach fails because of multi-collinearity. Various methods are used to encounter this type of problem. One method reduces the number of variables example by using stepwise approach. Another method known as PCS decompose X into its principal components (which are basically the eigenvectors of X as regressors on Y) using singular value decomposition method as follows:

$$X = S\Delta V' \tag{2.7}$$

where,

$$S'S = V'V = I \tag{2.8}$$

Here, S and V are the matrices of the left and right singular vectors with Δ representing a diagonal matrix having the singular values at the diagonal. According to their respective singular values, the singular vectors are ordered. Singular values, however, corresponds to the square root of the variance of X explained by each singular vector.

Columns of the singular vectors, S are used to predict Y using standard regression approach. A standard regression approach can be applied at this stage because orthogonality removes the problem of multi-collinearity but still, we need to choose the number of the optimum subset of predictors or variables. This could be done by retaining first few components that could explain X better. However, there is an issue with this approach and the issue is that those first few optimum subset of predictors explains X well and it doesn't guarantee that they appreciably explain Y as well.

Partial least square regression solves this problem by decomposing both X and Y together to find components of X that are also relevant to Y. The method determines a set of components called "Latent vectors", which are found by considering the covariance between X and Y and thereby generalizing principal component

analysis. Regression method is used next to predict Y using the decomposition of X.

2.5.3.2 Simultaneous decomposition of predictors and dependent variables

Partial least square regression decompose X and Y as a common set of orthogonal factors (scores) and loadings (need not be orthogonal). Predictor set X is decomposed as, $X = TP'$, with $T'T = I$ such that I is the identity matrix. Analogous to PCA, T is called as score matrix and P as loading matrix. Similarly, Y is decomposed as, $\tilde{Y} = TBC'$, where B is the diagonal matrix with regression weights at the diagonal, C is the weight matrix of the predicted variable, $\tilde{Y}$. Columns of matrix T represents the latent vectors.

2.5.4 Ensemble Empirical Mode Decomposition (EEMD)

`Hilbert-Huang Transform` De-trending and determining the intrinsic oscillations encapsulated in a complex signal like the weather or climate time series is a challenging task. For this purpose a method known as, Empirical Mode Decomposition (EMD) was developed Huang et al. [1998]. EMD forms the fundamental part of Hilbet Huang Transform. The method is similar to the wavelet and fourier transform in terms of decomposing the original signal into its constituent components. These components are nearly orthogonal in nature and are called as intrinsic mode function. Unlike the Fourier Transform method, EMD does not assume a priori based analysis and is, therefore, a suitable tool for detecting the multiple periodic components in an underlying time series. This decomposition method is based on a basic assumption that any data consist of a finite number of intrinsic modes. These intrinsic modes are basically the components of oscillations and are known as, IMF, Intrinsic Mode Function. The signal is decomposed in time domain and thus the IMFs possess the same length as that of the original signal while preserving the varying frequency. This quality makes this method essentially useful to analyze real life non-stationary and non-linear signal, for example, real world signal which includes multiple causes occurring in different domains. IMFs satisfy the following two main criteria:

1. While considering the entire dataset, the number of extrema and the number of zero crossings should be the same or at most differ by 1.

2. The local mean value of an envelope defined by a local maxima and minima is locally 0 *i.e.* the envelopes are symmetric about 0.

Hilbert Spectral Analysis

This method examines each IMFs instantaneous frequency as a function of time to give a frequency-time distribution of signal amplitude. This is done to identify the localized characteristics of the signal and this technique was later named as Ensemble Empirical Mode Decomposition. Thus, EEMD reduces the original signal into it's finite number of orthogonal components of intrinsic modes to which Hilbert spectral analysis is applied. IMF has a simple oscillatory mode with varying amplitude and frequency about the time axis, unlike a harmonic function. The method used to extract IMF is called shifting. First, all the local extrema in the signal are determined. All the local maxima and minima thus found are connected by a cubic spline fit as the upper and lower envelopes respectively. These upper and lower envelopes cover all the data points. The mean of the two envelopes, m_1, is then subtracted from the signal to get the first component, h_1.

$$y(t) - m_1 = h_1 \tag{2.9}$$

In this type of shifting, the new crest represents the local maxima and the troughs, the local minima. In the second round of shifting, h_1 would be considered as the original over which the two envelopes are generated. Mean of the two envelopes, m_{11} is subtracted from h_1 to get the component, h_{11}. Thus,

$$h_1 - m_{11} = h_{11} \tag{2.10}$$

Consider this shifting process "i^{th}" times. Then,

$$h_{1(i-1)} - m_{1i} = h_{1i} \tag{2.11}$$

where, h_{1i}, is labeled as the first IMF component,

$$c_1 = h_{1i} \tag{2.12}$$

The number of time the shifting process takes place is decided by the stoppage criterion. **Stoppage Criterion:** There are four standard stoppage criteria to decide the number of shifting processes.

1. **Standard Deviation:** Similar to the Cauchy's convergence test, and defining the total difference as, SD

$$SD_i = \Sigma_{t=0}^{T} \left| \frac{h_{i-1}(t) - h_i(t)}{h_{i-1}^2(t)} \right| \tag{2.13}$$

   The shifting process terminates when the SD_i comes out to be smaller than the SD_{i-1}, (from the previous step)

2. **S-Number Criterion:** S is a predetermined trial number which decides the number of shifting steps taken until the number of zero crossings and the extrema are equal or at most differ by 1.

3. **Threshold Method** This method fix two threshold values so that the mean fluctuations are globally small.

4. **Energy Different Tracking:** This method assumes that the original signal is a composition of the original signal and is a composition of the orthogonal signals, and calculate the energy based on this hypothesis.

The first IMF, incorporates the shortest oscillations of the signal. This first IMF is then subtracted from the original signal to obtain the residue, $Y(t) - IMF_1 = r_1$. The residue, r_1 constitutes the longer oscillations and is treated as the new base data set for the next shifting process. This cycle goes on until we obtain a trend, a line or a curve without the waves, *i.e.* when the function (residue) becomes monotonic and no more IMFs can be clipped out of it.

2.5.5 Bilinear Interpolation

This method interpolates in both, X and Y, directions and is an extension of the 1-D linear interpolation technique over a 2D grid and Z in case of 3D. This method could be considered as one of the simplest interpolation technique and possess advantages as well as disadvantages. Bilinear interpolation is a distance weighted averaging resampling method. The method estimates a new value based on the

4-nearest distance-weighted averages 2.14. Briefly, the equation can be given as follows:

$$Z = B_0 + B_1X + B_2Y + B_3XY \tag{2.14}$$

where, B_0, B_1, B_2 and B_3 coefficients are computed using four equations corresponding to the reference points. (http://web.pdx.edu/~jduh/courses/geog493f09/Students/W6_Bilinear%20Interpolation.pdf)

Bilinear interpolation method uses a distance-weighted average of 4 nearest neighboring cells. Thus there are 4 coefficients (B_0, .. B_3). The method does not demand a regular square grid. Z represents the interpolated value in 3D. By convention, we could replace it with Y in case the of 2D.

Chapter 3

Simple Methods for Estimating Tropical Cyclone Intensities

3.1 Introduction

The theoretical upper bound on a tropical cyclone intensity is termed as its Potential Intensity (PI) (Emanuel [1995, 2005a]). The Potential Intensity (PI) can be calculated using Sea Surface Temperature (SST), Sea Level Pressure (SLP), Atmospheric vertical profile of temperature, and Mixing Ratio (Emanuel [2007], Bister and Emanuel [2002]). The algorithm is based on the evaporation-wind feedback mechanism, the Wind-Induced Surface Heat Exchange (WISHE). It is a positive feedback mechanism between the atmosphere and ocean. According to this mechanism, a stronger ocean to atmosphere heat flux results in a stronger atmospheric circulation, which in turn causes a strong heat flux. Evaporation is primarily determined by the magnitude of the surface winds. Thus the mechanism involves bulk aerodynamic enthalpy transfer. The method does not use latent heat release as the driving mechanism for vortex amplification but used it as an aspect of the axisymmetric model where the latent heat is implicit. The mechanism also showed that CAPE is not necessary for storm intensification.(1.1)

The Power Dissipation Index (PDI) estimates the theoretical upper limit of TC intensity and depend upon PI (Emanuel [2005a]). Technically, a cube of the maximum wind speeds sustained for a period of one minute when summed gives us the PDI. This sum is considered at an intervals of six hours. The index quantifies the destructive potential of the storms.

3.1.1 Modeling TC Intensification

There are three major techniques developed to explore the subject of TC intensification. All approaches have their relative merits for the intended applications and their potential areas of improvements. A few of these merits and demerits are presented below.

First Technique: Potential Intensity

Most of the published work on the subject examines the TC potential intensity based on atmospheric thermodynamics and equations governing atmospheric flows (Emanuel [1986, 1995, 1988], Simpson et al. [1997]).

Strengths: (1) The method presents the idea that under ideal conditions (and under the assumptions made) TC intensifies using the self-induced heat transfer from the ocean. The idea has been supported by several studies (Emanuel [1986]). Heat fluxes maintain the TC against dissipation against friction.

(2) It introduces the Carnot cycle analogy for the first time to simplify the TC model from the thermodynamic point of view (Emanuel [1986],Emanuel [1988]).

Weakness: Boundary layer physics and the dynamics of the eye have not been accounted for in the study. Lateral mixing of heat, momentum and water could have potential consequences for the structure and dynamics of the eye.

Second Technique: Numerical Models

Another approach to determining cyclone intensity is based on time-dependent numerical modeling technique (Rotunno [1987]). This method considers a weak TC seeded into a known environment. The model is then integrated in time until the cyclone's maximum intensity is accomplished (Rotunno [1987], Persing and Montgomery [2005]).

Strengths: (1) This method extends the first approach to computing Tropical Cyclone Intensity (TCI) for axisymmetric storms and presented more accurate

results than the first Technique by generating storms weaker by 10% than those generated by the first method which is more comparable to the observational data.

Weakness: This technique is subjected to errors associated with numerical discretization and parametrization (Rotunno [1987])

Third Technique: Empirical

The third technique uses observational data to statistically find cyclone intensity and is a function of observed ocean-atmospheric variables like SST (DeMaria and Kaplan [1994], Zeng et al. [2007], Whitney and Hobgood [1997]).

This is because it is well-known that a higher Sea Surface Temperature (SST) is assumed to offer a supportive environment for TC formation and intensification but, it is equally true that vertical thermodynamic profile of the atmosphere also contributes towards TC genesis and intensification (Emanuel [2007], Bister and Emanuel [2002], Shen et al. [2000], Holland [1997b]).

Strengths: (1)The empirical relation developed by the third approach provides a simple and easy to use the method to determine the maximum potential intensity close to the tropopause, and to determine the outflow temperature, both of which are assumed to be a function of SST. The model was developed for the North Atlantic Ocean (DeMaria and Kaplan [1994]).

Weakness: (1) Climatological SSTs used to develop the model, instead of daily or weekly data, to compute the intensity of TCs. This was done to simplify the model. So, the model may not be good enough for estimating TCI at high temporal resolution, weekly or monthly. Also, the climatology was averaged over 31 years between 1962 through 1992, which dis-includes the intense storm data which occurred after 1992.

The present work thus follows the steps of the first and third method stated above. We are interested to know what physical variables are most important in determining the theoretical peak wind speed in TCs using Emanuel's PI approach (Emanuel [1986, 1988]).

A previous study using 45 years statistical regressions has shown that SST has a dominating influence in high hurricane seasons, independent of all other known factors, and that sea warming explained $61 \pm 34\%$ ($mean \pm StandardDeviation$) of the anomalous Atlantic hurricane activity at 95% confidence level in 1995 (Saunders [1997]). On investigating 1995 hurricane season in the North Atlantic Ocean using regression analysis on about 45 years of TC activity data exhibited SST to be the statistically dominant factor in driving TCs. The 1995 hurricane season under investigation had a demarcated activity of twice the 50 years average number of storms (Saunders [1997]).

Using SST climatology and the TC's maximum potential intensity data for a period of 31 years (1962-1992), an empirical relationship between the two is constructed. This empirical model is tested against Emanuel's theoretical model and also with observation based dataset. A good agreement between the model and the observational data was found when the tropopause temperature is assumed to be a function of SST. It is found that only 20% of the Atlantic Hurricanes reached 80% of the maximum possible TC potential intensity and, on an average only up to 55%.

A considerable interannual variability in the potential intensity data was also found (DeMaria and Kaplan [1994]). Following the similar approach, another empirical relationship between SST and the TC maximum potential intensity was developed from a 31 years sample (1963-1993). This model was compared to an established empirical relation and also with the theoretical results. In the North Pacific, only 11% of the storms were found to reach 80% of the estimated intensity while 19% were found to reach in the North Atlantic Ocean. It was found that during the westerly phase of Quasi-Biennial Oscillation (QBO), a higher percentage of storms reaches their theoretically maximum potential intensity (Whitney and Hobgood [1997]). Similarly, another empirical model developed to compute maximum potential intensity using SST between 1981 to 2003 dataset computed slightly higher TC potential intensity as compared to the findings in earlier studies. The relationship developed was suitable for the Atlantic Ocean only and also included the effect of thermodynamic efficiency in its later stages. Thus, the maximum potential intensity was better approximated than did previously (DeMaria and Kaplan [1994]) when compared to the observations (Zeng et al. [2007]).

Motivated by the demands to comprehend TC potential strength in a simple and easy way for the hazard planning and management, we explore a simplified statistical relationship between TC intensity and physical variables (primarily SST) influencing it. Another motivation for this study is to gain better understanding of the linear and non-linear factors influencing Tropical Cyclone Potential Intensity.

Detailed background on the topic along with the associated literature review follows next in the section(3.2). We try to answer these questions using data and methodology stated in section(3.3). Turning towards the results and discussions which are presented in section (3.4), various figures to assess the hypothesis are presented.

3.2 Theoretical Background: A steady state analytical TC model

Considering a highly idealized axisymmetric, steady-state TC, a model was developed (Emanuel [1986]) based on two primary assumptions. First, the flow above a well-mixed surface boundary layer is inviscid and secondly, it is thermodynamically reversible. These assumptions assured the safe usage of hydrostatic and gradient wind balance.

C_D represents the surface drag coefficient which quantifies the resistance of an object in a fluid environment. According to Emanuel (1995)'s theory (Emanuel [1995]), a TC can maintain it's kinetic energy if the energy supplied by oceanic heat sources is at a rate exceeding dissipation. Thus for a mature TC, Ce/Cd ranges as, $1.2 < Ce/Cd < 1.5$. At extreme winds, greater than 50 m/s, the drag coefficient found in most models cause kinetic energy to be destroyed. If Cd is set to 0, no system scale intensification occurs Michael et al. [2010].

The density ρ of surface air fluctuates by 15% approximately and the drag coefficient C_D increases with cyclone's wind speeds by a factor of 2. However, the Drag Coefficient settle around wind speeds of 30 ms^{-1} (Powell et al. [2003]).

Simplified form of TC intensity, referred to as Power Dissipation Index (PDI), in terms of V_{max} is given by,

$$PDI = \int_0^{\tau} V_{max}^3 dt \tag{3.1}$$

The index (PDI) represents total frictional dissipation of kinetic energy in the TC boundary layer. Over the lifetime of a storm.

Here, V_{max} represents the maximum sustained wind speeds at 10 metres above the surface. TC's PI is a better indicator of the threat of the storm than the frequency or intensity alone (Emanuel [2005d]). V_{max}, the PI associated with TCs is quantitatively represented as,

$$V_{max} = \sqrt{\epsilon \frac{C_k}{C_D}(k^* - k_B)|_M} \tag{3.2}$$

Where, "M" represents the quantities at the radius of maximum winds.

Simplicity of the equation(3.1) and its relevance to defining destructiveness in association with a tropical cyclone, we have made use of this index instead of traditional indices, which demand a range of input parameters.

It is well-known that SST plays a vital role in cyclone genesis and intensification (Miller [1958], Palmen [1948b]). However, SST on its own is insufficient to determine TC intensification. For instance, Atlantic storm, "Earl" in 1992, attained a maximum speed of 28 ms^{-1} at SST of about 27 °C while, Atlantic hurricane Bonnie, during the same season, gained maximum speed of 49 ms^{-1} with ocean temperature of about 25 °C (DeMaria and Kaplan [1994]).

An empirical relationship between ocean temperature and TC's maximum sustained wind speeds during a period of time ranging between 1962 and 1992 was developed (DeMaria and Kaplan [1994]). The designed empirical model to determine TC wind speeds were found to be an exponential function,

$$V_{max} = C_0 + C_1 \exp^{C_2(T - 30\,^\circ\mathrm{C})} \tag{3.3}$$

Where, maximum attained TC winds, V_{max}, is in ms^{-1} and C_0 (= 28.2 ms^{-1}), C_1 (= 55.8 ms^{-1}), & C_2 (= 0.18 °C) are the constant values. This model signifies SST as an upper bound on TC's intensity. However, other environmental factors contributing to it determine the actual intensity of a TC. We extend this idea further

to determine a simple model to quantify TC intensity as a function of difference between the ocean temperature and the lowest level atmospheric temperature (AT_1), (SST- AT_1)), which in turn depends on SST and thereby concluding a relationship to computing TC intensity directly from SST itself. This is one of the primary aims of this Chapter.

Total power dissipation in a TC is proportional to the cube of wind speed (Emanuel [1998]). Integrating the power dissipation over the surface area affected by a storm over its lifetime, τ, gives the potential intensity,

$$PI = 2\pi \int_0^{\tau} \int_0^{r_o} C_D \rho V^3 d\tau dr \tag{3.4}$$

where, C_D represents the surface drag coefficient, ρ denotes the surface air density, V is the magnitude of the surface winds. The limit on the integration on the storm's radius ranges from storm's centre, referred as '0' in the limit, to the outermost spiralling band at r_o (meters).

3.3 Data and Methods Used

3.3.1 Methodology

In this work, observational reconstructions were used to explore the connection between ocean temperature and maximum surface wind speed, V_{max}, have been utilized. Thus quantified V_{max}, is then applied to compute TC's Power Dissipation Index (PDI), an index to quantify upper limit on cyclone's destructive potential (Bister and Emanuel [1998], Emanuel [2007], Bister and Emanuel [2002], Holland [1997b], Emanuel [2000]). A schematic representation of the method to obtain V_{maxNw} is shown in figure (3.1). The figure(3.1) can be briefly stated as follows.
V_{max} = f($\triangle T$),
$\triangle T$ = f(SST,AT_1)

Where, $\triangle T$ refers to the difference between the SST and the low level atmospheric temperature (AT_1). $\triangle T$ correlates fairly well with SST. Thus, simplifying the two functions above,
$\Rightarrow V_{max}$ = f(SST)

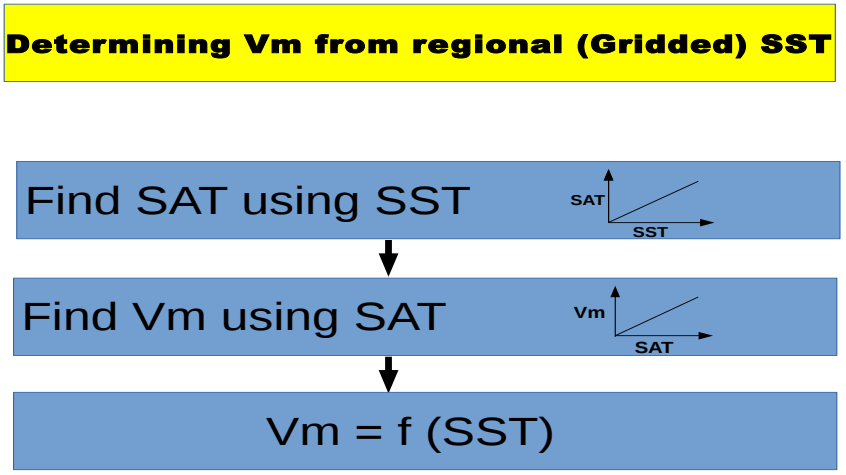

FIGURE 3.1: Methodology to compute spatial distribution (gridded) of V_{maxNw} from SST (gridded).

Local SST has a tendency to influence the atmospheric sounding above and effect the PI of a Cyclone, (Emanuel [2007], Shen et al. [2000], Holland [1997b]). The first part of this work make use of observation derived reanalysis datasets, to construct a simple statistical model to determine (tropical and) local maximum sustained wind speeds, V_{max}, from (tropical and) regional SSTs. Temperature anomalies of the troposphere also depend on variation in tropical SST (Sobel et al. [2002]).

This simple model is applied to SST data sets (Smith et al. [2007], COBE-NOAA [2015], NOAA [2014]) ranging from 1880 (Smith et al. [2007], NOAA [2014]), & 1891 (COBE-NOAA [2015]) onwards which enables the model suitable for computing cyclone's strength spatially during the pre-satellite era.

The second part of this work focus on exploring the spatiotemporal variation of V_{max} derived using the relation built-in the first part.

3.3.1.1 Similarity and Differences between COBE and ERSST.V3b

Similarity: Both the data set has one data source in common, i.e. ICOADS (International Comprehensive Ocean-Atmosphere Data Set)
Differences:

1. Data in case of COBE has been accumulated from ships, buoys and reports while the missing data in case of ERSST.V3b has been filled in using statistical methods.

2. ERSST.V3b uses advanced bias correction algorithms as compared to COBE where the later uses primitive methods as in Folland and Parker [1995].

3. ERSST.V3b is used as input for the merged land-ocean surface temperature product.

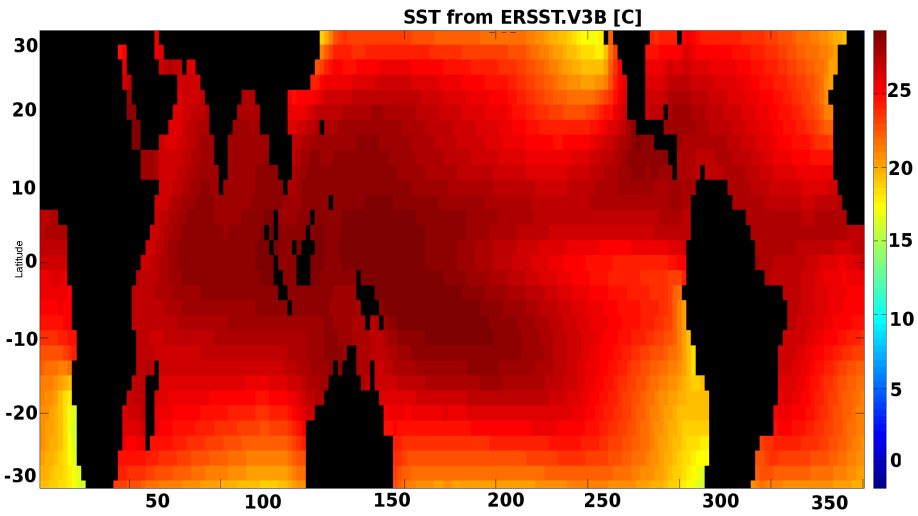

FIGURE 3.2: Tropical distribution of monthly mean SST. The SST values are averaged between 1982 (January) through 2013 (December). Tropical distribution of SST is obtained from $ERSST.V3b$ dataset(Smith et al. [2007])

Considering these three data sets (Smith et al. [2007], COBE-NOAA [2015], NOAA [2014]) during the same time, the departures of the SST.COBE and OISST.V2 from the SST.V3b averaged over the same period of time (January, 1982 to December, 2013), are shown in figure(3.3) and figure(3.4). On an average, SST.V3b illustrates warmer ocean phase as compared to the COBE dataset and comparable values to that of the OISST.V2 dataset, with greater differences in the ocean temperature in the North Atlantic Ocean and the West Pacific Ocean.

3.3.1.2 Computation of sustained wind speeds

Spatial linear correlation between V_{max} and ocean-atmospheric temperature contrast, $\triangle T$, is computed using Pearson's moment correlation method. Similarly, the relation between $\triangle T$ and SST is tested. The significance of both the correlations is tested using the Bootstrap method, a method of random sampling with replacement (Efron and Tibshirani [1993]).

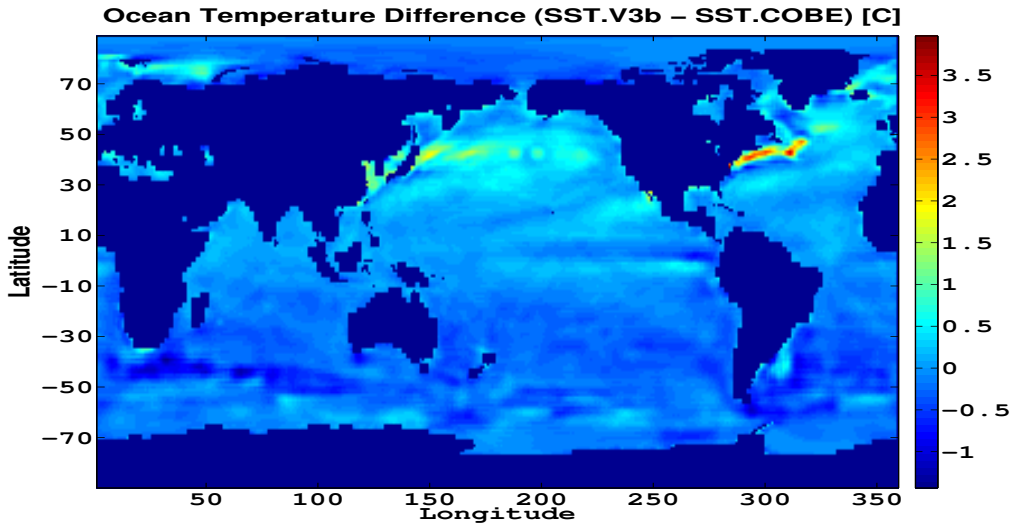

FIGURE 3.3: Departure of SST.COBE data set from SST.V3b. On an average, SST.V3b shows lower temperature than the SST.COBE data with a few exceptions in the North Atlantic and the West Pacific.

3.3.2 Data Used

1. **Reanalysis Data:** Reanalysis data set is a comprehensive record of weather and climate dataset. It incorporates observations and numerical weather model outputs to estimate the state of the system. Such datasets cover the entire globe from the earth's surface to well above the stratosphere.

   A monthly mean SST, sea level pressure, mixing ratio, and atmospheric temperature reanalysis datasets provided by the National Centers for Environmental Prediction (NCEP)/National Center for Atmospheric Research (NCAR) is used as input to determine tropical cyclone strength using an algorithm based on the thermodynamic model for cyclone intensity. Unlike SST Smith et al. [2007], COBE-NOAA [2015], NOAA [2014] and SLP (Kalnay [1996]) which are considered at surface level, atmospheric temperature and mixing ratio (Reanalysis [2014]) are considered in the vertical atmosphere. Atmospheric soundings are available up to the lower stratosphere for 16 pressure levels (plus the surface). SST is expressed in °C, SLP in mb, atmospheric temperature in °C and the mixing ratio in g/kg. The value of mixing ratio ranges between 0 g/Kg in cold continents to 20 g/Kg for the warm tropical areas (Levine [1995]).

   Sustained wind speeds, V_{max}, are derived using reanalysis datasets, monthly

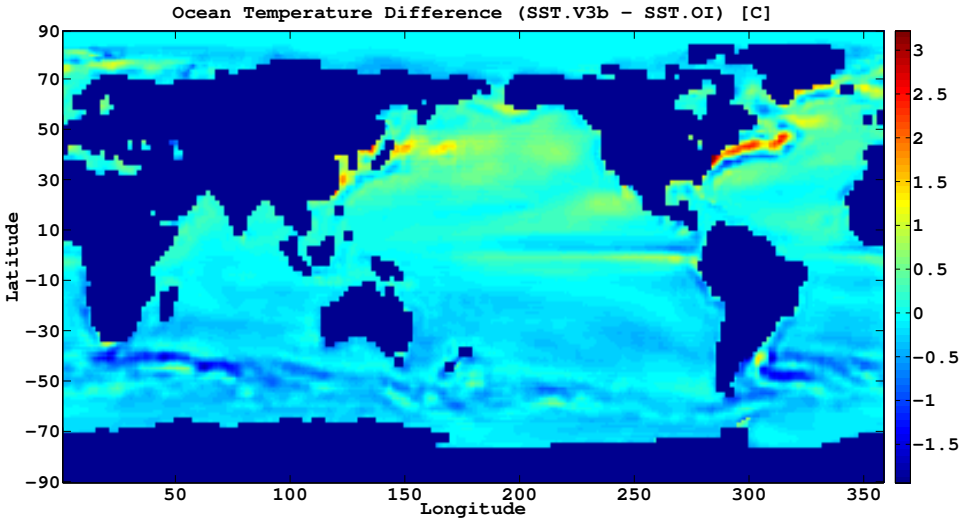

FIGURE 3.4: Departure of OISST.V2 data set from SST.V3b. On an average, SST.V3b and SST data sets presents similar values, with a few exceptions in the North Atlantic and the West Pacific.

mean atmospheric temperature, sea level pressure, SST, and specific humidity as input to the algorithm available at `ftp://texmex.mit.edu/pub/emanuel/TCMAX/`.

The reanalysis dataset is consistent over the spatial and temporal domains which are the major **advantage**.

However, observational constraints at a few locations, over a period of time leads to the reanalysis reliability issues which is a big **disadvantage** of using this kind of dataset and thus should be considered with caution.

TCPI as computed from the full calculation and that from the ocean temperature only has been shown in the figure (3.7). The upper panel of the figure presents the V_{max} and the spatial distribution of the V_{maxNw} has been illustrated on the right. V_{maxNw} represents the TCPI metric. The metric was modeled statistically in this chapter, eq (3.5).

Higher values of the V_{maxNw} as compared to the V_{maxNw} in a few regions can be seen in the figure (3.2) and it also comes out clearly in the difference plot (figure 3.5). However, this figure portrays appreciable spatial similarity in the two models in the tropics. The similar comparative graphs can be seen for the other two SST data sets, SST.COBE and OISST.V2, in the figure (A.8) and figure (A.4) respectively.

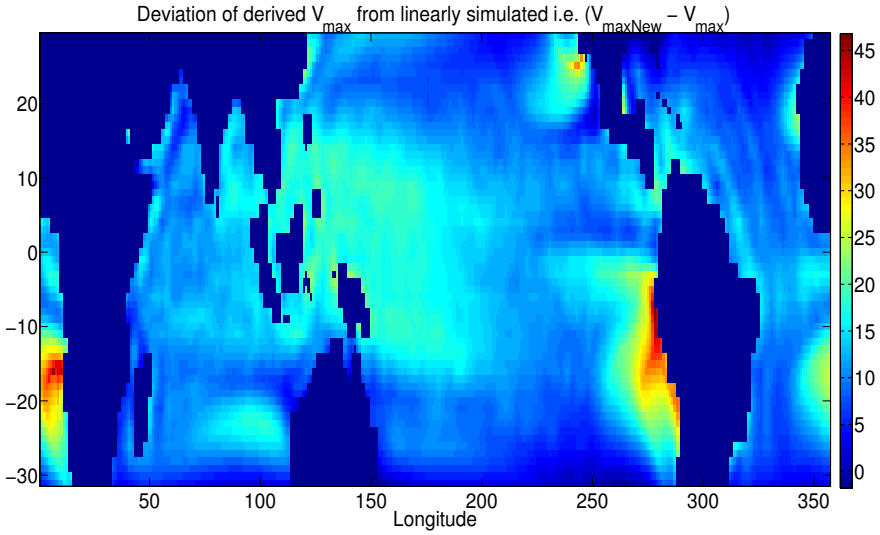

FIGURE 3.5: Spatial distribution of the difference between the peak winds speeds as derived from thermodynamical model and that obtained from the linear statistical model developed here. (Using SST.V3b)

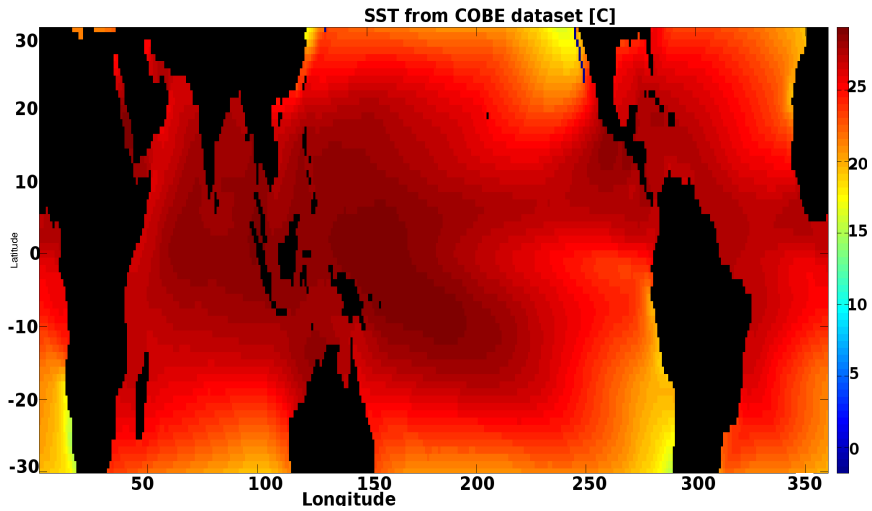

FIGURE 3.6: Tropical distribution of SST from COBE dataset (COBE-NOAA [2015])

3.3.3 Tropical Distribution of SST From Three Different Datasets

Distributions of SST using three datasets considered is shown in the Figures(3.2, A.2, & 3.6). It can be seen that the three datasets show similar temperature patterns in the tropical ocean. Correlation of these SST datasets with corresponding $\triangle T$ and with V_{max} is high for all the SST datasets. However, the third version SST dataset (3.2) shows the best significant correlation and is thus used for further analysis.

3.4 Results and Discussion

3.4.1 Development of a linear V_{max} Model and its validation against an established model

Based on the assumptions that V_{max} and SST (all SST values in the tropics) are correlated, at least to a first order approximation, we have performed a linear regression ($r^2 = 0.9534$) for the averaged datasets described in Section(3.3.1.2). Subsequently, the model is applied for climatological averaged values and also a time series analysis was performed in Section (A.2).

Here, we denote our modeled V_{max} as, V_{maxNw}.

$$V_{maxNw} = 6.3 * SST - 102 \tag{3.5}$$

A strong liner scatter was observed for SST values ≥ 16.5 C. Below this, the scatter was disoriented and hence the relation. Thus, we suggest not using this model for SST values lower than that.

Reliable NCEP reanalysis dataset provided by NOAA/PSD (Smith et al. [2007]) used to determine sustained speeds, V_{max}, from 1947 onwards by employing thermodynamic model to compute V_{max} as described in (Bister and Emanuel [1998]) shows appreciable spatial linear correlation with ocean-atmospheric temperature contrast, $\triangle T$ ($r^2 = 0.95$). Local ocean-atmospheric temperature contrast is in turn significantly correlated to local SST ($r^2 = 0.98$). Owing to these strong correlations, linear regression model developed between SST & $\triangle T$, is as follows:

$$\triangle T = 0.79 * SST + 36 \tag{3.6}$$

V_{maxNw} as obtained from our statistical model Equation(3.5) also shows a significantly high correlation with that of V_{max} obtained from Emanuel's model ($r^2 = 0.9534$).

How good is our TCI model for tropical region? The assumptions behind our approach to formulating a simplistic approach to computing V_{max} only from

cyclone-prone SST value and regions are two-fold: (a) TC's V_{max} values and sea-air temperature contrast ($\triangle T$) are correlated, and (b) SST and air temperature (AT) values are approximately related and, thus, are sea-air temperature contrast and SST. On the first assumption, the time-evolution of V_{max} and $\triangle T$ have been shown to be identical in their directions (not amplitude) during phases of intense storms [*cf.*, Zhu and Zhang [2006]], due to enhanced vertical transport. (An off-line analyses also showed significant spatial linear correlation with sea-air temperature contrast.). Secondly, mean AT, calculated employing the mean value theorem, cf., Equation A18 in Davis et al. [1985], has been subsequently shown to be related to surface temperature (T_s) in a linear way. Various researchers have used this formulation where the form of the equation remains the same but the coefficients vary depending on the area of their study. For example, $AT = 55.8 + 0.77T_s$ is reported in [Bevis et al. [1992], also see Figure(A.1) therein] for their study area.

We have not used these values but made the assumption that $\triangle T$ and SST are correlated with a scatter permissible for our purposes and developed a linear relationship between SST and V_{max}, whose reliability is tested further using two independent inputs. The SST Vs $\triangle T$ relation used here is shown in the equation(3.6).

In order to validate these modeled TC wind speed, both against an established method (Bister and Emanuel [1998]) and across different SST inputs, we calculate both V_{max} and V_{maxNw}, for each of the three SST data as inputs. Results using COBE [COBE-NOAA [2015], NOAA [2014], Smith [2008]] are shown in Figure(A.5), and using ERSST.V3b and OISST.V2 are shown in Figure(A.5) and Figure(A.6), respectively. We acknowledge that this simplistic linear model can be improved, by including more parameters to reduce the scatter, however, as we show here, this model works well for V_{max} in the tropics, especially for the higher values. In addition, our goal is to be able to use and provide other simple users with an easy-to-use model based on parameters that are readily available and in a timely manner. Figure(3.7) provides a visual comparison of V_{max} from two different outputs, from Emanuel's model and from our simplistic model, using SST.COBE as input.

The structural resemblance between Figure(3.7, A.5) (row 1) and Figure(A.5) (row 2) implies that V_{maxNw} is capable of capturing most of the V_{max} structures in the tropics, which is encouraging given our simplistic approach. However, on an average, our model shows somewhat higher V_{max} values of 2.89 ms^{-1} mean difference

as seen in Figure(A.5) (row 4). These 'higher differences' are relatively evenly distributed to a smaller magnitude throughout the tropics, and distinctly off the coasts of Angola, Namibia, Senegal and Peru to higher magnitudes. These higher values are seen on the histogram in Figure(A.5) (row 4) as 0.45% points beyond "$Mean \pm 4xStdDev$".Supplementary figures show analyses as in Figure(A.5), but using ERSST.V3b (Figure(3.7) and OISST.V2 (Figure(A.6), as SST inputs. For Emanuel's model, additional data for other required parameters have been used. The results of Figure(3.7) and Figure(A.6) are consistent with observations from Figure(A.5), with a slight change of statistical parameters, and hence are excluded from re-discussion for brevity.

In order to remove the bias of 2.89 ms^{-1}, we take off the value from the equation, (3.5), the final model equation becomes,

$$V_{maxNw} = 6.3 * SST - 99.11 \tag{3.7}$$

The peak wind speed, V_{max} (figure (3.7), panel 1), derived from full calculations using reanalysis data sets are comparable to the simplistic wind speed, V_{maxNw}. V_{max} which is derived using atmospheric temperature, sea level pressure, specific humidity possess the highest values near the equator. However, this area lacks the required Coriolis force and thus the wind speed beyond this region is considered. On an average, the tropical region in the northern hemisphere possesses higher wind speed than that in the southern hemisphere. Wind speed in the Southeast Pacific, close to the North America in the Northeast Pacific, and around the coast of Africa in Southeast Atlantic are negligibly small (figure (3.7), panel 1a).

The bias and an offset in the mean seen in the figure (3.7), can be attributed to the regions where the simple model fails. A possible reason for which has been provided in the section(3.7). The same explanation has been provided in support of the mean bias noticeable in the table (3.1)

High correlations between SST and V_{max} simulations for the three datasets (as mentioned later in this section) correspond to a linear relation between the two variables, thus simplifying the calculation of PDI, at least to a first order approximation. As shown in Table(3.1), the results of this simplistic approach are overly consistent with a more elaborate approach that, however, requires a range of inputs. It is also important to mention here that this approach is valid only

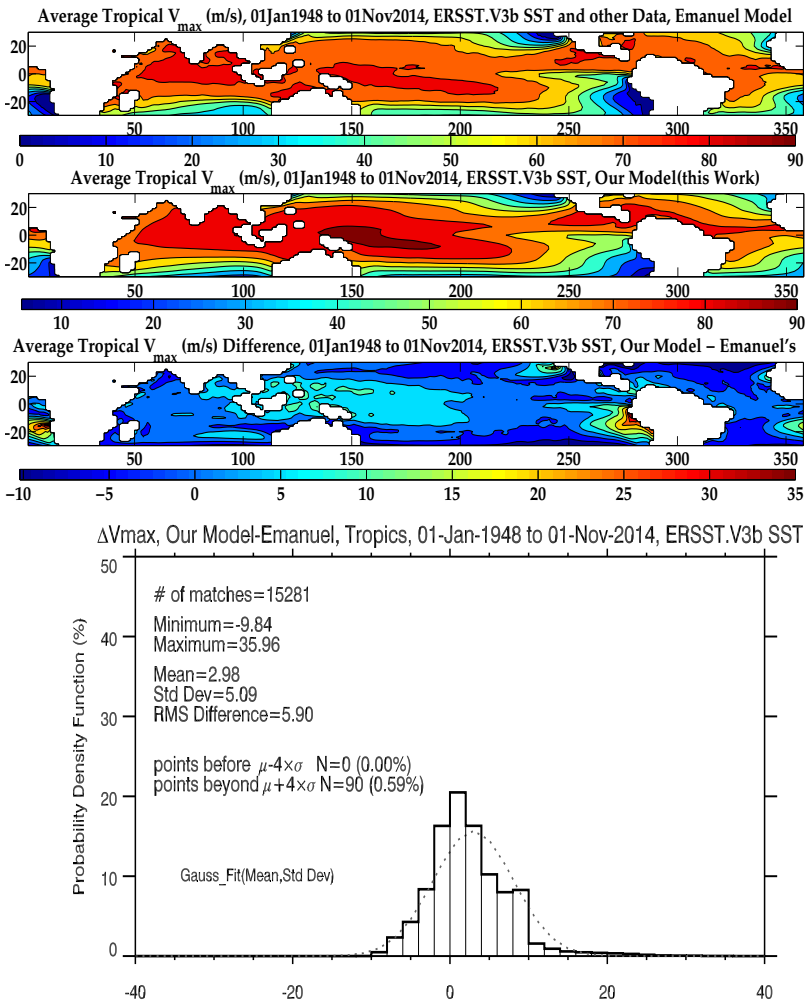

FIGURE 3.7: Comparison of cyclone wind speed V_{max} obtained from Emanuel's model and our simplistic empirical approach with only SST as input. Row-1: V_{max} employing Emanuel's model with reanalysis datasets as inputs: SLP, specific humidity and atmospheric temperature profile and ERSST.V3B (SST); Row-2: V_{maxNw} employing our approach (Equation 3) with ERSST.V3b (SST); Row-3: Spatial distribution of V_{maxNw} minus V_{max} to visually identify areas of disagreement, considering V_{max} as a benchmark (reference), Row-4: Probability density function (PDF) of 'δ V_{max} = V_{maxNw} - V_{max}'. Statistical parameters (number of V_{max} matches, minimum, maximum, mean, standard deviation, root mean square difference), a Gaussian fit, X N(mean, Std Dev) and number of grids beyond " Mean ± 4xStd Deviation", henceforth called 'extreme grids', are also annotated on the PDF.

for time-integrated low-spatial resolution datasets (e.g., monthly mean averages at 1°X1° latitude-longitude grids) and for SST conditions suitable for TC genesis. By no means, however, does it imply that this relationship between SST and V_{max} will hold globally for all SST values and in short time-scales. (For example, on a daily scale and in daytime low wind speed conditions with reduced mechanical mixing, warming will be higher.) Put differently, on short time scales and high spatial resolutions, SST only cannot predict instantaneous 10 m maximum wind-speeds.

The minor dissimilarities across outputs of various SST inputs, e.g., OISST.V2 and SST.COBE can be further attributed to minor variation in the distribution of SST across the datasets. The discrepancy between the considered SST products can be attributed to the difference in the statistical reconstructions used to find SST values in the regions where data was not available. A second reason could be in association with the techniques applied in collecting various SST datasets, for instance, going from the "Bucket method" to the "Hull method". In the Bucket approach, SST is considered to be the water temperature of buckets of water taken from oceans. In the "hulls of ships" method, SST is measured using sensors placed on the hull of a ship. The data products use both in situ and satellite data to obtain SST covering all the ocean basins on earth. (Note that, the cause of differences in SST is not the focus of this study; readers are referred to Reynolds et al. [2002],NOAA [2014],Smith et al. [2007],COBE-NOAA [2015],Martin et al. [2012],Dash et al. [2012] for more information on blended analysis SST fields.)

We have also studied the effect of differences between various SST analysis fields on the model output (figures not shown for brevity). For example, $\triangle T$ and SST as obtained from Martin et al. [2012] and SST.COBE, respectively, show significant correlation ($r^2 = 0.98$) and so do $\triangle T$ and V_{max} ($r^2 = 0.93$). These strong connections are then verified using the bootstrapping method Efron and Tibshirani [1993]. Modeled TC wind speeds, V_{maxNw}, is appreciably connected with a linear correlation of $r^2 = 0.90$ to the storm winds as computed from reanalysis datasets (figures not shown). Another set of SST values (OISST.V2) employed to compute V_{maxNw} also give high correlation with V_{max} ($r^2 = 0.89$). These results thus validate our statistical model and add more confidence to it.

The above mentioned high correlations are reconfirmed by values of p in our analysis, where, p is a matrix of $p - values$ to test the hypothesis of no correlation. The $p - values$ tested here are for the correlation between COBE-SST and V_{max}

derived using it along with the other input variables. Element of the matrix on i^{th} row and j^{th} column is denoted as, p(i,j).

Each $p - value$ represents the probability of getting a correlation as large as the observed value by random chance when the true correlation is zero. If p(i,j) is small, say less than 0.05, then the correlation is significant. In our case, the p-value was found to be zero. This was further tested at $\alpha = 0.05$ for (n-2) degrees of freedom using an alternative t-test statistic to determine the significance. According to this test, we can reject the null hypothesis that there is no correlation if the t-calculated is larger than the t-critical. We found the following values:

1. $t_{calculated} = 485.4131$
2. $t_{critical} = 1.6449$

Since, $t_{critical} < t_{calculated}$, we can reject the null hypothesis as mentioned above and can infer that the correlation is significant. Since reliable atmospheric temperature profiles before the satellite-era at remote regions are unavailable, we make use of a relationship between PDI and SST which can be used to determine TC power in remote regions. It is known that maximum TC wind speed is better correlated with ocean-atmosphere temperature difference than with SST. That is, though warmer SSTs contribute towards a highly supportive environment for TC strengthening, its formation and intensification are strongly influenced by the contrast between ocean temperature and the vertical thermodynamic profile of the atmosphere above it. However, this result suggests that when vertical moisture content and SLP are not available, SST values alone can be used by simply employing the linear regression model suggested here to approximate TC wind speeds, V_{maxNw}, and hence the intensity of a cyclone, reflected by the PDI.

The spatial departure of the TCPI as computed from full calculations and that from V_{maxNw} is shown in the figure(3.5). On an average, V_{maxNw} matches the V_{max} values in the tropics with a few exceptions. V_{maxNw} shows higher values around the coast of South America in the Southeast Pacific (not a very cyclone-prone region), in the Northeast Pacific around the coast of North America and to the South of Africa in the South Atlantic Ocean, not a very cyclone prone zone either. These exceptions, however, indicate model (V_{maxNw}) failure. A probable cause of such a failure has been explained in the section(3.7)

SST.COBE Input			
V_{max} (ms^{-1})	Emanuel implementation V_{max}	Our Model V_{maxNw}	$V_{maxNw} - V_{max}$ (Validation by comparison)
Minimum	0.24	0.70	-14.36
Maximum	94.90	92.24	38.87
Mean	66.60	69.07	2.89
Standard Deviation	16.51	16.86	5.35
RMS Difference	-NA	-NA	6.08
ERSST.V3b input			
Minimum	0.24	5.64	-9.84
Maximum	92.81	91.87	35.96
Mean	65.99	68.79	2.98
Standard Deviation	16.80	16.98	5.09
RMS Difference	-NA	-NA	5.90
OISST.V2 input			
Minimum	0.76	0.14	-14.18
Maximum	99.08	93.72	39.61
Mean	66.35	70.08	4.13
Standard Deviation	16.45	16.93	5.40
RMS Difference	-NA	-NA	6.80

TABLE 3.1: Summary and intercomparison of tropical cyclone wind speed obtained from Emanuel's model and our approach with only SST as input. Comparisons are performed for three different SST inputs: SST.COBE, ERSST.V3b and OISST.V2. Other parameters (SLP, specific humidity, atmospheric temperature profile) required for implementing Emanuel's model are from NCEP reanalysis datasets.

3.5 Spatial Distribution of SST

It is observed in Figure(3.2) that higher sea surface temperatures responsible for tropical cyclone intensification are prevalently present along the equator and primarily accumulated in the Northern Hemisphere. In general, the Northern Hemisphere is warmer than the Southern Hemisphere, mostly due to more landmass and less ocean surface in the north and the fact that sea-water heats up relatively slowly Kang and Seager [2012].

Owing to a wider area occupied by the Pacific Ocean and warmer SSTs in the Pacific, in comparison to other oceans, a higher amount of heat energy is available

to an evolving TC. However, vertical atmospheric sounding also contributes to cyclogenesis (Section 4.1). SST and theoretically maximum sustained winds speeds, V_{max}, show roughly similar structures (cf., Figure(3.2) and Figure(A.4(a))).

3.6 Model Verification: ACE vs V_{maxNw}

The Accumulated Cyclone Energy (ACE) index is used here to validate the developed model, V_{maxNw}. V_{maxNw} primarily quantifies TC PI and by definition does not take into account the duration of the individual TC event. The ACE index however includes TC intensity and its duration. It describes the destructive power and the activity of the individual TC over a TC season. By definition, the square of by definition, square of the sustained maximum TC wind speed (in knots) every six hours when scaled by a factor of 10000 leads to ACE 3.6.

$$ACE = 10^{-4} \Sigma V_{max}^2 \tag{3.8}$$

While V_{maxNw} is a theoretical parameter which presents plausibility of TCI in a given environment, ACE, on the other hand, is an observed parameter.

Both, ACE and V_{maxNw} quantify TC destructive potential and hence the associated intensity. None of the two indices takes storm dimension into account. Thus, both share the properties marginally and can be used for validation of one over the another.

Here, the V_{maxNw} time series has been obtained by spatially averaging the V_{maxNw} values, averaged over the North Indian Ocean, North Atlantic Ocean, Northwest Pacific, South Indian Ocean and the Southwest Pacific Ocean. Both the ACE and the V_{maxNw} are monthly values, spanning a period of 45 years, between 1970 to 2014.

Since the ACE index was not independently available over the South Indian Ocean and the Southwest Pacific Ocean, but over the Southern Hemisphere, we used the mean of the V_{maxNw} time series over Southwest Pacific Ocean and South Indian Ocean to represent the V_{maxNw} time series over the Southern Hemisphere. It is worth mentioning here that the aerial span of each of the ocean basin considered

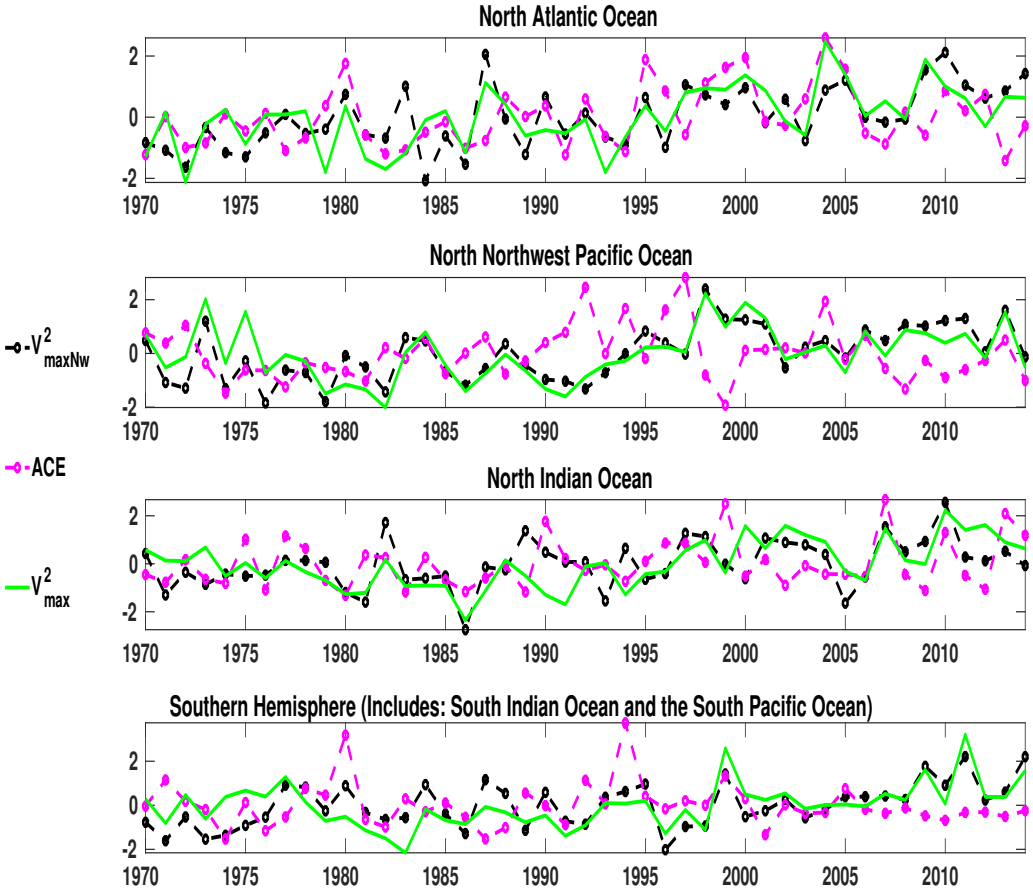

FIGURE 3.8: Standardized variation of ACE and V^2_{maxNw} between 1970 through 2017 (X-axis). The overall correlation between the ACE and V^2_{maxNw} can be seen in the table, 3.2. The two signals vary comparatively closely in the North Atlantic, North Indian Ocean and the Southern Hemisphere.

by V_{maxNw} may be different from that of ACE which could lead to significant difference in their magnitude. Also, ACE takes into account the duration of a seasonal storm, unlike V_{maxNw}. This is another caveat that comes into the picture while verifying V_{maxNw} relative to ACE (figure(3.8) & table(3.2)).

Since ACE is proportional to the square of the wind speeds associated with TCs, we used square of V_{maxNw} for the comparison purposes. Here, we used Pearson's Moment Correlation Coefficient as a means of comparison and hence verification of V_{maxNw} against the ACE index. Despite the caveats involved, a reasonable correlation between the monthly ACE index and V^2_{maxNw} was observed in the considered ocean basins, except in the North Indian Ocean.

In a nutshell, a fair correlation between the observation based ACE and theoretical

Ocean Basin	r: ACE & V^2_{maxNw}	r: ACE & V^2_{max}	r: V^2_{maxNw} & V^2_{max}
North Atlantic	0.34	0.51	0.65
Northwest Pacific	-0.13	-0.09	0.83
Southern Hemisphere	0.10	-0.02	0.66
North Indian Ocean	0.33	0.23	0.55

TABLE 3.2: Pearson's moment correlation coefficients (r) between the observed index, ACE, ${V_{max}}^2$ and ${V_{maxNw}}^2$. ACE, which is traditionally documented in units of $Knots^2$ has been changed to $(ms^{-1})^2$ by taking its product with the factor of 0.544^2 to match the units of ${V_{maxNw}}^2$ and ${V_{max}}^2$. The indices are considered over the North Indian Ocean, North Atlantic, Northwest Pacific and Southern Hemisphere. The reasonable correlation between the observed and the theoretical parameters proliferate our confidence in the usability of the model. The table compares the correlation coefficients of the observed seasonal ACE data with the V^2_{maxNw} and ${V_{max}}^2$

V_{maxNw} in the North Indian Ocean and the North Atlantic attributes towards the strength of employing the index developed here for research purposes vastly and operational usability marginally.

Low acceptance in the Southern hemisphere could be attributed to the lack of good quality data in the basin and the inhomogeneous nature of the ocean temperature in the basin which is a subject of further research.

3.7 Model Limitation and Possible Explanation

The figure (3.7) reveals that the simple model fails to quantify TCPI around the coast of North and South America, and a region surrounding the coast of Africa in the Southeast Pacific. A possible cause of such a failure has been discussed in this section. Convection is an important mechanism to drive the primary circulation and the secondary circulation in a tropical cyclone (TC). Convection is initiated using symmetric thermal perturbation at a vertical height of about 2 Kms (Wissmeier and Smith [2011]). Thus, considering the lowest layer of atmospheric temperature profiles, we attempt to determine the heat transfer from the ocean floor towards the atmosphere above it. Convective cooling occurs at the sea surface by a collective movement of particles via the evaporation by which TCs gain energy thereby causing the lowering of the sea surface temperature underneath. This convective cooling, also known as the Newton's law of cooling, is given as,

$$\frac{DQ}{DT} = hA(T_{surf} - T_{env}) = hA\Delta T(t) \tag{3.9}$$

where, Q is the thermal energy in Joules, h is the convective heat transfer coefficient (W/m^2K), A is the heat transferring area and T is the temperature of the object (SST), T_{env} is the environmental temperature (K). Now, $\Delta T(t) \equiv (T(SST) - T(AT_1))$, where, $T(AT_1)$ denotes the atmospheric temperature at the lowest level. Considering similar areas and similar values of the h which does not vary widely over the SST with similar characteristics, we can restate the equation to a certain degree of approximation as (*Cf*:Bergman et al. [2011]), defining, $h_c = (h * A)$ we get,

$$Q' = (T_s - T_{env})/(1/h_c) = (T_s - T_{env})/R_c \tag{3.10}$$

Where, h_c, represents the convection coefficient and R_c is the unit convective resistance.

Now, referring to the regions in the figure (3.9) showing abrupt mismatch with the V_{maxNw} values in figure (3.7) as,

1. West Coast of North America
2. African coast close to the Gulf of Guinea
3. South American Coast
4. The Arabian Sea in the North Indian Ocean
5. Off the coast of Namibia

Please note that an equal number of grid boxes are used over the considered regions for the computation as shown in the figure(3.9).

As can be noticed from the table(3.3), comparatively, higher atmospheric temperature above would suppress the evaporation from the ocean and hence the convection which fuels the TCs. Since this aspect is missing in our model, which is based on SST only, it gives higher V_{max} values.

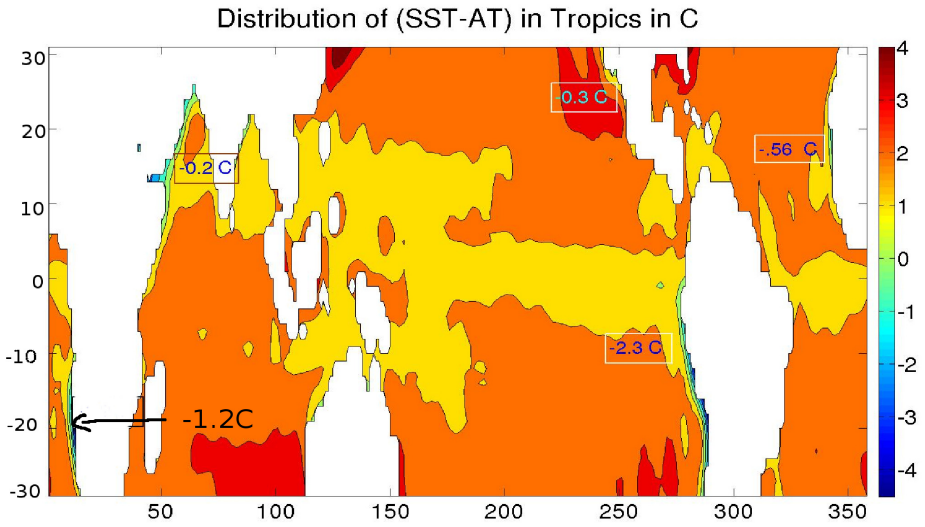

FIGURE 3.9: Spatial distribution of the difference of SST and AT at lowest layer of the atmosphere. Considered regions, where the model fails are indicated with an outline.

Regions	$Q' * R_c$ [°C]
1	-0.3
2	-0.56
3	-2.3
4	-0.2
5	-1.2

TABLE 3.3: Convective heat rate at the 5 regions where the V_{maxNw} failed

3.8 Summary and Conclusions

The study aimed to understand dependency of TC intensification on the environmental factors like ocean temperature, ocean-atmospheric heat exchange, relative humidity and the sea level pressure. It was identified that ocean-atmospheric energy exchange and predominantly, the ocean temperature acts as the governing factor.

According to the simple linear model developed based on significant correlations between the SST and TC intensity, it is possible to determine TC intensity primarily using only SST values, with somewhat sub-optimal but acceptable performance, when other data (SLP, atmospheric mixing profile, and atmospheric profile) are missing. In this chapter, we explored this possibility using a simplistic approach, where the results indicate that they match another evolved model to the first

degree of approximation for climatologically averaged datasets. This gains importance in light of the fact that it is challenging to obtain parameters like mixing ratio and other atmospheric temperature profile variables at remote, less accessible locations or for retrospective studies during the pre-satellite era. In our future work, we will first extend the method to reduce the scatter using other parameters and then test its performance on different categories of tropical cyclones using available data for known major cyclones.

Interestingly, the correlation between oceanic-atmospheric temperature differences and simulated surface wind speeds is stronger for major cyclones (belonging to category 3 or more). That is, stronger storms follow the linear relationship obtained through this model better than weaker storms. One possible explanation of this could be the role of WISHE (Wind Induced Surface Heat Exchange) in deciding the weaker or stronger storms (in terms of V_{max}) and hence their relation with the oceanic-atmospheric temperature difference.

Model analysis shows that high surface wind speeds responsible for stronger TCs are located in relatively lower up to approximately 20° latitudes in both the hemispheres. Also, the Northern Hemisphere warms more and usually experiences higher cyclone winds than the Southern Hemisphere. Surface wind speeds and minimum pressure associated with TCs are significantly anti-correlated (expected) when averaged over the tropics. This anti-correlation holds appreciably in all the considered ocean basins.

In a futuristic prediction by a climate model, both tropical SST and a storm's surface wind speeds increase. The computed difference between the two V_{max} values (with and without when using a doubled CO2 scenario) in the Indian Ocean and West Pacific and the North Atlantic Ocean indicate a rise in PDI when doubling CO2 in our environment.

The following is a summary of the key observations:

(a) Correlation between the ocean temperature and V_{max} is stronger for intense, high category storms, (b) Northern Hemisphere shows comparatively stronger storms than the Southern Hemisphere owing to a higher ocean warming, (c) Minimum pressure and maximum wind speeds are anti-correlated in all the ocean basins (Please refer to the figures in the supplementary chapter) (d) North Atlantic and Pacific Oceans are prone to stronger storms, (e)

The following are the major limitations of this work:

(a) This work employed the WISHE model approach which is also debated in some research results Montgomery et al. [2009]. Thus, we suggest a further investigation using a model closer to the non-axisymmetric spin-up state of an ideal tropical cyclone, and (b) The developed model is based on SST alone which has an advantage while studying tropical cyclone intensity at locations where all the needed atmospheric profiles are missing and SST is available. But, any error in SST will be propagated to the estimated wind speeds as there is no mechanism to prevent error propagation in such an overly simplistic approach.

Chapter 4

Saturation of Tropical Cyclone Strength under a doubled CO_2 scenario

We begin by analysing the sensitivity of the tropical cyclone strength to change in SST. Change in tropical SST alone by 1 °C yields an increase in the peak winds associated with tropical cyclones by about 10 ms^{-1}. (The tropical region considered here does not include 5 ° North and South of the equator due to absence of an appreciable Coriolis acceleration to induce vortical motions in tropical cyclones). The change in the theoretical peak wind speeds associated with tropical cyclones responds weakly to the increasing CO_2 levels. On doubling CO_2 amount, change in peak cyclone wind speed show less response to the increased SST value. This effect appears in tropics and in all the ocean basin considered. This result was verified using two independent data sets. Increasing CO_2 levels were found to induce stronger cyclones, however, their response to SST weakens. We term this as, "Sensitivity Saturation Effect". The effect can be understood as a response of the change in TCI to the change in SST on increasing CO_2 levels.

4.1 Introduction

TCs are a prominent element of the climate system and plays a key role in driving various climatic phenomena. Most of the studies related to TC activity have mainly focused on TC frequency Landsea et al. [1996], Chan et al. [1996] and their track forecasting which is primarily determined by atmospheric flows, while tropical cyclone intensity has received significant attention comparatively recently. With the rise in ocean heat content and documented SST, during the second half of the twentieth century, Levitus [2000], various research work attempt to apprehend what caused the rising SST on TC frequency and intensity Strazzo et al. [2015]. Influence of climate change on the frequency of TC system is still vague with a few studies proposing lowering of TC frequency in North Atlantic basin Zhao et al. [2009].

A study explored the sensitivity of TC's intensity and precipitation rate to various climate models in warming scenario and also under different convection parametrization scheme. Temperature and relative humidity data taken from CMIP2+ CMs showed an overall rise in the wind speed by 6%, incrase in the pressure drop by 14%, and the precipitation rate by 18% Knutson and Tuleya [2003].

Another study anallysed the IPCC B1 scenario along the path of the "low end" radiative forcing. The study reported change in the intensity of TCs with the warming world. Following a high end, A1F1, scenario, lead to even faster rate of change of TCI Knutson and Tuleya [2005].

A simulation of Atlantic hurricane frequency under 21st centruy warming conditions showed a drop in the landfalling hurricanes by 30%. The study also found that as a respons to the increase in the green house gas warming, reduced the TC formation basinwide by 18% Knutson et al. [2008].

U.S. hurricane damage, quantified in terms of it's wind speed only (not included TC rainfall or surge), for IPCC A1B scenario was studied. IPCC's A1 storyline talks about future world of rapid economic growth, global population that peaks in the mid century and then declines due to rapid new and more efficient technologies. A1B emission scenario represents a balanced energy across sources. The study found that 3 out of 4 climate models used, predicted an increasing damage

with time Emanuel [2011].

Both, the IPCC-AR5 and 21st century forecasts report, reports that TC frequency would either decrease or remain constant, while, there is a likely increase in the potential intensity and the associated precipitation rates Jens Hesselbjerg and Krishna Kumar [2013]. According to the future projections, the climate change impacts TC activity heterogeneously. Projections based on downscaling and model resolution of the same while adding confidence in the predictions does not quantify specific characteristics of the changes.

A few studies focusing TC intensity has shown an overall rise in the number of intense hurricanes Emanuel [2013]. Merely SST is not a perfect metric for determining TC's thermodynamics but, tropical cyclone potential intensity depends on the degree of the thermodynamic disequilibrium between upper ocean and the atmospheric profile above Emanuel [1995]. While a later study documented that with change in SST by 1 °C, increase TC's maximum wind speed by 4 ms^{-1} Emanuel [2013]. The present study extends this work and seeks to understand how the variation in SST affects TC strengthening. Then, we try to understand the impact of the unit increase in SST on the TCPI under present-day and doubled CO_2 scenario.

Warmer seas cause stronger TCs (Merrill [1987]) while SST alone is insufficient to decide TC intensity Emanuel [2005d]. The non-linear empirical relation between categorised TCs and SSTs have been proposed previously DeMaria and Kaplan [1994]. A Strong positive connection between SST and TCs with intensities in the upper quantities in the climatological TC intensity distribution was also documented Elsner et al. [2008]. The connection between the two was shown to be stronger when SSTs are greater than 26 °C.

TC power dissipation index, defined as the cube of TC peak wind speeds integrated over their lifetime, has been shown to be appreciably correlated to SSTs (Emanuel [2005d]). Continuing this work further, a framework of spatial tessellation (introduced by Elsner et al. [2012a]) of equal area hexagons was employed. The framework of spatial tessellation of equal area hexagons in medium resolution GCMs, namely FSU/COAPS GCM and GFDL-HiRAM, showed negligible sensitivity of TC intensity towards observed SSTs which is contrary to what was shown in earlier studies. Failure of GCMs to model TCs with peak wind speed over 50

ms^{-1} possibly confines their competence to determine intense TCs with such a precision. Also, inadequacy of GCMs to distinguish inner core thermodynamics of TCs hinder modeled TCs from acting as an idealized heat engines Elsner et al. [2012b].

TC track points and gridded SST values were together superimposed on one another by regressing SSTs over TC intensity. Regressing SSTs exceeding 25 °C (August-October), when averaged over each hexagons onto TCs' maximum intensity magnitudes gives the sensitivity of later on former. While these studies depend upon observations show a connection between SST and TCPI. Modeling studies carried out recently show similar results. Various Global Climate Models (GCMs) and downscaled simulations for 21st century predict increasing TC intensity under various climate change scenarios Emanuel [2013], Knutson et al. [2013], Villarini and Vecchi [2013]. However, present GCMs have too coarse resolution to resolve TC intensity well Chen et al. [2007]. Previous results are subjected to conditions and are warned to be used with caution Strazzo et al. [2015].

Ocean temperature inarguably plays an important role in TC intensification. Models and theories predict an increase in ocean temperature in the warming world. Thus, it is of much scientific interest to see how this rising SST impacts TC intensification which is important for adaptation and mitigation planning. There are two primary aims of this study. First is to quantify the extent to which various natural factors (SST, SLP, atmospheric temperature profile, and relative humidity) contributes towards intensification of TC peak wind speed. The second aim is to quantitatively investigate how the TCPI varies as a response to a unit increase in the SST under present-day and doubled CO_2 scenario. Thus, we compare TCPI's sensitivity towards the ocean temperature under present-day and doubled CO_2 scenario.

The first part of the study, we considered SST, SLP, relative humidity, and atmospheric temperature data from perturbed physics ensembles as derived from HadCM3 and GFDL model runs. we chose the ensembles which were closest to the results obtained from reanalysis data (refer to, (Figure4.1)) (averaged over a course of 67 years, as in Chapter 3).

In order to explore the impact of SST on TC strength, we considered perturbed physics ensembles as derived from HadCM3 model runs and then from GFDL simulations. Despite the importance of SST in TC intensification, there remains

a paucity of analysis explaining the link under climate change scenario. Thus, technically, the study first tries to find the most significant natural variable that influences TCPI. For this purpose, we used the method of partial least square regression to find out the dominant variables affecting TCPI. The method is also useful to quantify the regression model because of its ability to robustly handle descriptor variables Herve [2003].

Remaining work proceed as follows: Section(4.2) Describes data sets and Methods used, and Sections(4.3 & 4.4) discusses Results and Conclusions.

4.2 Data and Methods Used

4.2.1 Data Used

4.2.1.1 UKMO's HadCM3

To assess changes in the TCPI sensitivity as a response to fluctuations in SST when CO_2 concentration is at present day levels and when it's doubled in the environment, we employed a suite of coupled ocean-atmospheric models. A demand for better computation of uncertainties in climate forecast estimates gave rise to the perturbed physics technique (Moore et al. [2001]). In this approach, we consider a single model structure and perturb the magnitudes of uncertain variables, in an allowed range. The range is decided with the help of people involved in parametrization development and by rigorous inspection of the modeling literature. The simulations based on the UK met office model (HadCM3) are referred to as, Qump1, Qump2 and so on are abbreviated here as, q_1, q_2 respectively.

The Hadley Centre Climate Model, version 3 (HadCM3) runs in the present day CO_2 level and then with doubled CO_2 level runs to obtain SST, sea level pressure, relative humidity, and atmospheric profile in the two case scenarios. We use Perturbed Physics Ensembles (PPE) by estimating the mean response of 53 different model versions with changes in their physical parameters involved in the model. There are two primary reasons for exploiting the PPE technique here. First, the method efficiently samples mean climate states in relatively broad bounds (Collins et al. [2010]). Secondly, a wide range of climate forcings and feedbacks are efficiently handled under increased levels of green house gases (like CO_2).

Experimental runs with single models can then be developed in "ensemble mode", depending upon the availability of computation power and time.

Considering a changed climate situation of doubled CO_2, SST thus obtained from the model runs are plugged into an algorithm to quantify tropical cyclone strength, measured in terms of its peak wind speeds.

Before employing the model derived ensembles, we selected seven members which most closely follows the pattern of the re-analysis outputs (Figure4.1). The figure presents distribution of SST as obtained from reanalysis Smith [2008] and from model outputs Collins et al. [2010]. First sub-image at top left reflects SST spread obtained from reanalysis products while other sub-images shows the spread in SST as obtained from HadCM3 runs.

Despite some variation in the magnitude and spread in the model derived products, model results are quite similar to those of reanalysis products, especially in tropics which is where we need it (Figure 4.1).

All of the 16 ensemble members (derived from the perturbation method) were experimented upon and agreed with the findings presented in this work.

But here, we limit ourself to presenting seven members only which qualitatively and quantitatively agree strongly with the reanalysis datasets shown in the Figure(4.1) and as indicated in the table(4.1).

The model derived ensemble members chosen show high correlation with the reanalysis dataset, especially in tropics. This gave us the confidence to choose the data sets, specifically for the tropical region. The correlation coefficients between the model and reanalysis datasets are given in table (4.1)

Technically, TCPI is a measure of thermodynamically derived maximum wind speeds and is thus written as, V_{max} at several places in the equations and the text here. Please note that both can be used interchangeably.

The modeled dataset is bi-linearly interpolated to yield SST and other variables on $1X1$ grid. These downscaled temperature values are then increased by a unit magnitude before using as an input to the algorithm to quantify TC peak wind speed, while keeping other input parameters unchanged. Results obtained from the simulations runs with original SST values (no addition or deduction) are then

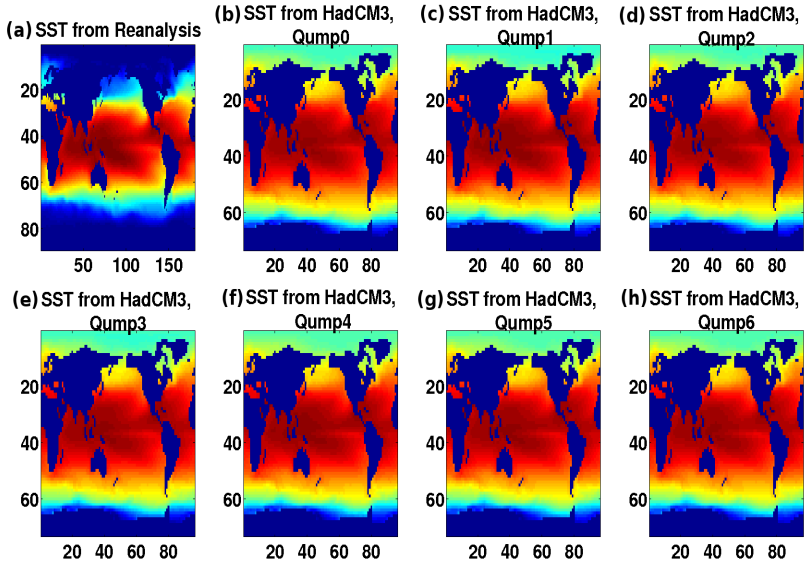

FIGURE 4.1: Graph shows comparison of SST spread as obtained from reanalysis (panel (a)) and that obtained from model runs ((b)-(h)).

,

Variables	Coefficient (r)	Coeff of Determination(r^2)
($SSTq_0$,SST_{Re})	0.9583	0.9183
($SSTq_1$,SST_{Re})	0.9637	0.9287
($SSTq_2$,SST_{Re})	0.9609	0.9233
($SSTq_3$,SST_{Re})	0.9595	0.9206
($SSTq_4$,SST_{Re})	0.9598	0.9212
($SSTq_5$,SST_{Re})	0.9558	0.9136
($SSTq_6$,SST_{Re})	0.9571	0.9160
($SSTq_7$,SST_{Re})	0.9590	0.9197

TABLE 4.1: Pearson moment correlation coefficients (r) and coefficient of determination (r^2) between SST from reanalysis and HadCM3's ensemble members. The Higher correlation coefficient between the reanalysis and the model parameters increase our confidence considering the later for our analysis.

subtracted from those V_{max} values with increased SST. The difference of the two V_{max} values describes the change in TC peak wind speed and hence the associated intensity that would occur when ocean temperature has risen by 1 °C. Difference between the peak wind speeds, ΔV, is obtained as explained by equations(4.2, 4.3, & 4.4). SST reanalysis product is retrieved from NOAA's extended reconstruction of SST (ERSST.V3b), Version 3b Smith [2008]. The resolution was further increased to $1X1°$ by applying bilinear interpolation.

Apart from SST, we have considered Sea Level Pressure (SLP), atmospheric temperature and relative humidity. Atmospheric temperature and relative humidity are acquired in the vertical levels of the atmosphere. From model simulations, atmospheric sounding is available for 16 pressure levels up to the lower stratosphere. The thermodynamic model used here to derive TC potential in terms of its peak wind speed and minimum pressure require specific humidity or mixing ratio as one of the input parameters.

Mixing ratio dataset is not directly obtained from the model output. Thus, we converted the relative humidity to mixing ratio using an algorithm Brunner [2001] which defines the mixing ratio of H_2O per kg of dry air at a particular temperature and pressure. Mixing ratio is computed using the following expression:

$$MR = \frac{m_W}{m_D} = \frac{M_w}{M_D} * \frac{\frac{R_H}{100} * e_s}{p - \frac{R_H}{100} * e_s} * 1000 \tag{4.1}$$

Where,
m_W = Mass of water vapor
m_D = Mass of dry air
M_W = Molecular weight of water
M_W = Molecular weight of dry air
R_H = Relative humidity
e_s = Saturation pressure (hPa) of water vapor
p = Ambient pressure (hPa)

4.2.1.2 GFDL's ESM-CM3

We used data from the most recent world climate research programme, Climate Model Intercomparison Project, CMIP5 (Taylor et al. [2012]). The data set (AT,

SLP, SST, & MR) were part of the earth system model's close carbon cycle project which aimed to study the impact of the climate change on our ecosystem and also the impact of the human activities on our ecosystem. Coupled Physical model (version 3), CM3, was used for the stated simulations. CM3 was developed using CM2.1 (Delworth et al. [2006]) as the starting point. The model aimed to answer the indirect role of aerosols on clouds, chemical interactions and the role of stratospheric chemistry thence ozone. The data set were taken from under the present-day and doubled CO2 scenarios.

4.2.2 Methodology

Using a variety of statistical and mathematical tools, the "sensitivity" of TC intensification to various natural processes, SST in particular, was analysed. Each method has its own advantages and drawbacks. This work uses advanced quantitative regression method, Partial Least Square Regression (PLSR), braided with simple sensitivity analysis for a linear increase in SST. PLSR method is adopted in order to get insight into roles various natural phenomena play while strengthening TCs. The method is especially useful for solving this type of riddle since it doesn't rely on distribution type, collinearity and is also independent of observations, unlike other regression methods. Also, PLSR maintains the predictive nature of the model.

4.2.2.1 Partial Least Square Regression (PLSR)

PLSR method is essentially useful in the cases where there exist factors which possess correlation between themselves and the simple least square method fails or is unreliable. PLSR technique in such a case leads to stable and highly predictive models even when there exist a correlation between the variables. The method primarily relies on a linear transition from a set of estimators (Xs) to a new set of variables called latent variables in a new space. This is achieved by a small number of orthogonal factors. These orthogonal factors are mutually independent estimators. This is where this method varies from the principal component analysis which mainly depends on the latent variables formed on the basis of highest correlation with the dependent variable (Y). PLSR thus contains the smallest number of factors. On increasing the number of factors, PLSR converges to the

classical multiple linear regression methods. PLSR technique basically employs principal components of both, X and Y datasets. The main idea is to establish a regression model between the principal scores (Xs & Ys) of the independent matrix, X, and the dependent matrix, Y, and not between the original matrices themselves. Independent matrix is decomposed into its principal component score matrix (Xs) and a corresponding loading matrix, P in addition to an error matrix, E. (figure4.2)

The climate variables corresponding to the independent variable, Xs are SST, SLP, MR, and AT while the dependent vector, Ys corresponds to V_{max}.

Similarly, the dependent matrix is decomposed into a score matrix, Ys, along with an error matrix, F. These two equations (figure4.2) of X and Y are said to possess an outer relationship. The focus of the PLSR method is to then minimise the norm of F while keeping the correlation between X and Y by the inner relation, Ys = B*Xs.(figure4.2)

While setting up a PLSR model, a major decision is to determine the number of optimal principal components which we estimated by plotting the mean square error corresponding to each component and choosing the number of components corresponding to the minimum error value. For our case, we obtained 4 as the optimal number of components. For this purpose, another recommended method is of cross-validation of the model of varying number of components.

The model most commonly utilizes either NIPALS (Nonlinear Iterative Partial Least Squares) or SVD (Singular Value Decomposition) algorithm to perform iterations in processing the PLSR regression. Out of the two, SVD is faster but, we have used NIPALS to compute the loadings (P, Q) and the scores (T, U). A reason for choosing NIPALS is attributed to its tendency to precisely estimate the latent variables.

PLSR and sensitivity analysis were performed using statistical package available in Mathworks, 2015a. The required but unavailable sub-routines were also written in the same version of Mathworks. The first step in the procedure was to normalise the data sets. The data were normalized to have a zero mean and unit variance. This was done to remove bias by variables having (1) Numerically large values and, (2) large variance.

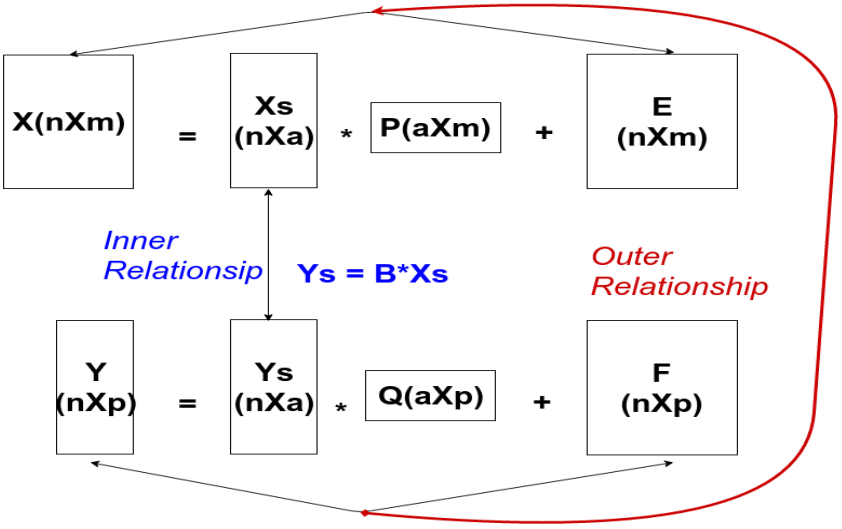

FIGURE 4.2: The figure illustrates PLSR method. X and Y are decomposed into their principal components (Xs and Ys) and loading matrices (P,Q) along with their corresponding error matrices (E,F). The correlation and hence the inner relationship between the scores (Xs & Ys) is stated as, "inner-relationship" ($Ys = B * Xs$) in the figure.

Using this method we obtained input variables which were arranged in descending order of their contribution towards cyclone intensification. From this order, we pick up the first input variable which controls TC intensity the most. To test the impact of the chosen variable (SST) on TCPI, first we used its original value and then the value raised by a unit degree, as done in the sensitivity analyses. Then, we subtracted the TCPI value as obtained with the original SST value from the TCPI value as obtained from the increased SST value. This difference between the two TCPI values thus obtained represents the "sensitivity" of TCPI towards a unit increase in SST. Following similar method, we computed the difference between the TCPIs for a case with doubled CO_2 amount.

4.2.2.2 Sensitivity Analysis

The first step taken towards the sensitivity analysis is graphically explained in figure (4.3). The model is used as an input to determine tropical cyclone strength using an algorithm based on a thermodynamic model for cyclone intensity. The algorithm (Bister and Emanuel [1998]) takes SST, SLP, atmospheric temperature,

and mixing ratio as input variables and yield maximum achievable cyclone winds (TCPI) & theoretically minimum TC pressure (P_{min}) attainable.

$$V_{max_{SST}} = f(SST) \tag{4.2}$$

$$V_{max_{SST+1}} = f(SST + 1) \tag{4.3}$$

$$\Delta V = V_{max_{SST+1}} - V_{max_{SST}} \tag{4.4}$$

Unlike SST and SLP which are considered at surface level, atmospheric temperature and mixing ratio are considered in the vertical atmosphere. Atmospheric sounding is available for 16 pressure levels up to the lower stratosphere. 16 pressure levels considered are, 1000, 925, 850, 700, 600, 500, 400, 300, 200, 150, 100, 70, 50, 30, 20, & 10 mb.

Mixing ratio dataset is not directly obtained from the model output and we converted the relative humidity dataset to mixing ratio using an algorithm Brunner [2001] which defines the mixing ratio in grammes of H_2O per kg of dry air.

Before analysing the "sensitivity" of tropical cyclone strength to its most influential factors, we need to first find it and Partial Least Square Regression (PLSR) method is thus used here. The method regresses V_{max} on the four input factors, SST, Sea Level Pressure (SLP), the Mixing ratio (lowest level), and Atmospheric temperature (AT) (at lowest level).

4.3 Results and Discussions

4.3.1 Analysis Using Partial Least Square Regression

First, the impact of various input parameters on the cyclone intensification was examined using the method of partial least square regression.

This regression method employs partial least square components or latent factors and returns the predictor and response loadings along with the beta factor which

Coefficient (β)	β_{SST}	β_{SLP}	β_{MR}	β_{AT}
Reanalysis	6.333	0.3350	0.0055	0.3990
Model (Q 1)$1XCO_2$	10.5	0.34	0.00	-2.26
Model (Q 1)$2XCO_2$	10.53	0.19	0.001	-2.63

TABLE 4.2: PLSR coefficients (β) corresponding to SST, SLP, mixing ratio (lowest level), and AT (lowest level) from reanalysis and model (HadCM3) datasets

determines the regression coefficients. Regression coefficients obtained from reanalysis dataset are as follows: 6.33, 0.335, 0.0055, and 0.399. Here, the first term denotes the regression coefficient corresponds to SST, the second term shows the regression coefficient of SLP, third to the lowest level of the MR, and fourth is associated with the lowest level of the atmospheric temperature profile. This show that SST, and AT vectors contributes most in quantifying the dependent vector and thus the tropical cyclone strength. The units corresponding to the regression coefficients are as follows. The coefficient, 6.33 corresponds to °C/(ms^{-1}), 0.335 adhere to hPa/(ms^{-1}), 0.0055 to $(ms^{-1})^{-1}$ and 0.399 comply with °C/(ms^{-1}).

While SST corresponds to the highest contribution towards V_{max}, the significance of the results is tested using t-test. Fitting V_{max} values using partial least square regression method gives us new V_{max} values which are tested relative to the V_{max} obtained from thermodynamic model Bister and Emanuel [1998]. The two sample t-test used here confirms at 5% significance level that the two independent dataset comes from the same distribution with equal means.

This study fundamentally explains long term behavior (climatology) and hence the response of the tropical cyclone strength to varying SST. different tropical cyclone prone ocean basins responds differently to the changing SST magnitude locally and globally. Rising SST under doubled CO_2 scenario as obtained from GCM outputs indicate that this increase can be attributed to the increase in green house gases such as, CO_2.

The variable with the highest PLSR coefficient is accounted to pose the highest influence on the TCPI. PLSR coefficient for both, model and reanalysis datasets, are documented in table (4.2).

Last two rows of the table refer to the PLSR coefficients of the input variables,

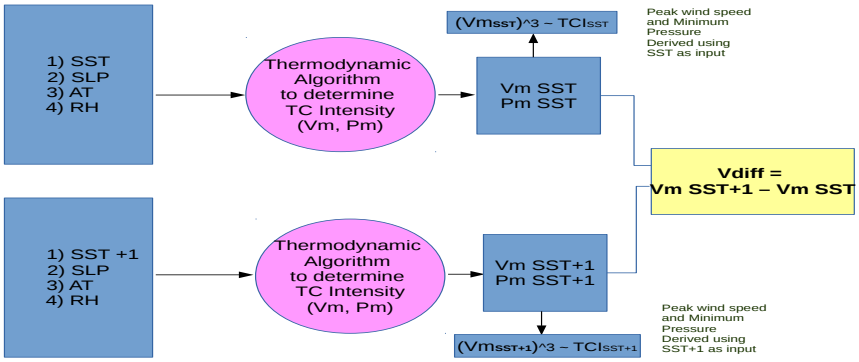

FIGURE 4.3: A Schematic representation of the methodology to compute ΔV.

SST, SLP, MR and AT (MR, AT at lowest level, close to the ocean surface), respectively derived from HadCM3 model under present and doubled CO_2 scenario. The first row presents the PLSR coefficients associated with reanalysis derived SST, SLP, MR and AT. Both, model and reanalysis datasets used for developing the regression model uses tropical datasets at 1X1 degree grid. As can be seen from the table (4.2), coefficient associated to SST is higher than that corresponding to other variables. AT influence Vmax negatively and goes well with the wind-induced surface heat exchange, WISHE, the model concept of the enthalpy exchange between the ocean and AT above, where low AT would enforce the evaporation needed for the intensification. Lower values corresponding to SLP and MR show their feeble contribution towards TCPI intensification.

Here, variables with the highest PLSR coefficient is accounted to pose the largest influence on the potential intensity or on the TCPI. PLSR coefficients for both, model and reanalysis datasets, are documented in the table(4.2). First, two rows of the table refer to the PLSR coefficients of the input variables, SST, SLP, MR & AT respectively, derived from HadCM3 model under present and doubled CO_2 scenarios respectively. The third row of the table (4.2) show the coefficients in the same order as stated earlier where we employed the reanalysis dataset.

As can be seen from the table(4.2), PLSR coefficients corresponding to the SST is significantly higher than that others. Higher AT (at the lowest level, close to SST) influence TCPI negatively and goes well with the WISHE model's concept of enthalpy exchange between the SST and AT, where, low AT would enforce the evaporation and hence the potential intensity.

PMCC coef (r)	SST	SLP	MR	AT
Reanalysis	6.333	0.3350	0.0055	0.3990
1XCO_2 (r)	0.98	0.49	-0.75	-0.095
1XCO_2 (r^2)	0.96	0.24	-0.56	-0.009

TABLE 4.3: Pearson's Moment Correlation Coefficients between TCPI and SST, SLP, MR, & AT derived from model data (GFDL) under present day and doubled CO_2 scenario

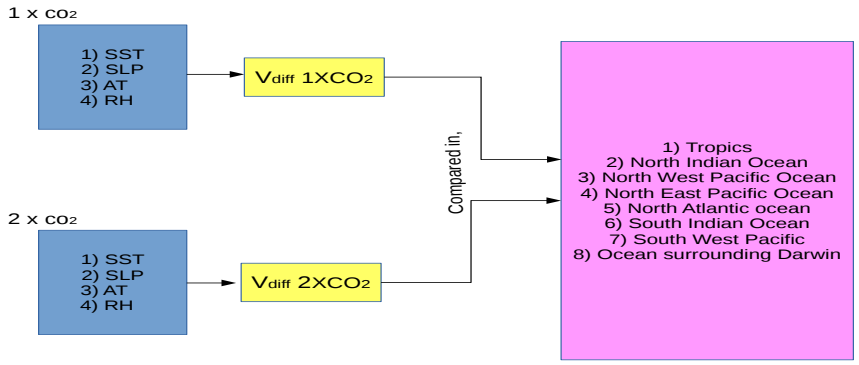

FIGURE 4.4: A Schematic representation of the methodology to compute ΔV under present and doubled CO_2 concentration.

Also, TCPI show higher correlation (Pearson moment correlation coefficient, PMCC) with the SST, as shown in table(4.3). SLP and MR on the other hand show feeble and negative correlation with TCPI. Tropical SST, SLP, AT and MR used here are a model (GFDL) based, under present day CO_2 level.

4.3.2 Analysis Using Histograms

The previous analysis showed us that the peak wind speeds are highly dependent on the ocean temperature. Directed by this result, we define the change in the peak wind speed, as a result of a unit increase in the ocean temperature, given by,

$$\Delta V = V_{max}(SST + 1) - V_{max}(SST) \tag{4.5}$$

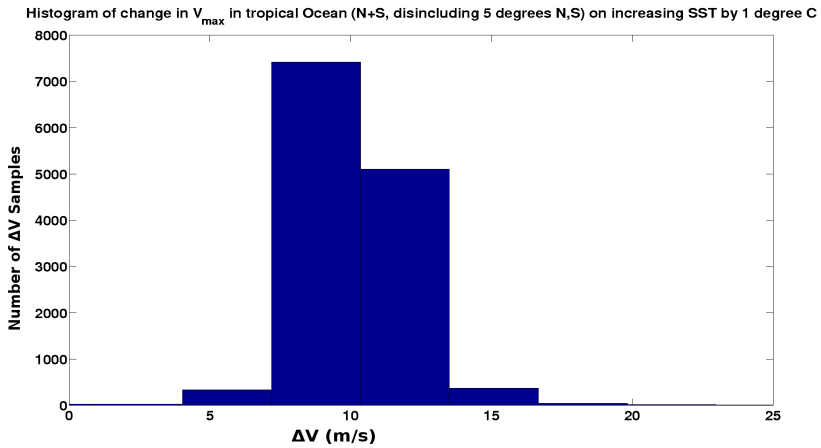

FIGURE 4.5: Under present day CO_2 scenario, change in maximum wind speed, V_{max}, on increased SST by 1 °C averaged over tropics is highest between the range of 8.5ms^{-1} to 10.6 ms^{-1}, which is significantly high (at 5% significance level).

4.3.2.1 Histogram of sensitivity to V_{max} in the Tropical Ocean Basin

A histogram of change in the tropical wind speeds, ΔV, at each grid point is graphed in Figure(4.5). A graphical display of gridded change in TC strength on increasing SST by a unit degree in tropics in form of histogram is shown in Figure(4.5). This bar plot of ΔV distribution is organised in intervals or bins.The intervals having a unit of peak wind speed (ms^{-1}) on the X-axis and the number of grid points, along Y-axis, possessing the associated V_{max} values are represented.

This histogram representation provides important information about the nature of V_{max} data like, the dispersion, the central tendency, and in general shape of the distribution. Here, central tendency is measured in terms of mean and median and dispersion of the data in terms of range and standard deviation. ΔV values averaged over tropics possess quantile values at 0.25, 0.5, & 0.75 to be 9.2 ms^{-1}, 10 ms^{-1} and 11.1 ms^{-1}.

Here, the tropical region does not include 5 °C north and south of equator since the region does not support TC formation owing to lack of Coriolis force that causes vortex turning associated with a cyclone. Less than 25% of the increased V_{max} values are less than 9.2 ms^{-1} in magnitude, $(1/4)^{th}$ are between 9.2 and 10 ms^{-1}. Next 25% values are between 10 and 11 ms^{-1}. Remaining $(1/4)^{th}$ are above 11 ms^{-1}. Change in V_{max} on increasing SST by 1 °C is a unimodal distribution and is positively skewed (Skewness = 0.21 ms^{-1}), *i.e.* on an average, there is an

increase in TC wind speeds by about 10 ms^{-1}, in tropics. T-test performed on the distribution at 5% significance level shows that this positive change in TC wind speed is significant. Unambiguously, V_{max} is highly sensitive to the change in tropical SST. The distribution has kurtosis (Kurtosis = 6.2) slightly more than twice that of a Gaussian distribution with kurtosis of 3 units. That is, most of the grid points (4300) show increase in V_{max} in tropics between 8.5 and 10.6 ms^{-1} Figure(4.5). The histogram graph thus indicates substantial contribution of unit change in SST on TC strengthening. Hence, in tropics, varying SST consecutively influences cyclone intensity.

4.3.2.2 Histogram of sensitivity to V_{max} in the North Indian Ocean

In Figure(4.6), we can see that change in peak wind speeds on increasing SST by 1 °C is positive. We can see a negative skewness in the changed V_{max} distribution (skewness = -0.94) over the North Indian Ocean. None of the ΔV grid values shows decrease in V_{max} on increasing SST. The distribution possesses a kurtosis (Kurtosis = 7.3) greater than 3 and is thus more peaked than a Gaussian distribution. 75%, 50% and 25% quantile values of ΔV are, 9.97 ms^{-1}, 8.9 ms^{-1}, and 8.6 ms^{-1} respectively. Thus, lower than a quarter of the data points are smaller than 8.6 ms^{-1}, 25% of the values are between 8.6 and 8.9 ms^{-1}. Last quarter of values is greater than 10 ms^{-1}. These findings show that in North Indian Ocean, in general, there is a net increase in ΔV values by about 9 ms^{-1} when averaged over North Indian Ocean as a response to increasing in SST by 1 °C

4.3.2.3 Histogram of sensitivity to V_{max} in the South Indian Ocean

Histogram of ΔV in South Indian Ocean is close to consistent with change in maximum wind speed on increasing SST by 1 °C. The graph stretches the range from 0 to 14 (ms^{-1}) while it peaks between 10.7 ms^{-1} to 11.2 ms^{-1} *i.e.* most of the grid points show increase in the peak wind speed by 11 ms^{-1} on an average Figure(4.10).

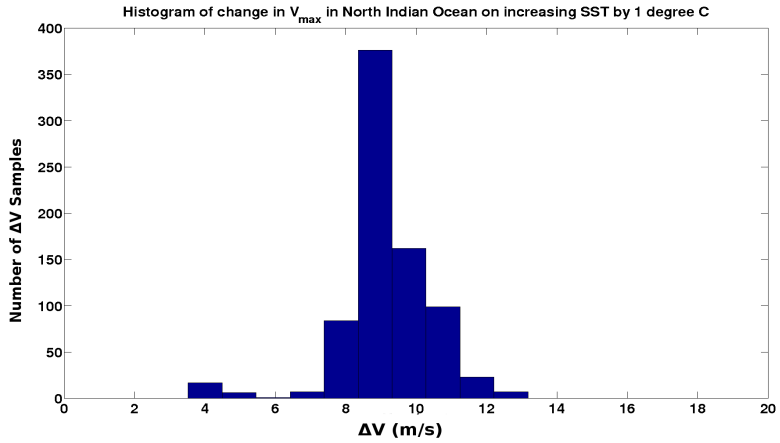

FIGURE 4.6: Histogram of ΔV as response to 1 °C rise in SST. Y-axis denotes the number of grid points possessing ΔV demarcated on abscissa. On an average, increase in V_{max} as response to increase in SST by 1 °C is 9 (ms^{-1}).

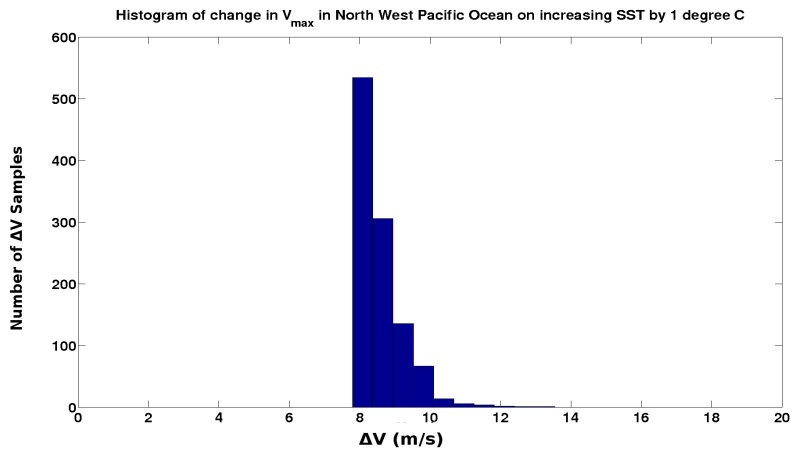

FIGURE 4.7: Histogram representing ΔV in Northwest Pacific Ocean as a result to 1 °C rise in SST. Ordinate denotes the number of grid points possessing ΔV demarcated on X-axis. In Northwest Pacific, all the ΔV values are above 7 (ms^{-1}) with expected increase in ΔV on increasing SST by 1 °C to be 8.4 (ms^{-1}).

4.3.2.4 Histogram of sensitivity to V_{max} in the Northwest Pacific Ocean

Bar plot of ΔV in Northwest Pacific basin is positively skewed (skewness = 1.6). In Northwest Pacific, the average increase in V_{max} on increasing SST is about 8.5 ms^{-1}. Most of the grid points in Northwest Pacific demarcate a positive change in peak cyclone wind speed by about 8.25 ms^{-1} Figure(4.7).

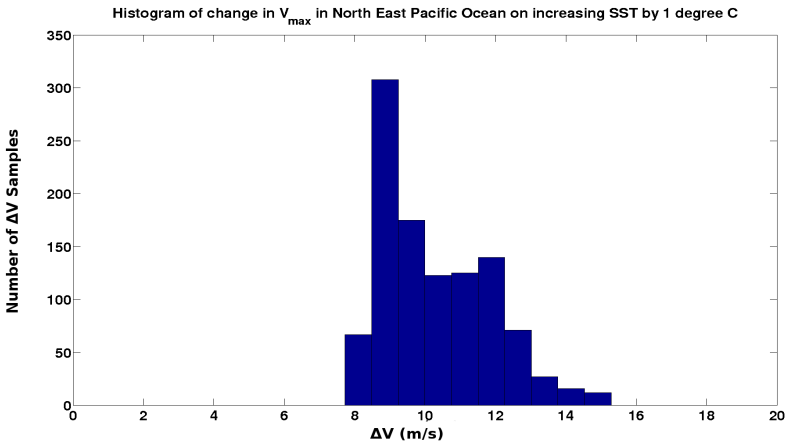

FIGURE 4.8: In Northeast Pacific, distribution of ΔV in Northeast Pacific Ocean is far from Gaussian and it also appears that it is a bimodal distribution. Bimodal characteristic in the distribution is indicative of two merged distributions. The two distributions could be due to overlapping of two ocean basins prone to tropical cyclone formation giving rise to two distributions of ΔV, one corresponding to each basin. V_{max} increase by 8.4 (ms^{-1}) in Northeast Pacific Ocean as response to 1 °C upswing in SST.

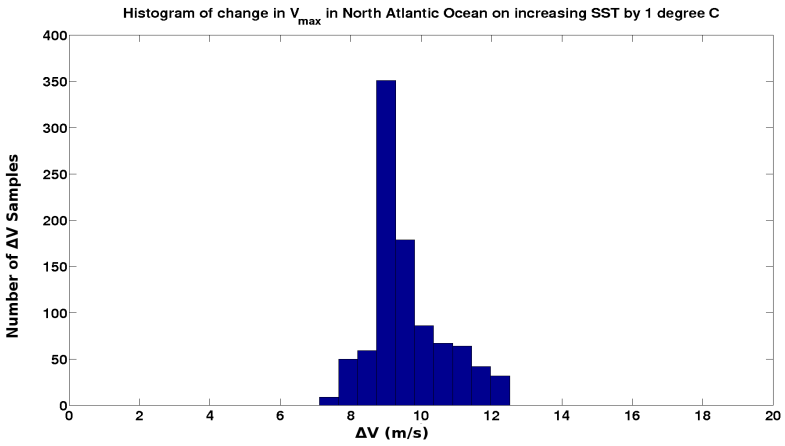

FIGURE 4.9: Histogram of ΔV in North Atlantic Ocean as a response to 1 °C rise in SST. Y-axis denotes the number of grid points possessing ΔV demarcated on X-axis. In North Atlantic Ocean, all the ΔV values are above 9 (ms^{-1}). This distribution is very close to Gaussian with kurtosis of 3.1.

Ocean Basin	Median	Skewness	Kurtosis	Q 0.25	Q 0.50	Q 0.75
Tropics	10	0.21	6.2	9.2	10	11
NIO	8.9	-0.94	7.3	8.6	8.9	10
NWPac	8.4	1.6	6.5	8.1	8.4	8.8
NEPc	9.9	0.71	2.8	9	9.9	11.5
NAtl	9.3	0.79	3.1	8.9	9.3	10.3
SIO	11	-0.1	1.9	9.8	11	12.2
SDrwn	10	1.1	3.4	9.5	10	11
SWPac	9.8	0.2	1.6	8.4	9.8	11.4

TABLE 4.4: Statistics of change in tropical cyclone

4.3.2.5 Histogram of sensitivity to V_{max} in the Northeast Pacific Ocean and North Atlantic Ocean

Results from the histogram of rest of all the considered TC prone ocean basins is shown in the table(4.4). Since median is not sensitive to outliers, we analyze results in table(4.4) and table(4.5) by comparing median values stated. Under doubled CO_2 scenario, ΔV declines in all the ocean basins including tropics. Tropical ΔV decrease by 0.9 ms^{-1}. 1.4 ms^{-1} reduction is observed in North Indian Ocean, 1.1 ms^{-1} decline in Northwest Pacific, 1.6 ms^{-1} in Northeast Pacific, 1.2 ms^{-1} in South Indian Ocean, 1.5 close to Darwin and Jakarta and 1.2 ms^{-1} decrease in Southwest Pacific.

The highest downturn in the "sensitivity" of TCI to SST is observed in Northeast Pacific and least over tropics. However, the skewness of ΔV becomes more positive on increasing CO_2 concentration and thus more grid points have higher ΔV values but spread more. This reduction in ΔV as a response to a unit increase in SST could be explained by the observed increase in atmospheric temperature profile on increasing CO_2 concentration. Increased atmospheric temperature could suppress the amount of heat exchanged between ocean and atmosphere via evaporation from the ocean surface. It's identified that increasing SST would still induce higher evaporation which leads to convection over the sea surface and eventually leading to convective thunder clouds (provided right conditions for cyclogenesis like low vertical wind shear occurs). However, increase in atmospheric temperature substantially can suppress the evaporation content over the seabed meaning thereby decreased sensitivity to increased ocean temperature. The results from this analysis are comparable to the PLSR results which indicated the dominant role of high SST underneath and relatively lower AT above.

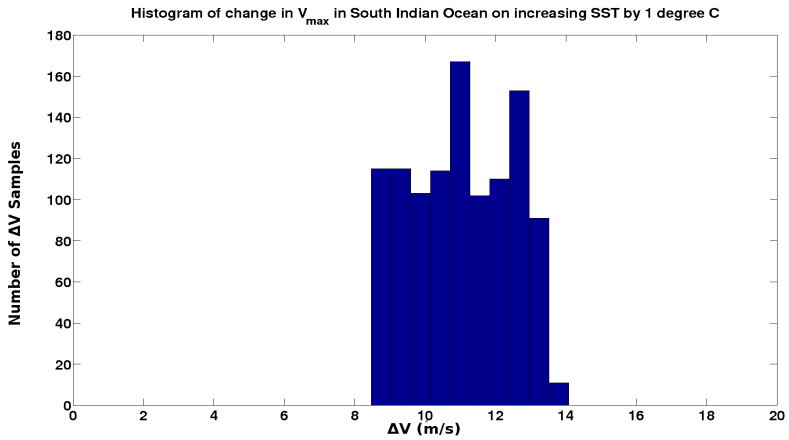

FIGURE 4.10: Histogram of ΔV in South Indian Ocean as a response to 1 °C rise in SST. Y-axis denotes the number of grid points possessing ΔV demarcated on the abscissa. In South Indian Ocean, increase in ΔV ranges between 0 to 14 (ms^{-1}). This distribution show even arrangement of ΔV values across the bins (X-axis values) between 0 to 13 (ms^{-1}). Average increase in ΔV over South Indian Ocean is 11 ms^{-1}.

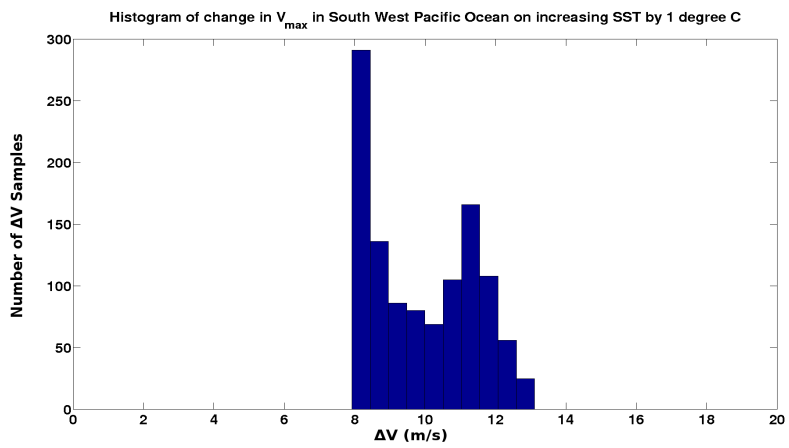

FIGURE 4.11: Histogram of ΔV in Southwest Pacific Ocean as a response to 1 °C rise in SST. Y-axis denotes the number of grid points possessing ΔV demarcated on X-axis. Typical increase in ΔV over Southwest Pacific Ocean is 9.8 (ms^{-1}).

Ocean Basin	Mean	Median	Skewness	Kurtosis	Q 0.25	Q 0.50	Q 0.75
Tropics	9.5	9.1	0.9	5.3	8.3	9.1	10.3
NIO	7.7	7.5	-0.65	6.3	7.2	7.5	8.3
NWPac	7.4	7.3	1.2	4.9	7.0	7.3	7.4
NEPc	8.9	8.3	0.9	2.7	7.6	8.3	10
NAtl	8.3	8.1	0.5	3.5	7.8	8.1	8.8
SIO	10.1	9.8	0.3	1.8	8.5	9.8	11.7
SDrwn	9.1	8.5	1.6	5.1	8.2	8.5	9.4
SWPac	9.1	8.6	0.4	1.9	7.4	8.6	10.6

TABLE 4.5: Statistics of change in tropical cyclone for doubled CO_2 scenario

Ocean Basins	ΔV 1XCO_2	ΔV 2XCO_2
Tropics	10.0868	9.8839
North Indian Ocean	9.2398	8.6577
Northwest Pacific	8.8903	9.2568
Northeast Pacific	10.5793	10.0660
North Atlantic	9.7598	9.3820
South Indian Ocean	11.1751	11.0543
Southwest Pacific	10.1314	10.2110
Darwin	10.4194	10.0581

TABLE 4.6: The decrease in sensitivity of TC strength towards SST with increased CO_2 concentration. On an average, we can notice highest effect in North Indian Ocean and least in South Indian Ocean. North and Southwest Pacific add an exception to this, while the exception is quite small in the southern part of the West Pacific Ocean. Data used, **HadCM3, UK Met Office**

Ocean Basins	ΔV 1XCO_2	ΔV 2XCO_2
North Indian Ocean	9.56	6.6
Northwest Pacific	9.44	6.70
Northeast Pacific	10.04	6.94
North Atlantic	10.77	6.97
South Indian Ocean	9.44	6.4
Southwest Pacific	8.41	5.9

TABLE 4.7: Table compares ΔV in six tropical oceans (averaged over equal areas), under present and doubled CO_2 concentrations. Lower values of ΔV represents the lower sensitivity of change in ΔV to a unit increase in SST. All the tropical ocean basins stated in the table above, North Indian Ocean, Northwest Pacific, North Atlantic Ocean, Northeast Pacific, South Indian Ocean, and Southwest Pacific, illustrates the reduced sensitivity of ΔV (towards SST) on doubling CO_2 concentration. Data used, **CMIP5, GFDL**

In order to test the significance of the values stated in table(4.7) and (4.6), we performed 2-tailed test (since we were unsure if the value is expected to be on the higher or lower end). As a null hypothesis, the values as given in the tables(4.7) and (4.6) were considered and an alternate hypothesis around it was constructed. For the given mean (μ), the sample size, n, standard deviation, s, of the sample (X), the test statistic employed is given as,

$$t = \frac{(\bar{X} - \mu)}{s/\sqrt{n}} \tag{4.6}$$

A significance level of 5% was considered for all the tests. The p-value, denoting the probability of observing a test statistic as extreme as the observed value under the null hypothesis, was then computed. Here, the small p-value cast doubt on the validity of the null hypothesis. The p-value obtained in each of the ocean basins were close to 1, higher than 0.90 at a 5% significance level. Thus, the values given in the tables (4.7) and (4.6) are significant at 5% significance level.

4.3.3 Sensitivity Analysis

The lower values of ΔV in the table(4.12) represents lower sensitivity of change in TCPI to a unit increase in SST. All the tropical ocean basins stated in the table show reduced "sensitivity" of ΔV towards SST on doubling CO_2 amount. The table compares ΔV in six different tropical ocean (averaged over equal areas) under 1X and 2X CO_2 levels.

The impact of increasing MR, which according to PLSR coefficients looks feebly connected to TCPI, has also been studied (but not shown here), using both,GFDL and HadCM3 dataset.

Scatter plots in figure (4.12), illustrate variation of TCPI Vs SST in the first panel, between TCPI Vs MR in the second panel, TCPI Vs SLP in the third panel, and TCPI Vs AT in the fourth panel of the figure (4.12). The figure displays the better relationship between $Vmax$ and SST as compared to other variables. The figure also supports significantly strong correlation obtained between TCPI and SST as shown in table (4.8)

As can be seen from the tables, (4.10)(4.9), ΔV reduces on increasing SLP and AT in all the ocean basins, except SIO where ΔV rather show slight increase.

Variables correlated	Correlation Coefficient (r)	Coefficient of Determination (r^2)
(TCPI, SST)	0.9746	0.96
(TCPI, SLP)	-0.7504	-0.56
(TCPI, MR)	-0.095	-0.009
(TCPI, AT)	-0.4940	0.24

TABLE 4.8: The table presents the Pearson's moment correlation coefficient (r) and the coefficient of determination (r^2) between TCPI and the four input variables (SST, SLP, MR, and AT, from reanalysis dataset). TCPI in the table above shows best connection with SST as compared with other three variables. This link can be visualised in the scatter plots between the same set of variables shown in the figure (4.12), which agrees with the values displayed in this table.

Tropical Ocean Basin (CMIP5 Dataset)	$\Delta V = V_{max_{AT+1}} - V_{max_{AT}}$ 1XCO_2	$\Delta V = V_{max_{AT+1}} - V_{max_{AT}}$ 2XCO_2
NIO	-4.64	-4.4
NWPC	-4.41	-4.3
NATL	-4.55	-4.4
NEPC	-5.29	-5.04
SIO	-5.17	-5.2
SWPC	-5.13	-5.12

TABLE 4.9: The table above illustrates the sensitivity of ΔV towards an increase in AT in tropics under present and doubled levels of CO_2. Where NIO refers to the North Indian Ocean, NWPC stands for Northwest PacifiC, NATL corresponds to North Atlantic Ocean, NEPC can be expanded as Northeast Pacific Ocean, SIO indicate South Indian Ocean, and SWPC represents Southwest Pacific Ocean

Tropical Ocean Basin (GFDL Dataset)	$\Delta V = V_{max_{AT+1}} - V_{max_{AT}}$ 1XCO_2	$\Delta V = V_{max_{AT+1}} - V_{max_{AT}}$ 2XCO_2
NIO	-0.27	-0.25
NWPC	-0.25	-0.24
NATL	-0.27	-0.26
NEPC	-0.29	-0.29
SIO	-0.23	-0.24
SWPC	-0.32	-0.32

TABLE 4.10: The table above illustrates the sensitivity of ΔV towards an increase in SLP in tropical ocean basins under present and doubled levels of CO_2. Where, NIO refers to the North Indian Ocean, NWPC stands for Northwest PacifiC, NATL corresponds to North Atlantic Ocean, NEPC can be expanded as Northeast Pacific Ocean, SIO indicate South Indian Ocean, and SWPC represents Southwest Pacific Ocean

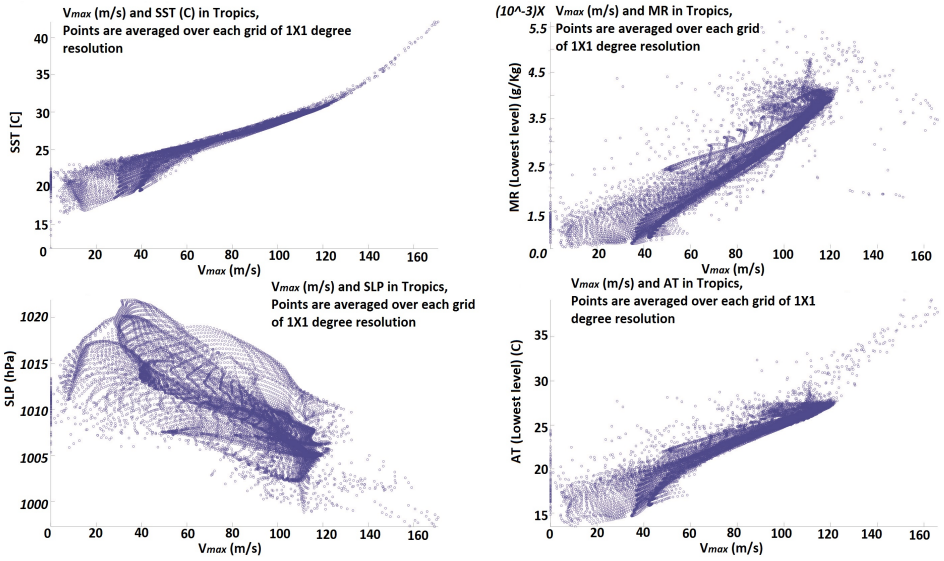

FIGURE 4.12: The figure illustrates scatter plots between TCPI and four input variables, SST, MR, SLP, and AT. The figure indicates a better connection between TCPI and SST (panel 1) as compared to other variables.

However, the response of ΔV to a unit increase in MR and SST shows rise in all the ocean basins, including SIO. However, change in SST gives rise to the maximum departures in the wind speeds both under present day and doubled CO_2 concentrations.

The results from sensitivity tests (table(4.12), table(4.10), table(4.9) table(4.11)) performed on each of the input (SST, SLP, and AT), shows that sensitivity of ΔV is highest towards SST and this sensitivity reduces in all the ocean basins when the CO_2 concentration is doubled.

4.3.4 Detailed Explanation of the Tables from Sensitivity Analysis section:

Interdependence between the TCPI and the four input variables, SST, SLP, MR and AT are individually quantified using Pearson's moment correlation coefficient and is shown in the table(4.8). The best connection can be seen with the ocean temperature (r = 0.98). The two datasets used here covers tropical ocean and the gridded data points are used to determine the correlation. The coefficient of determination between TCPI and SST is significant and substantial (r^2 = 0.96)

Model Ensemble (HadCM3 Dataset)	$\Delta V = V_{max_{SST+1}} - V_{max_{SST}}$ 1XCO_2	$\Delta V = V_{max_{SST+1}} - V_{max_{SST}}$ 2XCO_2
Q0	9.97	9.92
Q1	10.25	10.25
Q2	9.94	9.23
Q3	10.1	9.44
Q4	10.11	10.06
Q5	9.99	9.998
Q6	10.1	9.96
Q7	10.25	10.2

TABLE 4.11: Table above compares ΔV obtained from using perturbed model runs under present-day and doubled CO_2 amount. The ΔV values presented in this table are averaged over tropics. Individual oceans are also considered and are shown in other *e.g.* tables (4.12) which agree with the sensitivity saturation effect shown in the table above.

Tropical Ocean Basin (GFDL Dataset)	$\Delta V = V_{max_{SST+1}} - V_{max_{SST}}$ 1XCO_2	$\Delta V = V_{max_{SST+1}} - V_{max_{SST}}$ 2XCO_2
NIO	9.56	6.6
NWPC	9.44	6.7
NATL	10.77	6.97
NEPC	10.04	6.94
SIO	9.44	6.4
SWPC	8.41	5.9

TABLE 4.12: CMIP5 Dataset: Table above illustrates the sensitivity of ΔV towards an increase in SST in tropical ocean basins under present and doubled levels of CO_2. Where, NIO refers to the North Indian Ocean, NWPC stands for Northwest PacifiC, NATL corresponds to North Atlantic Ocean, NEPC can be expanded as Northeast Pacific Ocean, SIO indicate South Indian Ocean, and SWPC represents Southwest Pacific Ocen

(table(4.8)). This high correlation seen here motivates us to look for the sensitivity of TCPI towards SST.

The sensitivity of change in TCPI towards an increase in AT at present day and doubled CO_2 levels can be seen in the table (4.9) (HadCM3) and table(4.10) (GFDL). An increase in AT by a unit degree in present day and doubled CO2 state shows interesting patterns in all the ocean basins. The change in TCPI with 1 degree Celsius increase in the atmospheric temperature is negative in all the ocean basins and under the present day and doubled CO2 conditions. This indicates the damping effect of the high AT above the ocean surface. This damping

effect could be explained by the decrease in the evaporation rate with the increased temperature above an ocean basin. Interestingly, through the damping is apparent in all the ocean basis, it reduces on increasing CO_2 concentration, which increased the ocean temperature underneath, thereby leading to correspondingly higher evaporation rate and atmospheric instability, promoting higher TCPI.

Table (4.6 and 4.12) illustrates how sensitive is the TCPI towards a unit increase in the SST in the tropical ocean basins (NIO, NWPC, NATL, NEPC, SIO and SWPC) under present and doubled CO_2 scenario. Table (4.6) uses the HadCM3 data for the analysis while HadCM3 data for the analysis while the table (4.12) uses data from GFDL. The sensitivity of the change in TCPI towards ocean temperature is highest in the North Atlantic when GFDL is used table (4.12) but not so when HadCM3 is used table (4.6). Interestingly, the tables indicate different levels of sensitivity towards the ocean temperature under the present day and doubled CO_2 scenarios. Ocean temperature as derived from HadCM3 leads to comparatively higher values.

Tables(4.7 and 4.6) show that the ΔV values as obtained from HadCM3 (4.6) are comparatively higher than those from GFDL (4.7). A possible explanation of the observation comes from differences in the response of the two models towards increasing CO_2 concentration. On comparing SST values as obtained from GFDL and HadCM3, it was found that the HadCM3 SST values are higher and doubling of CO_2 amount in the HadCM3 gives comparatively higher rise in SST than those obtained from GFDL and thus the V_{max} values correspondingly the ΔV values. This indicate that HadCM3 responds with higher SST gradient and is thus more sensitive to the doubling of CO_2 concentration than that of GFDL.

4.4 Conclusions

The study has identified the sensitivity of ΔV to a unit increase in SST. The sensitivity however decreases on increasing CO_2 concentration in a climate system.

The mechanism could be understood as follows. Increased CO_2 concentration increases atmospheric temperature substantially which suppresses the evaporation and thus the amount of latent heat liberated. This reduction in the heat liberation in turn reduce the amount of the input energy for a TC. This can also be

understood in terms of decreased atmospheric instability due to increase in the atmospheric temperature above.

One of the most important findings to emerge from this work is that the "sensitivity" of tropical cyclone strength to ocean warming could eventually saturate with the rise in CO_2 concentration. All the considered ocean basins show a significant increase in the tropical cyclone intensity as response to 1 °C increase in the ocean temperature. Tropical cyclone intensity in the different ocean basins responds differently to the varied CO_2 levels and to the changed SST values.

The research has also shown that each ocean is unique in terms of its sensitivity towards cyclone intensification as a result of increasing SST. SST, atmospheric temperature, and ocean-atmospheric temperature contrast (SAT) are the factors that have pronounced impact on cyclone intensification. The most obvious finding to emerge from this study is that influence of atmospheric mixing ratio is small on tropical cyclone intensification. Increasing SLP and atmospheric temperature have negative effect on tropical cyclone intensification.

From this research, another important questions arises. Considering that the decrease in the "sensitivity" of ΔV towards SST goes on, with increasing CO_2 amount, then is it expected that the sensitivity would saturate, and wouldn't change further? If it does saturate, at what critical value of CO_2 would this occur?

Is this situation any similar to the band saturation effect and does it too follow the logarithmic relationship between the CO_2 concentration and ΔV?

4.5 Weakness and Limitations

This work is one of its kind to find saturation in "sensitivity" of tropical cyclone strength towards SST as a result of increasing CO_2. However, this work only looked at doubled CO_2 scenarios and did not attempt to study cases with a further increase in CO_2 concentrations. Thus, extensive experimentation with different levels of CO_2 is suggested to avoid any circumstantial findings.

Secondly, datasets from only two models (HadCM3 and GFDL) are used here which differs from each other. Thus, we suggest considering data from more models to increase confidence in the results.

Moreover, Emanuel's methodology used here to compute TCPI is only an approximation.

Finally, the data from GFDL and HadCM3 models used here may have errors.

Chapter 5

Summary, Conclusions and Recommendations

5.1 Introduction

This chapter presents the summary of the research work undertaken, the conclusions drawn and the recommendations made as an outgrowth of this work.

This study investigated the impact of our changing climate on the TC intensity. This research has sought to understand the spatial and temporal behaviour of the TC intensity under present day and changed climatic scenario. The scientific literature is inconclusive on several vital questions within the diversified discourse. One of question reflects on the impact of the varying CO_2 concentration on TC's tendency to intensify.

The study also attempts to understand the TC intensity's sensitivity towards the basic underlying parameters like ocean temperature, atmospheric temperature, humidity content and the sea level pressure. This part of the study leads us to an unanticipated finding which has never been documented before which we term as the possible sensitivity saturation effect analogous to the well-known "Band Saturation effect". This part of the work would be of high interest to climatologists and could have an impact on our present understanding of the intensifying storms in the warming world, forced by the available literature till date.

There are two sections corresponding to the two main questions investigated in the thesis.

The first section of the research presents the one to one connection and importance of the ocean temperature on the TC potential intensity. Making use of this interesting finding, we attempted to develop a simple statistical model to express the spatial distribution of the TC potential intensity. The statistics of TC strength on doubling CO_2 concentration was looked at using this model.

The second part of the research sets out to quantitatively understand how does the dependence of TC strength on the ocean temperature changes on changing the CO_2 concentration.

We summarise and discuss results of each of these two sections next followed by the conclusions, limitations of the work along with the recommendations for further investigation and experimentation to explore the questions the work has posed or to undertake the limitations of the work (be it in terms of data availability or otherwise).

What this research doesn't do is to develop a new thermodynamic TC potential intensity model or theoretically modify one. Nor does it improve the existing ones but make use of a well-established theoretical model to study TC potential intensity under different climatic conditions.

5.2 The Questions

The main objective of this dissertation has been to investigate the response of TC potential intensity to the warming world. This question was motivated by a need to apprehend behaviour of the TC potential intensity in general and its dependence (both spatial) on the natural variations and the desire to anticipate its future as a response to our warming world.

The pathway to answer the primary questions generated a number of secondary questions which were also investigated. A few of which are as follows.

1. What is the role of sea surface temperature in tropical cyclone intensification. How can we use this connection to estimate TC potential intensity?
2. How can the warming oceans influence TC potential intensity?
3. What is the impact of $2XCO_2$ on TC potential intensity?

4. How sensitive is the TC potential intensity to the underlying factors?

5. How important is the role of ocean warming in the TC intensification on spatial scales?

5.3 The Answers

I have proposed answers to these questions, based on a detailed analysis of the observations, theoretical and numerical models, advanced statistical methods capable of handling non-linear and non-stationary data.

1. **Chapter 3**

   Spatially and temporally, the TC potential intensity shows the highest response towards the ocean temperature and towards atmospheric temperature to some extent.

   Using three reanalysis datasets, we found that over the TC prone region, SST in general and ocean-atmospheric temperature contrast, in particular, contributes to the maximum TC potential intensity. This finding could be understood in terms of the enthalpy exchange process between the ocean surface and the atmospheric profile over it, in view of the TC's secondary circulation behaving as a natural Carnot heat engine. A higher ocean temperature acting as a strong TC source may directly affect the TC potential intensity by increasing it. Based on this view, a simple linear model was developed. Considering significantly high correlation coefficients between the developed model and the theoretical model, we were enabled to compute the TC potential intensity mainly by employing the SST values with somewhat sub-optimal but acceptable performance during the situation when other datasets (SLP, AT and atmospheric humidity profiles) are not available. Outputs of the model in the various ocean basins closely coincide with the evolved model (to the first degree of approximation) and the observations (ACE index) to a fair extent. The TC potential intensity seems to vary inhomogeneously throughout the tropics i.e. it varies by a different amount in the different ocean basin.

The simulated model shows that the amount of variation in the TC potential intensity in the North Atlantic and the Northeast Pacific Ocean is comparatively less than that in the North Indian Ocean and the Northwest Pacific when CO_2 concentration is doubled.

The spatial spread of the simulated TC potential intensity, show patterns similar to the ENSO's warm pool and cold tongue patterns which are an indicative of a possible connection between ENSO and the TC potential intensity. (Shown over the temporal scales in the chapter not included in the thesis)

The Northern Hemisphere shows more warming and more associated TC potential intensity in the warming world. The surface wind speeds show high anti-correlation with the minimum pressure values over the tropics. This anti-correlation has been observed in all the ocean basins to an appreciable extent (supplementary figs).

In a prediction using a climate model, both tropical ocean temperature and the TC potential intensity shows an inhomogeneous increase. The calculated difference between the TC potential intensity under the present-day and doubled CO_2 cases show a dramatic rise in the TC potential intensity in the North Indian Ocean, the Northwest Pacific, and the North Atlantic Ocean. The TC potential intensity illustrates a strong dependence on the underlying ocean temperature spatially and thus would be considered as one of the primary drivers of the TC intensification tropically.

Chapter 4

The chapter examines the TCPI's sensitivity to the ocean temperature. Two independent models reveal an average increase in the TC potential intensity between 8 to 10 m/s per unit increase in the ocean temperature (in ^oC). The key finding to emerge from this study is that the increase in the TC potential intensity responds comparatively weakly to the ocean temperature on increasing CO_2 amount.

On doubling the CO_2 concentration change in the TC potential intensity shows a weakened response to the increased SST values. This effect is observed in all the ocean basins considered in the study. Though the TC potential intensity shows an overall rise on increasing the CO_2 concentration but, its response to the SST decreases. We termed this observed behaviour as the sensitivity saturation effect which we define as the reduction in the

TCPI's sensitivity towards the change in the SST on increasing CO_2 concentration. This observation leads to a next level question of whether there will be a sensitivity saturation effect, analogous to the well-known "Band Saturation effect", as a response to the increasing CO_2 levels and if it does, at what cut-off CO_2 levels. This emerging question opens up a new area of investigation for the climatologists.

In this way, this research provides a framework for the future exploration of the subject. The study also depicts unique characteristics of the ocean sensitivity towards the local ocean temperature variations. Increasing SLP and AT show an overall negative impact on the TC potential intensity.

5.4 Limitations & Prospective Suggestions

Chapter 3: Handicapped by the HadCM3's performance around the land areas in the ocean, the future projections of the TC potential intensity near the areas surrounding the land is doubtful for the same reason. A more reliable model is suggested to take the analysis to next level.

This study used WISHE model approach which is debated in some documented researches. So, we suggest a next level investigation by employing a model closer to the non-axi symmetric spin-up state of an ideal TC.

The simple statistical model developed here is based on the SST alone and thus offers an opportunity to study the TCs over the remote places where other parameters are unavailable. But, at the same time, errors in the SST will be propagated to the estimated TC potential intensity as there is no mechanism to prevent the error from propagating into such an overly simplistic approach. A highly reliable SST data set with the removed bias could assist in overcoming this shortcoming to some extent.

Chapter 4: The fifth chapter looked at the present and doubled CO_2 scenarios only with the two well-established climate models, both of which supports our findings. It would be worth experimenting with the different levels of CO_2 and test for the sensitivity saturation effect.

We also suggest an in-depth study to explain the observed response of TC strength towards an increase in SST under the considered CO_2 concentrations from the point of view of the thermodynamics of TC intensification.

5.5 Contributions

1. **Chapter 3:** The study offers several significant contributions. The primary contribution of this study has been to substantiate the vital role of the ocean temperature on the TC potential intensity. The study demonstrates one to one connection between the SST and TC potential intensity on the spatial scales (1X1 degree grid). This not only contributes to the existing knowledge of such a connection but also take this knowledge further and apply it to compute the TC potential intensity using a simple regression equation using SST alone. This promotes our understanding of how the TC potential intensity would vary at remote locations where, SLP, MR, and AT profiles are unavailable.

   In view of the satisfactory performance of the TC potential intensity model developed here (VmaxNw) and its good correlation with the ACE in all the considered ocean basins, VmaxNw can be used in place of the ACE index to some extent.

   Thus, this work offers several practical applications.

   This study confirms the findings of (Saunders [1997],Miller [1958], Palmen [1948b]) which found a strong connection between the TC potential intensity and the local ocean temperature.

   Another important contribution of this study is that it gives confidence to the previously existing theory which found an increase in the TC potential intensity in the warming world (Walsh et al. [2015]).

2. **Chapter 4:** This study has several important contributions.

   Firstly, it confirms the findings of (Strazzo et al. [2015]) which indicated towards the spatial sensitivity of the TC potential intensity on the local SST. Secondly, this is the first time that the reduction in the TCPI's sensitivity towards the ocean temperature has been reported under the climate change

(doubled CO_2) scenario. This characteristic of the TC potential intensity has been confirmed using two well-established climate models.

Most importantly, this study invokes an idea of the "Sensitivity Saturation Effect" (a term coined by the author) according to which we propose that the response of the TC potential intensity to the ocean temperature could saturate on increasing CO_2 concentration.

Appendix A

Supplimentary Figures, Tables and Explanations

A.1 Chapter 3

A.1.1 Dependence of V_{max} on SST and AT

The Storm strength is quantified as the maximum wind speed in the storm. This speed is considered at 10 metre height for an average of one to ten minutes. V_{max} is primarily determined by considering the TC as a Carnot heat engine, mainly it's secondary circulation. A TC has two circulations primary and secondary. The primary circulation includes the rotational part of the flow and is purely circular in nature. This is the circulation element which is responsible for the majority of the damage associated with the TCs. The secondary part of the circulation involves the overturning (in-up-out-down).This part of the circulation flow is slower than the primary part but governs the energetics of the storm Emanuel [2006]. The flow is in the radial and vertical directions. The primary energy source for this type of cycle is the evaporation of water from the sea surface. The sea surface act as both, the source (evaporation) and as a sink (friction) of TC's energy. This leads to the theoretical upper limit on the attainable storm's wind speed Emanuel [2006]. This upper bound is called, the Maximum potential intensity (V_{max}). V_{max} depends on the Convective Available Potential Energy (CAPE) of the evaporated and lifted air parcel and the energy of the environmental boundary layer air parcel. CAPE is the measure of the atmospheric instability which is associated with the severe

weather systems, for instance, TCs. Put simply, CAPE represents the energy a parcel of air would attain if raised to a vertical atmospheric level. The link between the V_{max} and CAPE is as followsBister and Emanuel [2002]:

$$V_{max} = \sqrt{\left(\frac{T_s}{T_0}\right)\frac{C_k}{C_D}\left(CAPE_S - CAPE_b\right)} \tag{A.1}$$

In the equation, A.1, $CAPE_S$, represents the CAPE of an air parcel lifted from saturation at the sea level. $CAPE_b$ is the CAPE at the boundary layer air, at the radius of maximum winds. CAPE is given as follows:

$$CAPE = \int_{LFC}^{LND} g\frac{\Theta(z) - \overline{\Theta(z)}}{\overline{\Theta(z)}}dz \tag{A.2}$$

where, Θ represents the virtual temperature which entertains the use of the dry-air equation of state for the moist air except that T is replaced by Θ. Now, $\Theta \sim (1 + 0.61r_v)T$ where, r_v represents the mixing ratio. On taking ratio of the two virtual temperatures, at a particular level, this factor, $(1 + 0.61r_v)$, vanishes and we are left with the temperature term only.

Determining $CAPE_S^*$ and $CAPE_B$ using the definition of CAPE and equation(A.2). Assuming the adiabatic moist lapse rate to be, γ_m, where, $\gamma_m = dT/dz$. For a parcel lifted from the sea surface to an environmental sounding say at (e.g.P_s = 650mb), the associated CAPE would be,

$$CAPE_s^* = \left(\frac{(T_{p,ps} - T_{e,ps})}{T_{e,ps}}\right)gdz \tag{A.3}$$

$$CAPE_b^* = \left(\frac{(T_{b,pb} - T_{e,pb})}{T_{e,pb}}\right)gdz \tag{A.4}$$

Given the lapse rate, $\gamma' = dT/dz$, $T_{p,ps} = (SST - \gamma' dz_s)$ (for the negative lapse rate, typical of tropics) and $T_{e,ps} \approx AT(z_s)$. In the boundary layer region then, $T_{e,pb} = AT(z_b)$ while, $T_{b,pb} = (SST - \gamma' dz_b)$. Substituting these expressions in equation, A.3 and A.4, and taking difference of the two CAPES,$(CAPE_s - CAPE_b^*)$,we get,

$$CAPE_s - CAPE_b^* = \Big(\frac{(SST - \gamma' dz_s) - AT(z_s))}{AT(z_s)} dz_s - \frac{(SST - \gamma' dz_b) - AT(z_b))}{AT(z_b)} dz_b\Big) g \tag{A.5}$$

From A.5, we can infer that the difference of the convective potential energy at the boundary layer and that in the atmosphere, rising from a saturated state depends on the atmospheric temperature at the level and at the sea surface temperature level from which the parcel rose at the first place. *i.e.*

$$CAPE_s - CAPE_b^* = f(AT(z), SST) \tag{A.6}$$

Now, V_{max} is a function of $CAPE_s - CAPE_b^*$ (Equation(A.1)) which in turn depend upon the SST and AT thence the V_{max}.

$$V_{max}^2 \propto CAPE_s - CAPE_b^* = f(AT(z), SST) \tag{A.7}$$

This (Equation A.7) is in line with our results which represents the dependence of V_{max} on the SST and the atmospheric temperature. A Positive CAPE is essential for convection and thence storm formation. For this to be true,(From Equation A.5), SST should be high while AT should be relatively low to cause positive buoyancy and hence the positive CAPE.

A.1.2 Computing V_{maxNw} using SST

As stated in section(3.3.1), the TCPI, V_{maxNw}, was computed using SST, which was chosen as a result of a strong correlation of the TCPI with the $\triangle T$, where, $\triangle T$ = f(SST, AT_1).

Computation of $\triangle T$ involved a couple of sensitivity experiments before deciding the optimal method. SST is the dominant factor to approximate the TCPI to a good extent, in most cases.

During the initial experimentation, $\triangle T$ was taken as (SST - mean(AT)), where mean(AT) was the statistical mean of the atmospheric temperature in a column. $\triangle T$ values over all the considered ocean basins were very high owing to the negative mean(AT) values. But, we know that mean of AT computed without taking the varying density into account is impractical.

It can be found in the literature (Bevis et al. [1992]) that the mean(AT) values can be approximated using SST. Thus, SAT was calculated as the difference between SST and mean(AT), where AT can be defined in terms of SST using an equation. The coefficients, however, vary from one region to another. If our atmosphere were isothermal, then the mean temperature would be constant, equal to the surface temperature. However, the atmospheric temperature shows a negative gradient up to the tropopause, the mean column temperature would be given by the temperature of the atmosphere weighted by the pressure of the water vapour. Thence, mean(AT) would depend on the surface temperature (SST in our case). Dependency of the mean atmospheric temperature on the surface (at surface temperature, T_s) would then be, mean(AT)= $55.8 + 0.77T_s$ over the New York area (Davis et al. [1985]). For more details on the equation, please refer to, (Bevis et al. [1992]),(Davis et al. [1985]).

Finally,the lowest atmospheric temperature was used to compute SAT (=SST - AT1) and again a good correlation with the TCPI was found. So, it was decided to use this method which finally lead us to the relationship, VmaxNw = f(SST), (Eq. 3.5).

A.1.3 Application of Linear Model Outputs to HadCM3 Model

We examined changes in SST and hence V_{maxNw} and PDI projected from the third version of the Hadley Centre Climate Model, HadCM3, where coupled oceanic-atmospheric model outputs were considered in the present day and for a doubled CO_2 scenario. We further applied the resulting ensemble outputs generated by perturbed physics outcomes from the HadCM3 climate model to our statistical model of determining TC winds. This was done to investigate the change in maximum sustained winds and hence cyclone strength when CO_2 levels are doubled in our atmosphere.

It should be noted that the climate model outputs used here are inefficient at resolving the details of tropical cyclone intensity. Both reanalysis and model projections of cyclone wind speeds are found to be highly correlated to SAT, which is, in turn, are strongly linked to SST. Modeled V_{maxNw} derived from SST again show a high correlation between the reanalysis and HadCM3 model outputs for the

present day CO_2 level. Using estimated values of SST from the climate model outputs employing both present day and doubled CO_2 cases in our statistical model (Equation(3.5)), we computed V_{maxNw} for the two cases mentioned before. The difference in the wind speeds obtained with enhanced CO_2 levels show a significant increase in maximum sustained winds as shown in Figure(A.1), and hence cyclone strength. This can be interpreted as stronger storms in the warming world with higher levels of CO_2. The increase in maximum sustained wind speeds is heterogeneous in both hemispheres with the higher increase in the Northern Hemisphere. The Northeast Pacific shows the highest rise in storm winds Collins et al. [2010]. The North Atlantic Ocean comes next in the list of regions. The Indian Ocean followed by the West Pacific region show little influence due to increased levels of CO_2. This trend is reversed in the Southern Hemisphere with the West Pacific and the Indian Oceans representing regions most prone to destruction by TCs while the South Atlantic and the South East Pacific Ocean basins show the smallest increase in storm wind speeds. To summarise, it is some sort of dipole effect, with regions in the North showing highest increase reflecting the lowest increase in the South.

In a futuristic scenario of doubled CO2, both SST and V_{max} increases. The oceans more prone to such intensification are the North Indian and the West Pacific basins, and (f) Tropical cyclone intensity is highly dependent on ocean temperature. SST can be considered as one of the main driving forces for tropical cyclone intensification. Hence, when other parameters are unavailable, we can use SST to simulate tropical cyclone intensity to a reasonable extent for global tropical oceans as has also been demonstrated by previous case studies [cf. Montgomery et al. [2009]].

Using Eq.(3.5) we temporally determine proxy index for V_{max}, V_{maxNw}, and then computed the same parameter from temporal reanalysis outputs. The linear link between the two-time series comes out to be only 0.86 in the tropical Atlantic Ocean and is about 0.74 in tropical parts of West Pacific Ocean. Thus, we can not efficiently employ spatially derived V_{max} model to determine the parameter varying temporally. This could be accounted to the non-stationary behaviour of maximum sustained winds. However, as we showed earlier, the spatially derived proxy index (V_{max}), averaged over time, successfully determine maximum sustained wind speeds in tropics and the cyclone prone ocean basins.

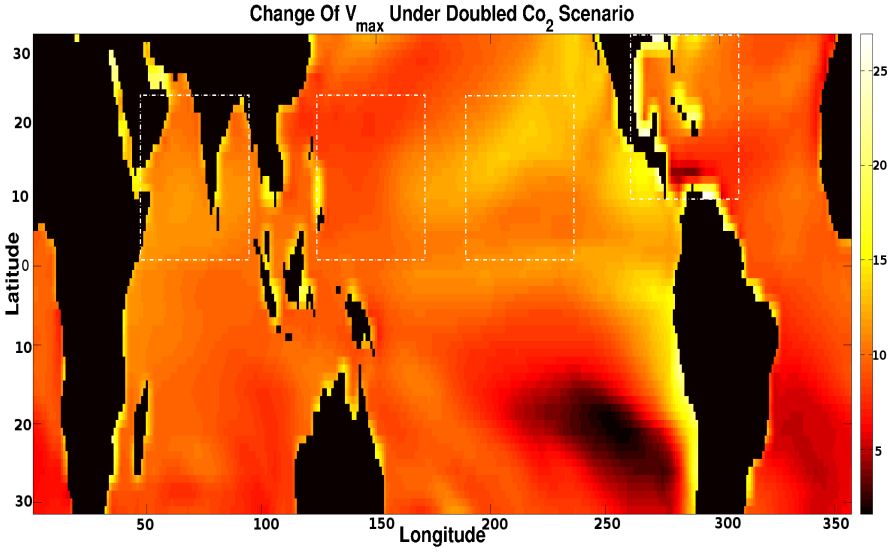

FIGURE A.1: Change in tropical cyclone wind speeds, V_{max}, on doubling CO_2 scenario

Observed imbalance in theoretically maximum sustained wind speeds, V_{max} and V_{maxNw}, can be the narrated by a comparable spreading of SST and mean atmospheric temperature, SAT. Also, higher V_{max} in the West Pacific and the Indian Ocean are similar to SAT_{max} distribution.

It should be noted that TCs rarely occur within 5° North and South of equator due to negligibly small value of planetary angular momentum (Henderson [1998]). However, TC wind speed, V_{max}, as derived using ref(Bister and Emanuel [1998],Bister and Emanuel [2002]) (Figure(A.8)) does show high values due to absence of this concept in the model.

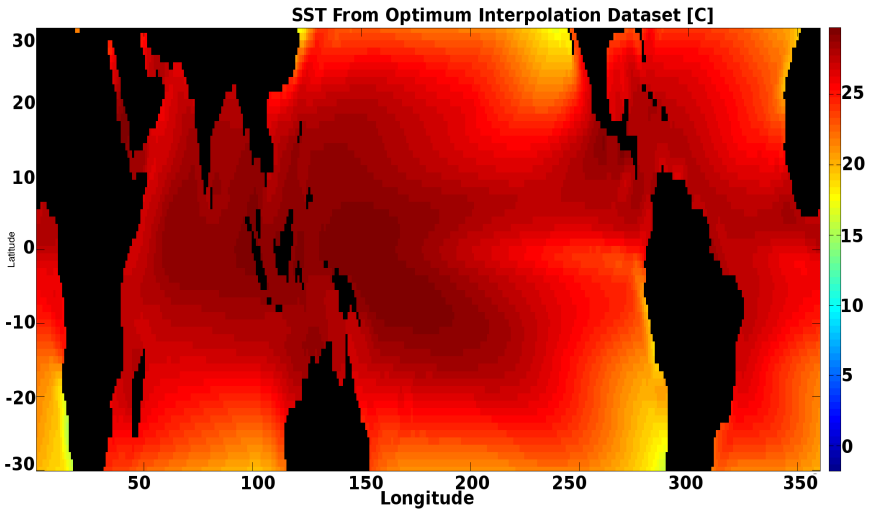

FIGURE A.2: Tropical spread of SST, from $SST - OI$ dataset(NOAA [2014])

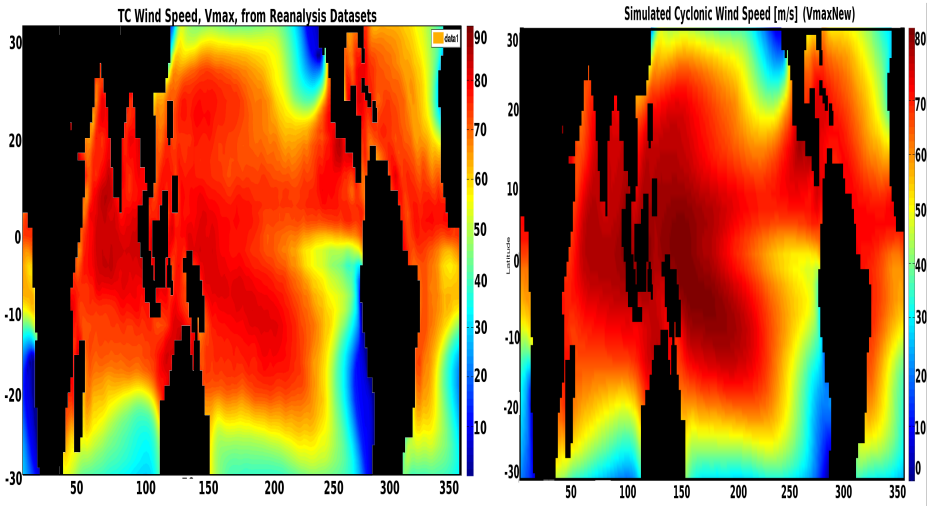

FIGURE A.3: Comparison of the Cyclone wind speed, V_{max} and V_{maxNew} as, obtained from reanalysis datasets; ERSST-V3b (SST), SLP, Specic Humidity & Atmospheric temperature profile. The Modeled tropical cyclone wind speed, VmaxNew, w.r.t. ERSST-V3b (SST), as input to Eq(3.5). Peak wind speed distribution as derived from an algorithm based on thermodynamics and that obtained from our simple linear model match well in tropics.

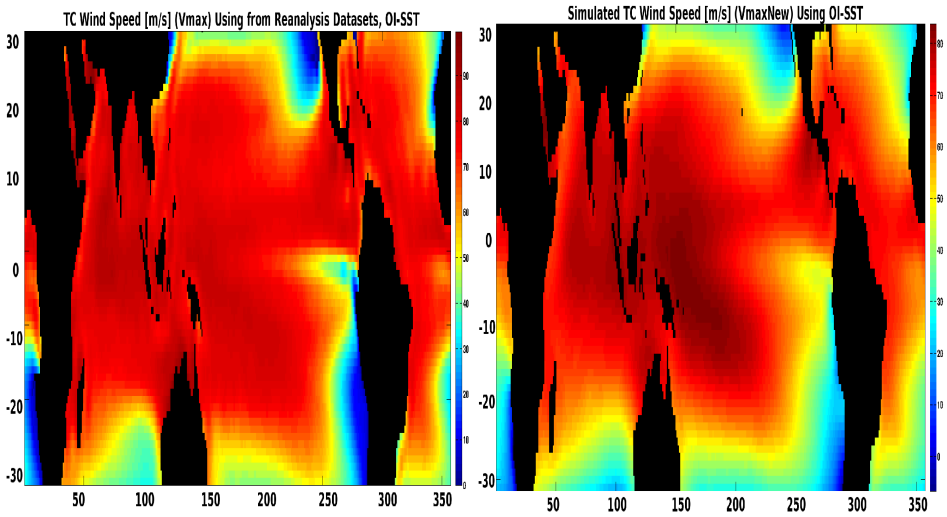

FIGURE A.4: Cyclone wind speed, V_{max}, obtained from reanalysis datasets; OI.SST (SST) (NOAA [2014]), SLP, Specific Humidity & Atmospheric temperature profile. Modeled cyclone wind speed, V_{maxNew}, as obtained from OI.SST (SST) dataset(NOAA [2014])

Also, due to errors in SST obtained from HadCM3, Figure(A.7) close to land regions, we notice remarkable hype in $VmaxNw$ close to land areas during doubled CO_2 case (refer to figure(A.1)). The observed results in those troubled regions are however not supported in this work due to issue with the data quality Connolley [June, 2005].

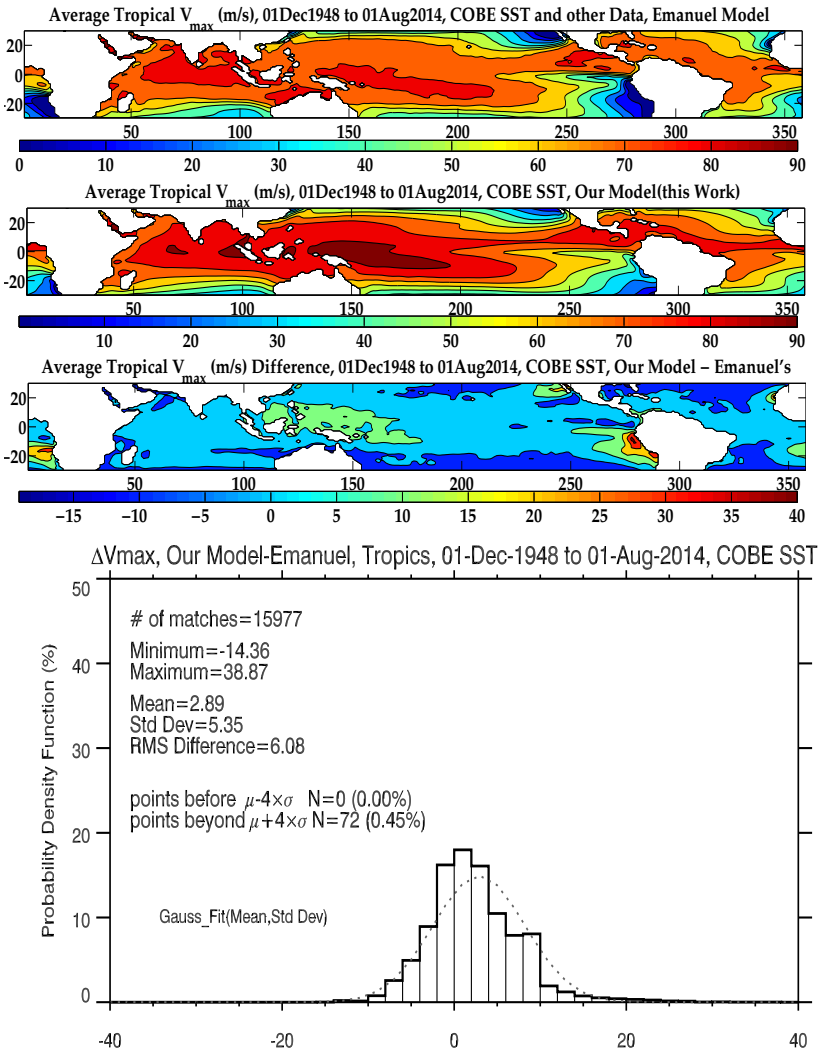

FIGURE A.5: Comparison of cyclone wind speed V_{max} obtained from Emanuel's model and our simplistic empirical approach with only SST as input. Row-1: V_{max} employing Emanuel's model with reanalysis datasets as inputs: SLP, specific humidity and atmospheric temperature profile and COBE SST; Row-2: V_{maxNew} employing our approach (Equation 3) with COBE SST; Row-3: Spatial distribution of V_{maxNew} minus V_{max} to visually identify areas of disagreement, considering V_{max} as a benchmark (reference), Row-4: Probability density function (PDF) of 'δ V_{max} = V_{maxNew} - V_{max}'. Statistical parameters (number of Vmax matches, minimum, maximum, mean, standard deviation, root mean square difference), a Gaussian fit, X N(mean, Std Dev) and number of grids beyond " Mean ± 4*Std Deviation", henceforth called 'extreme grids', are also annotated on the PDF.

A.1.4 Understanding the role of Sustained Wind Speed through Enthalpy

This result showing an indirect association between SST and sustained wind speed can be explained by considering the contribution of enthalpy exchange between

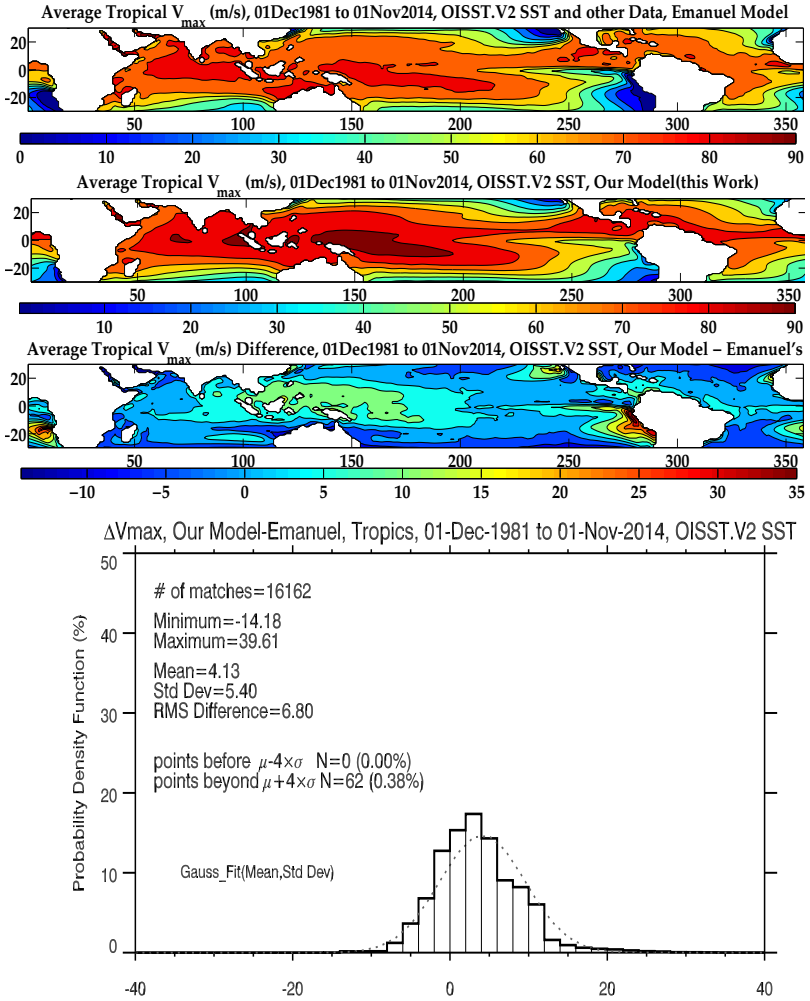

FIGURE A.6: Comparison of cyclone wind speed V_{max} obtained from Emanuel's model and our simplistic empirical approach with only SST as input. Row-1: V_{max} employing Emanuel's model with reanalysis datasets as inputs: SLP, specific humidity and atmospheric temperature profile and OISST.V2 (SST); Row-2: V_{maxNew} employing our approach (Equation 3) with OISST.V2 (SST); Row-3: Spatial distribution of V_{maxNew} minus V_{max} to visually identify areas of disagreement, considering V_{max} as a benchmark (reference), Row-4: Probability density function (PDF) of 'δ V_{max} = V_{maxNew} - V_{max}'. Statistical parameters (number of Vmax matches, minimum, maximum, mean, standard deviation, root mean square difference), a Gaussian fit, X N(mean, Std Dev) and number of grids beyond " Mean ± 4xStd Deviation", henceforth called 'extreme grids', are also annotated on the PDF.

the ocean and the air above during cyclone genesis. A tropical cyclone draws heat energy from the warm ocean water and uses it to evolve and move across the underlying surface against friction. Thus, a TC system can be regarded as a heat engine. At equilibrium, the input energy is equal to the energy going out of the system or is used in mechanical motion against the surface friction. Considering a cyclone system to be an ideal thermodynamic heat engine, the Carnot engine,

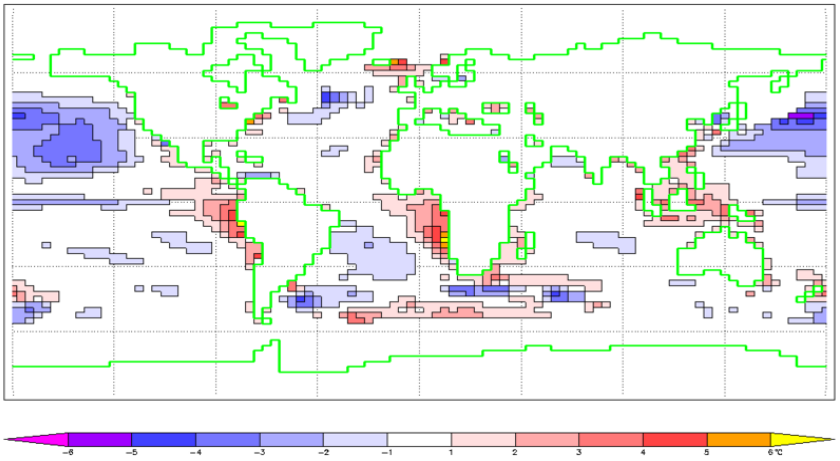

FIGURE A.7: SST errors in HadCM3 as when compared with ERA-15 (annual mean), Courtsey: Connolley [June, 2005]

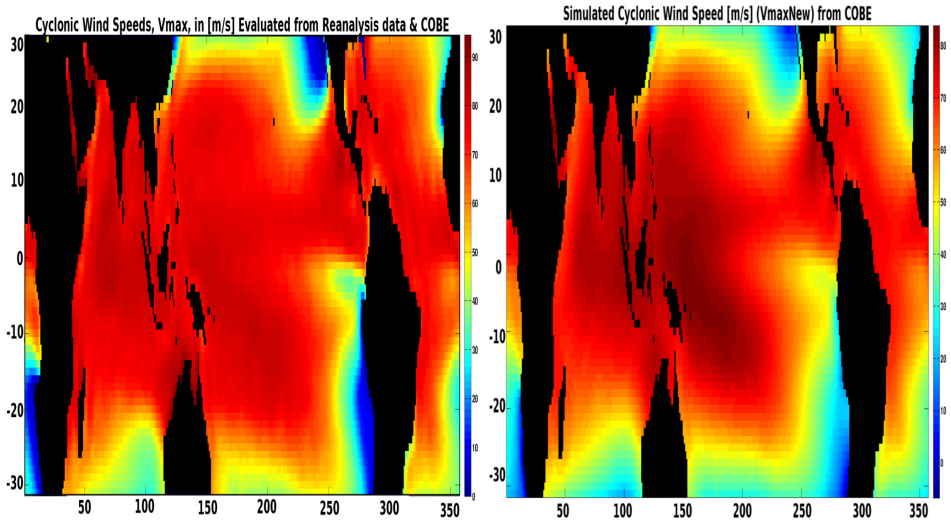

FIGURE A.8: Cyclone wind speed, V_{max}, obtained from reanalysis datasets; COBE (SST), SLP, Specific Humidity & Atmospheric temperature profile (COBE-NOAA [2015]) and the Modeled tropical cyclone wind speed, V_{maxNew}, w.r.t. COBE (SST) (COBE-NOAA [2015]), as input to Eq.(3.5). Peak wind speed distribution as derived from algorithm based on thermodynamics and that obtained from our simple linear model matches well.

at equilibrium cf.Emanuel [1986],

$$W_{in} = W_{out} \tag{A.8}$$

The Energy per unit area going out of the system due to frictional dissipation, associated to surface drag coefficient (C_d) and rotational wind speed ($\mathbf{u}$), produces losses given by,

$$\boldsymbol{W_{out} = C_d \rho u^3} \tag{A.9}$$

Where, ρ denotes the density of near surface air in kg/m^3. Owing to friction, energy loss per unit area, per unit time, *Energy* dissipated is given as,

$$W_{out} = C_d \rho v^3 \tag{A.10}$$

where, the density of air near the surface is in Kg/m^3, wind speeds close to the ground, v, in m/s. Assuming that behaviour of cyclogenesis is similar to that of a heat engine with efficiency, ε, and total heat input per unit time and surface area, Q_{in}. The energy produced in the system per unit surface area is given by,

$$W_{in} = \varepsilon Q_{in} \tag{A.11}$$

Also, the assumption of cyclone formation being similar to that of a Carnot heat engine efficiency Emanuel [1986] as a function of SST and the outflow temperature, is given by,

$$\varepsilon = \frac{T_s - T_0}{T_s} \tag{A.12}$$

Specific enthalpy (k), enthalpy (energy) per unit mass, which is combination of sensible heat $(C_p * T)$ and the associated latent heat, $(L_v * q)$,is given by,

$$k = C_p T + L_v q \tag{A.13}$$

here, water vapour concentration is q, L_v denotes the latent heat of vapourization, T as the air temperature above and, C_p as the heat capacity of air. Two sources of heat input into the storm system are, evaporation from the sea surface and secondly the recycled heat from frictional dissipation, where former is the dominant source of heat input into the cyclone system during its formation. Evaporation rate, rate of heat input into the system from the ocean can be given by using bulk aerodynamic formula (M. T. and Emanuel [2012]),

$$Q_{in,ss} = C_k * \rho * v * \Delta k \tag{A.14}$$

where, Δk is the difference of enthalpy from the sea surface and the air above it and C_k represents enthalpy exchange coefficient. Thus, higher contrast between the two will increase the evaporation rate sourcing tropical cyclone. This goes well with our results stated above.

Another source fueling a cyclone is the internal sensible heat activated by the frictional dissipation which is equal to the dissipated heat, W_{out}. It appears within a TC system and recycles back into the spinning system. Thus, it can be equated to W_{out} as follows:

$$Q_{in,diss} = C_d \rho v^3 \tag{A.15}$$

Making used of these relations, rate of total energy generated per unit surface area is then given by,

$$W_{in} = \varepsilon Q_{in} = \frac{T_s - T_0}{T_s}(C_k \rho v \Delta k + C_d \rho v^3) \tag{A.16}$$

Where, T_s and T_0 refers to temperature at surface of ocean and the atmosphere above it, respectively.

The Equation(A.16) provides a good thermodynamic approximation of the behaviour of SST and Atmospheric Temperature profile during TC genesis in relation to changes in enthalpy (Δk), though deriving this equation involves various assumptions and hence has its own limitations.

A.1.5 Potential of SST Alone in Describing TC Potential Energy

To test this, we ran two controlled experiments. In the first one, only SST varied while keeping AT, MR and SLP constant. In the second one, both SST and AT varied while keeping the other two variables constant (MR, SLP = Const.). Both of these experiments were run for 1X and 2X CO2 scenarios. The first experiment with varying SST and AT is shown in Fig 1a and Fig 2a below. The case while changing SST alone is shown in Fig 1b and Fig 2b. As can be seen from the figures, PI between 7 to 25 N and S latitudes, discarding the regions between 7 degrees N and S of the equator where Coriolis force is negligible, the spatial distribution in both the cases is not very different. The PI for the case when AT

is also considered shows little spread towards higher latitudes than for the case when SST alone is considered. Considering AT into the picture suppresses the PI, mainly in the northern hemisphere, from flourishing towards higher latitudes. Thus, VmaxNew for the 2XCO2 scenario, derived using SST alone, gives a good first approximation in most of the tropics.

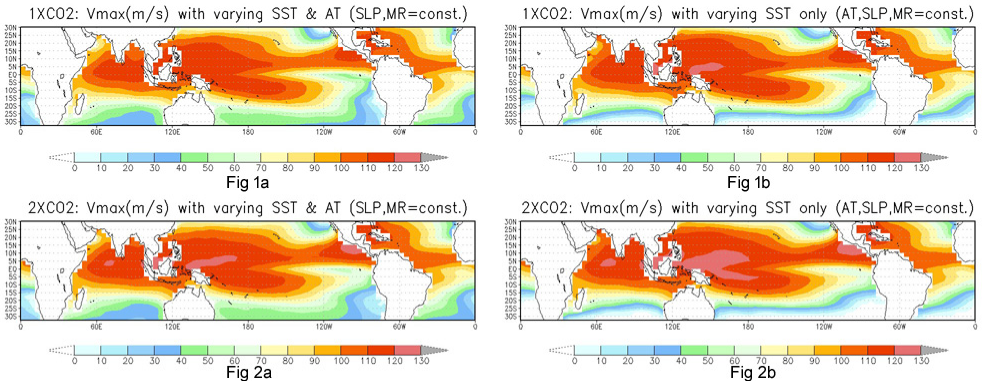

FIGURE A.9: Control experiment with changing only SST values and keeping other variables constant (Fig 1b, Fig 2b) and the case when both, SST and AT varies while keeping rest of the input variables unchanged (Figure (A.9(a)), Figure (A.9) 2a) for both, 1X, 2XCO_2 scenarios

A.2 Model application on temporal resolution

In order to analyze if this simplistic approach holds adequately in the temporal domain, a time series analysis is performed using wavelet spectrum and standard time series plots. The conclusion that is drawn on a spatial domain that this approach holds is also verified for longer time series, implying that the simplistic approach may be used as a fallback for TC studies when reliable atmospheric temperature profiles before the satellite-era, at remote regions, are unavailable for evolved models. As a first step, we have used wavelet analyses on our output using ERSST.V3.b, individually for all the basins that provided us with the frequency of the V_{maxNw} signals and their associated time periods. The major known trends were found to be identified from this simplistic approach, which is encouraging. Whereas the outputs of wavelet spectrum analysis show the frequency vs. time pattern of V_{maxNw} , it does not provide a clear picture of the temporal behaviour. Therefore, as a second step, time series variation of V_{maxNw} is shown for the corresponding basins.

A.2.1 Patterns in the V_{maxNw}

Making use of V_{maxNw} to understand these variations in the TC structure over a long period of one and a half century could be of interest to climate scientists especially in detecting their cause and effect relationship and its variation with the changing climate Continuous wavelet power spectra for V_{maxNw} in different basins are plotted here for further analyses. The black contours on Figures (A.10) through (A.14) represent the 5% significance level against the red noise and the cone of influence demarcates the region where edge effects come to into effect.

A.2.1.1 North Indian Ocean

Figure(A.10) plots the power spectrum in the North Indian Ocean that shows high power in 6 year band during 1877 and a 5-year cycle in 1901. The two elongated bands (contoured in black) range between $2-6$ years. After these two bands, we can observe a lull period and then a cycle between 3-4 years during 1943, followed by a similar significant cycle around 1984 and again during 1988. All these bands show highest power around 5 and 3 years that may be associated with the El-Niño-Southern Oscillation (ENSO) in the Northwest Pacific and dormant Indian Ocean Dipole cycle, respectively.

A.2.1.2 South West Pacific Ocean

The continuous wavelet transform of V_{maxNw} in the Southwest Pacific is shown in Figure(A.11). Cyclic patterns in the wavelet power are clearly observed in the V_{maxNw} series. A significant peak in the 2-9 years cycle is apparent around 1954. This cycle of 9 years may coincide with the Pacific Decadal Oscillations (PDO) which spans 8-12 years period. About 4 years cycle is also seen around 1972. Another significant cycle possesses a period of 3-7 years during 1910. These oscillations may coincide with the ENSO cycle of 3-7 years (needs further investigation).

A.2.1.3 North Atlantic Ocean

The continuous wavelet power spectrum in the North Atlantic is illustrated in Figure(A.12). A significant peak in the 5 years band around 1934 is apparent. The

wavelet spectrum also shows high power with the periodicity of 2-3 years which is widespread and show significant but intermittent occurrences at a difference of about 8-10 years.

A.2.1.4 Northwest Pacific

The Figure(A.13) presents the continuous wavelet power spectrum of V_{maxNw} in the Northwest Pacific which shows a significant cycle of 8 years around 1950 and may be related to the Pacific Decadal Oscillations (PDO) that show up around 1916. Cycles of 2-3 years are widespread during the considered period of 161 years from 1854 to 2014.

A.2.1.5 Southern Indian Ocean

The Figure (A.14) exhibits the continuous wavelet power spectrum of V_{maxNw} in the South Indian Ocean. The figure suggests the occurrence of very few cycles. Most of the power of the signal appears to be concentrated at longer duration cycles (at the bottom of the cone), which, however, are not discussed here and detailed analysis is suggested for this region. The most dominant cycle is of 3 years which occurs around 1991, 1971 and 1891.

A.2.2 Time series trends

A.2.2.1 North Indian Ocean

The North Indian Ocean looks like an active region accommodating various intense tropical storms since early 1990, Figure (A.15). Although there was a comparatively dormant period during 1895 to 1990, a dramatic rise is observed then after.

A.2.2.2 South West Pacific

Simulated TC wind speed V_{maxNw} reveals a steep increase since 1910 until 2014 in the Southwest Pacific, Figure (A.16). A period of 161 years between 1854 to 2014 shows steady fluctuations between 67 to 70 m/s wind speed.

A.2.2.3 North Atlantic Ocean

The North Atlantic ocean seems to drift from moderately active to a dramatically active TC region, in terms of the associated destructive potential, Figure (A.17). The year 2005 and 2010 marked years of severe tropical storms, prior to 1910, which was a period of low cyclone activity.

A.2.2.4 North West Pacific

Graph of V_{maxNw} in the Northwest Pacific, Figure (A.18), shows that there has been an interesting long-term cyclone of rise and fall between 1854 to 1980 and thereafter, the TC strengthened sharply. Least active year in terms of TC strength was, 1919.

A.2.2.5 South Indian Ocean

Trends in V_{maxNw} in the South Indian Ocean, Figure(A.19), show a lull period between 1854 to 1940 followed by a year of a sharp rise and then fall. V_{maxNw} since 1970 onwards illustrates a sharp rise from 59 m/s to 63 m/s.

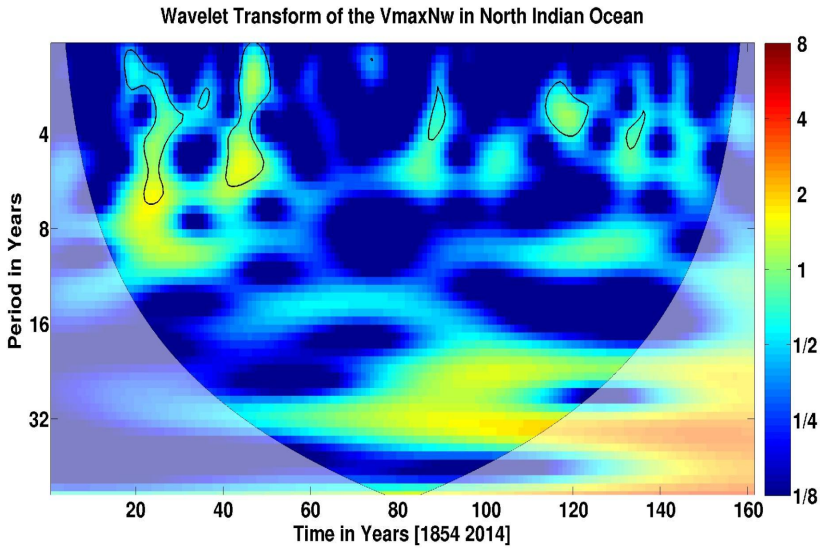

FIGURE A.10: Wavelet power spectrum of VmaxNew in the North Indian Ocean highlighting temporal patterns of occurrence of maximum wind speeds.

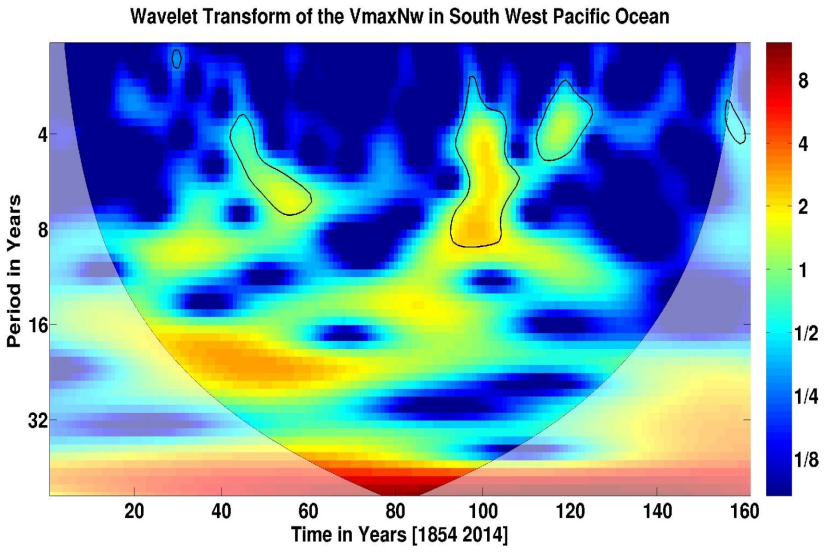

FIGURE A.11: Wavelet power spectrum of VmaxNew in the South West Pacific Ocean highlighting temporal patterns of occurrence of maximum wind speeds.

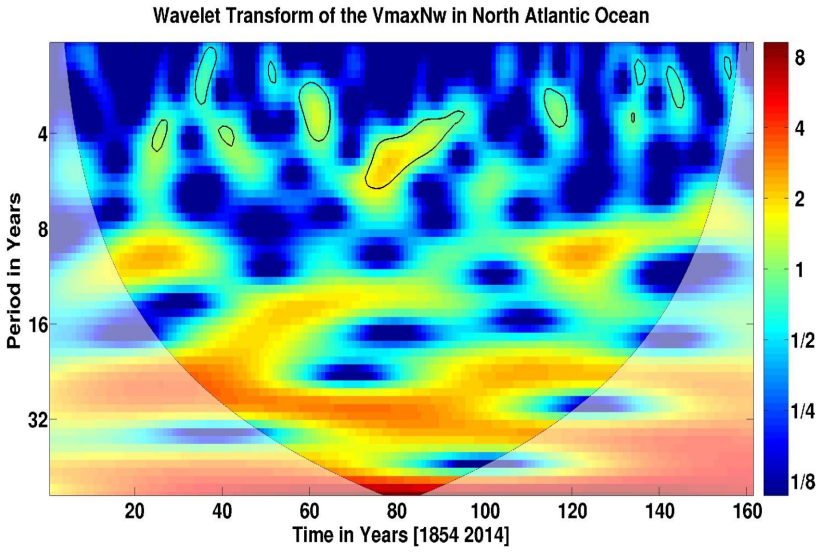

FIGURE A.12: Wavelet power spectrum of VmaxNew in the North Atlantic Ocean highlighting temporal patterns of occurrence of maximum wind speeds.

A.3 Supplementary Figures from time series analysis

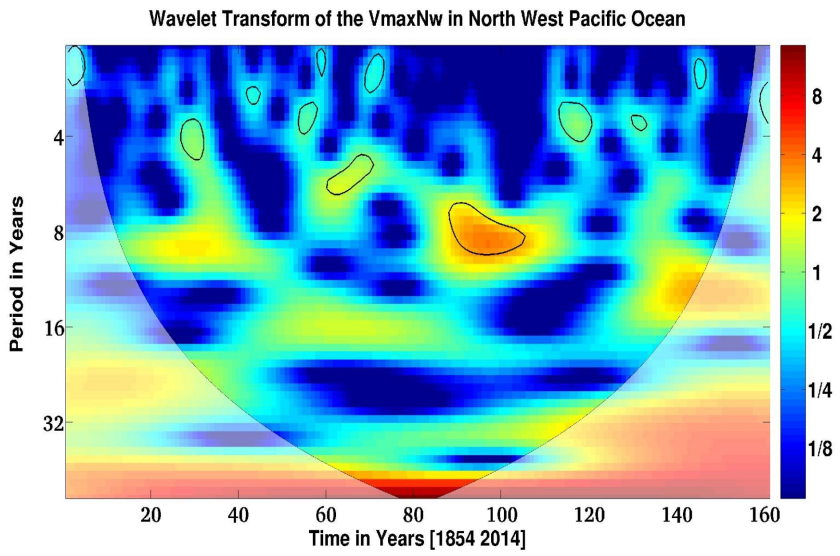

FIGURE A.13: Wavelet power spectrum of VmaxNew in the North West Pacific Ocean highlighting temporal patterns of occurrence of maximum wind speeds.

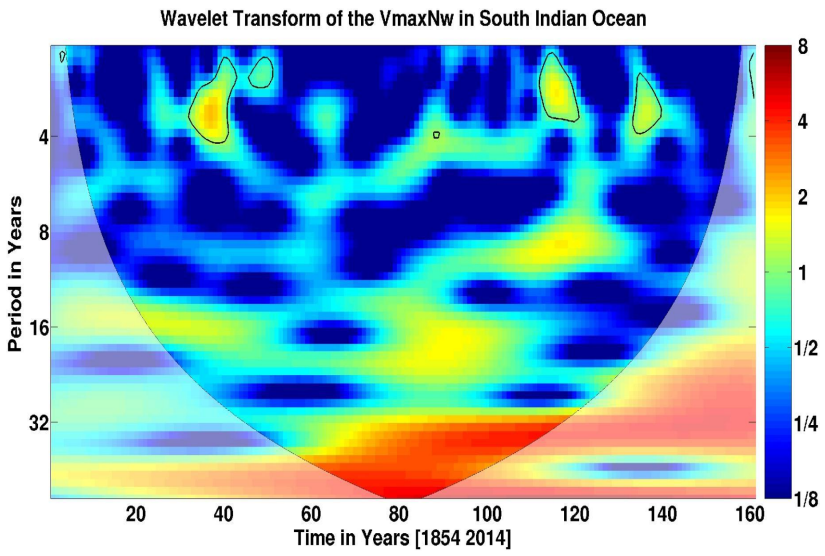

FIGURE A.14: Same as in Figure (A.13) but for the Southern Indian Ocean.

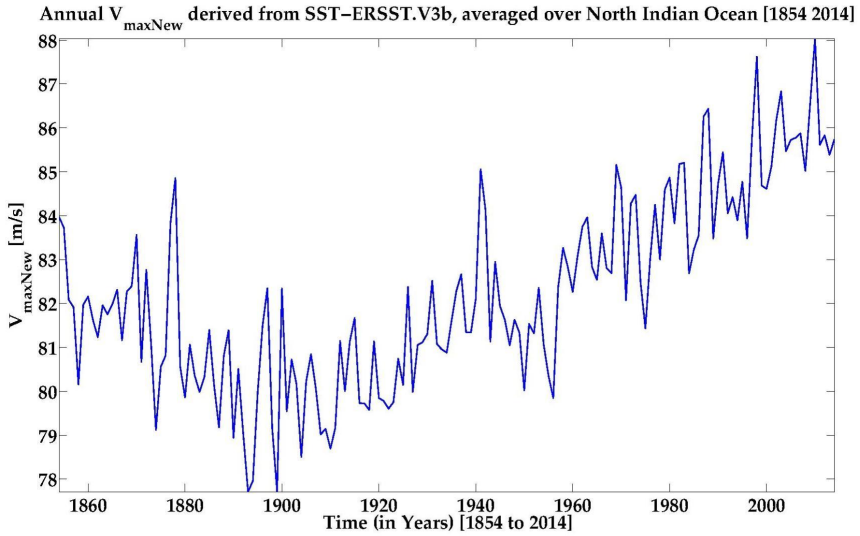

FIGURE A.15: Time series of Simulated TC wind speed VmaxNew in the North Indian Ocean

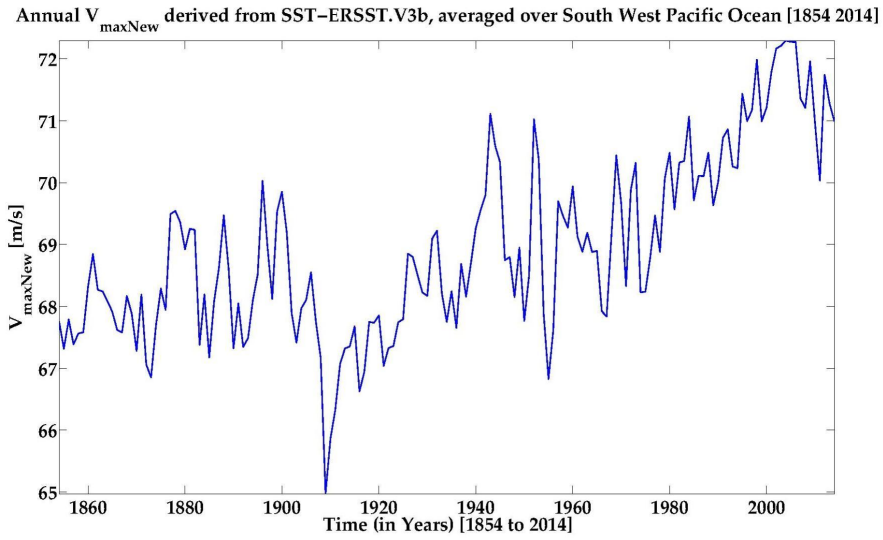

FIGURE A.16: Same as in Figure (A.15) but for the Southern West Pacific.

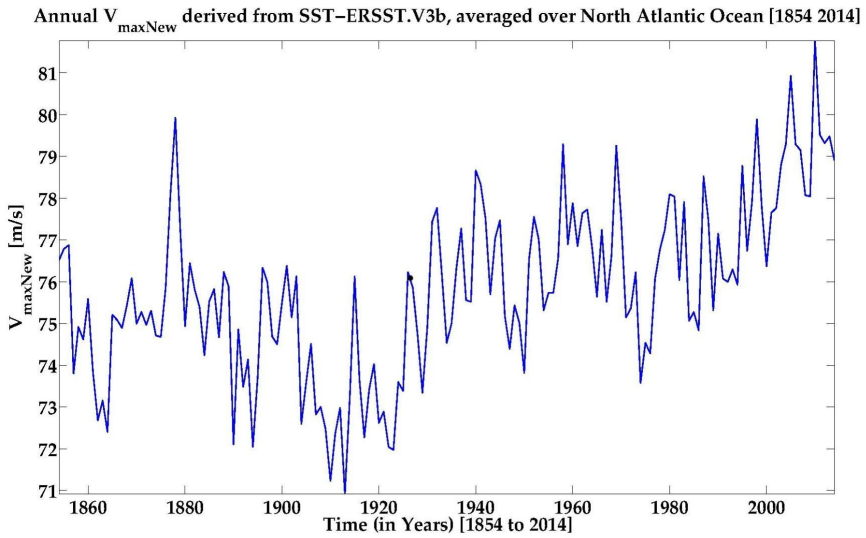

FIGURE A.17: Time series of simulated TC wind speed VmaxNew in the North Atlantic Ocean

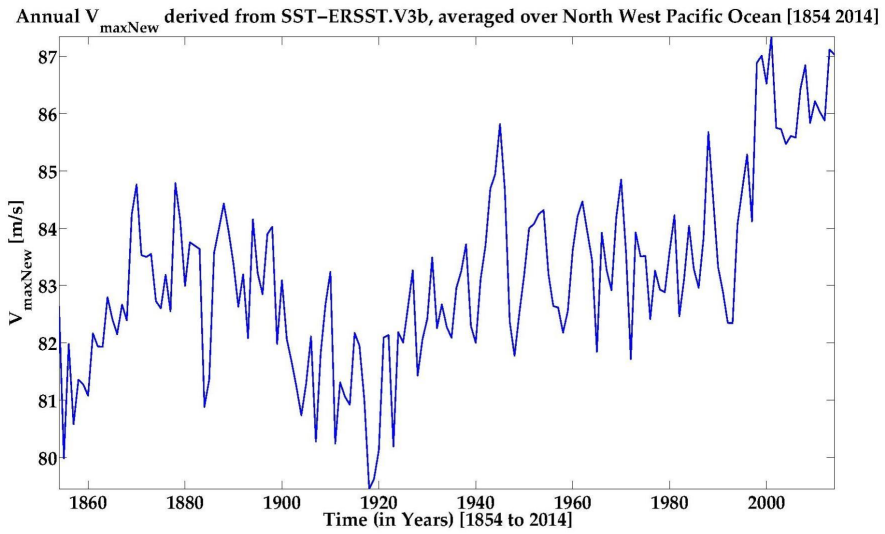

FIGURE A.18: Time series of simulated TC wind speed VmaxNew in the North West Pacific Ocean

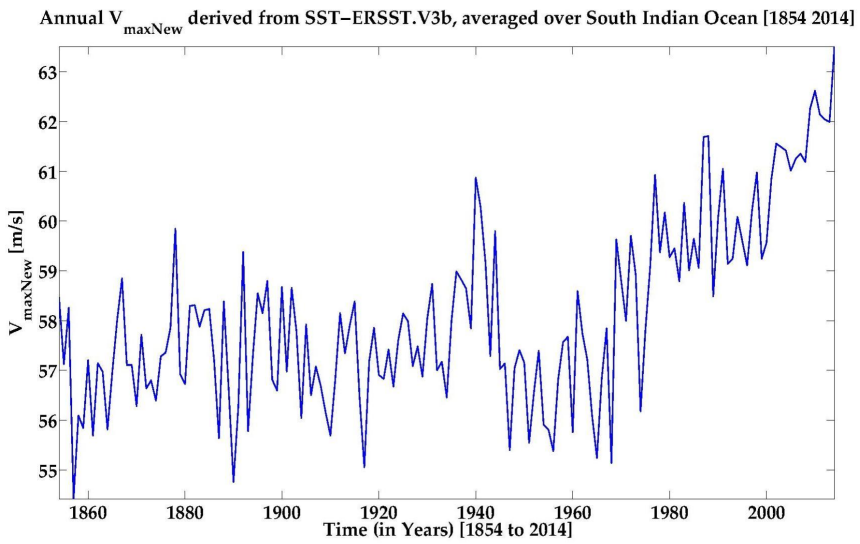

FIGURE A.19: Time series of simulated TC wind speed VmaxNew in the South Indian Ocean

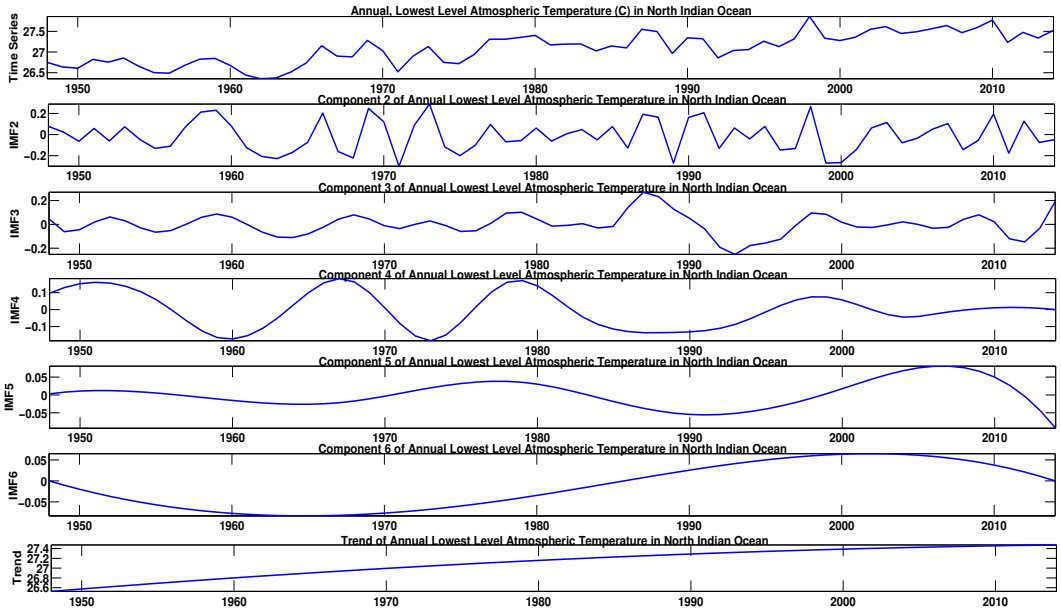

FIGURE A.20: EEMD of the AT in the North Indian Ocean.

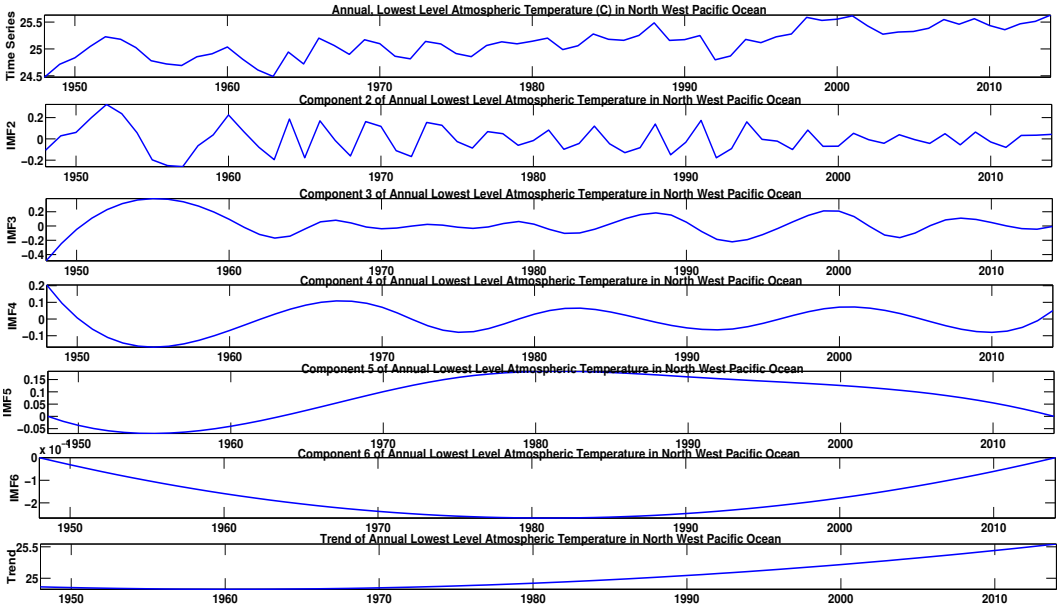

FIGURE A.21: EEMD of the AT in the North West Pacific Ocean.

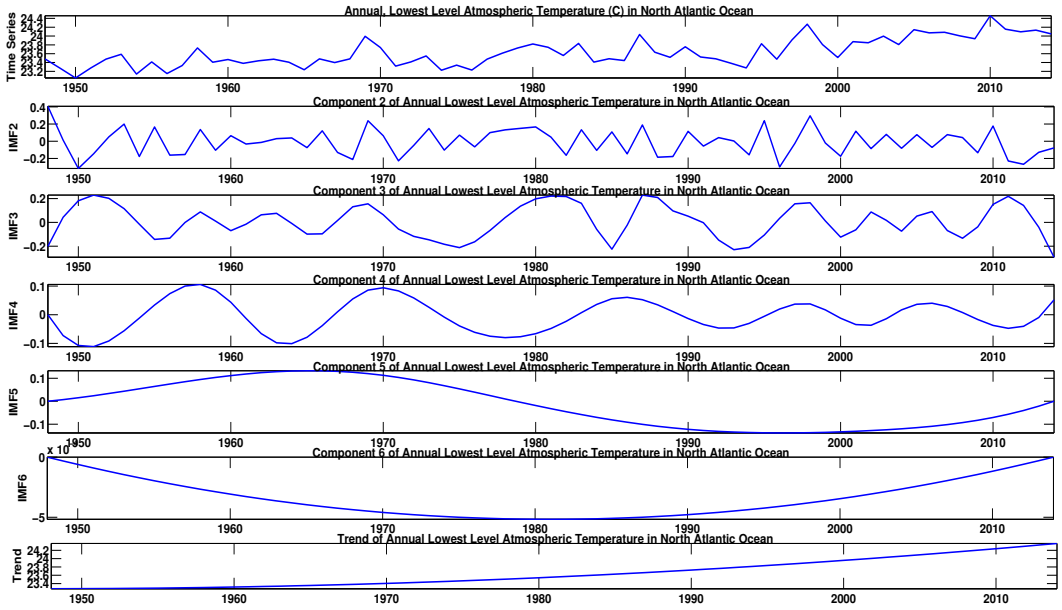

FIGURE A.22: EEMD of the AT in the North Atlantic Ocean.

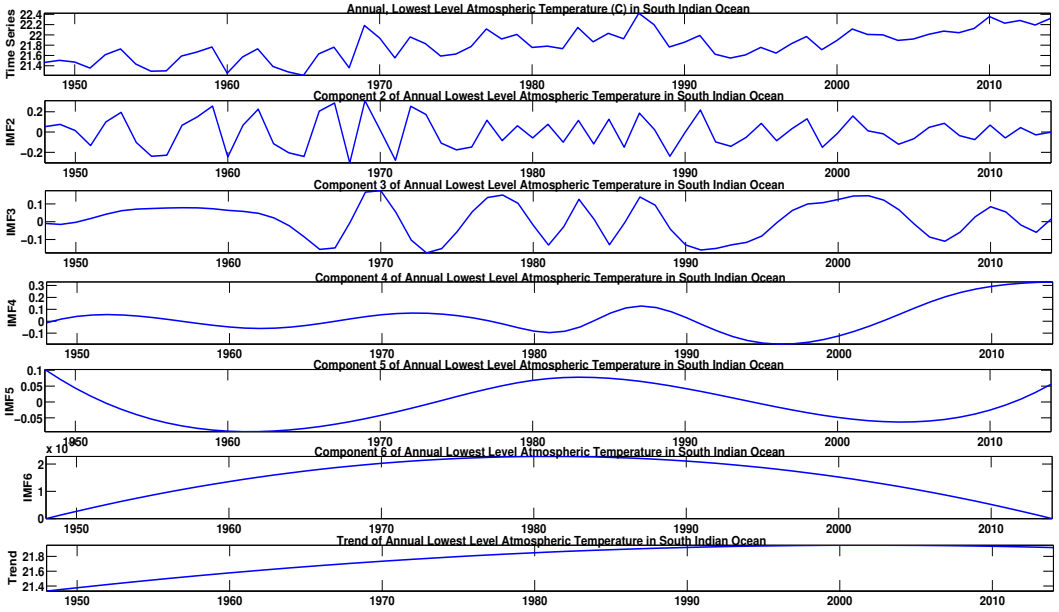

FIGURE A.23: EEMD of the AT in the South Indian Ocean.

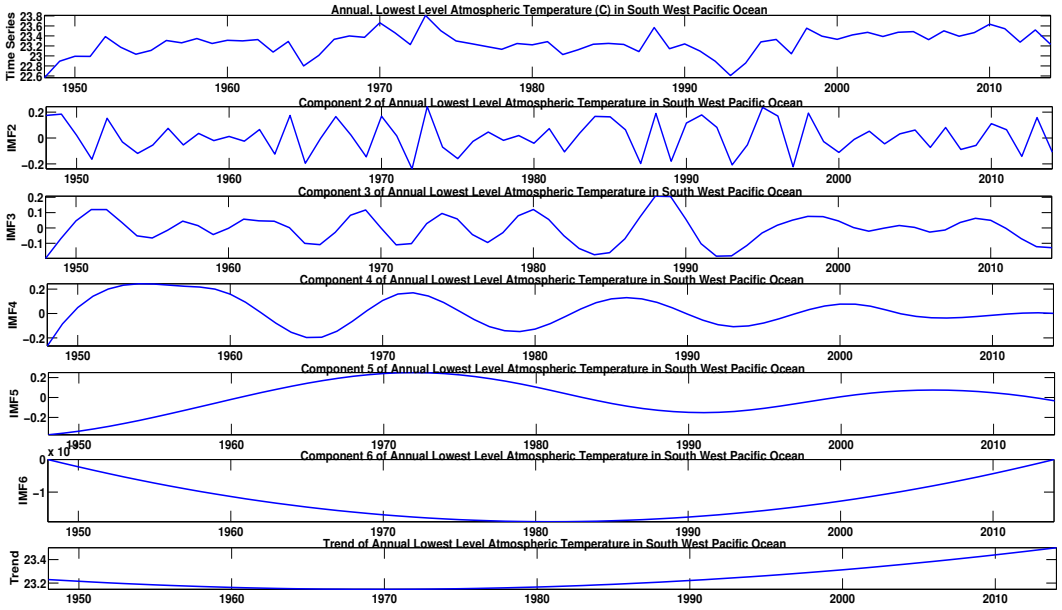

FIGURE A.24: EEMD of the AT in the South West Pacific Ocean.

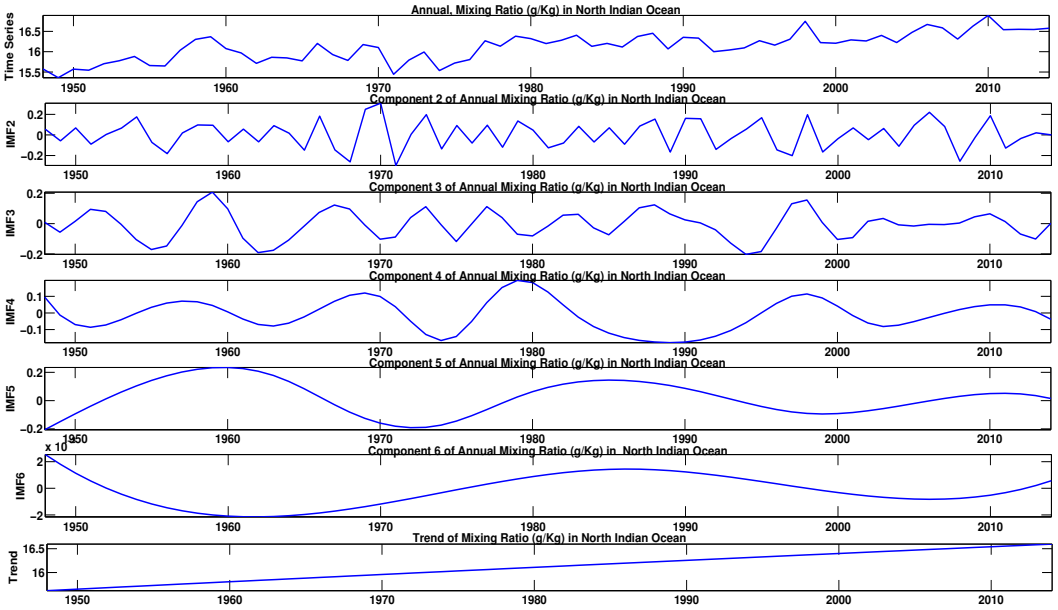

FIGURE A.25: EEMD of the MR in the North Indian Ocean.

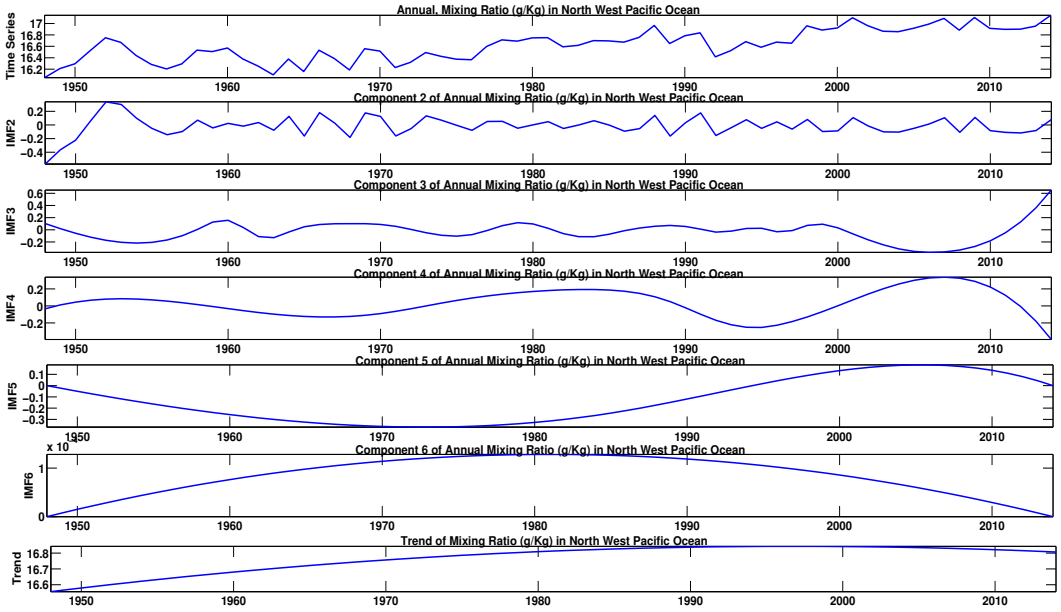

FIGURE A.26: EEMD of the MR in the North West Pacific Ocean.

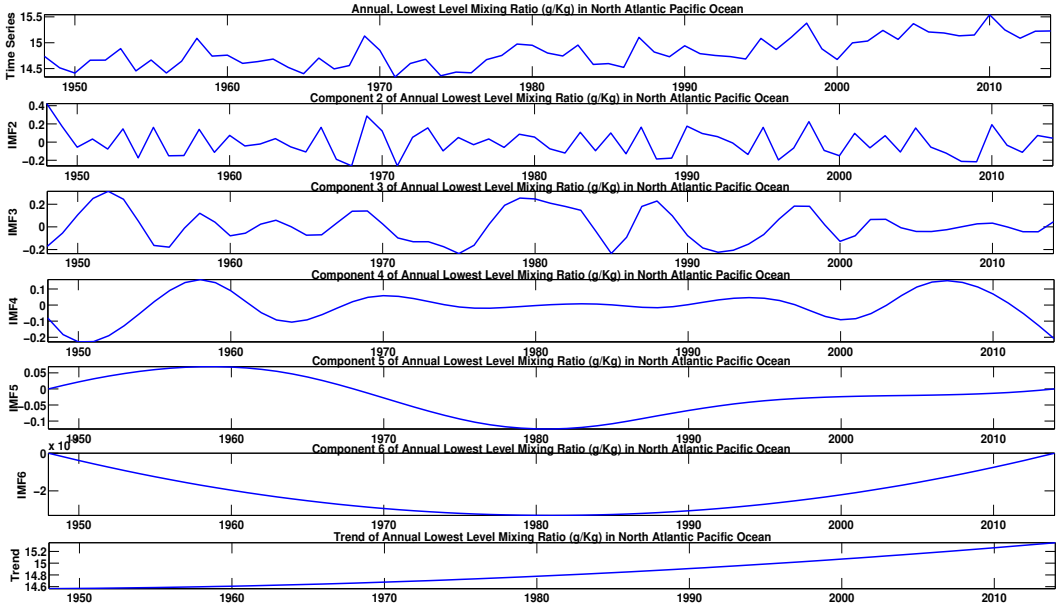

FIGURE A.27: EEMD of the MR in the North Atlantic Ocean.

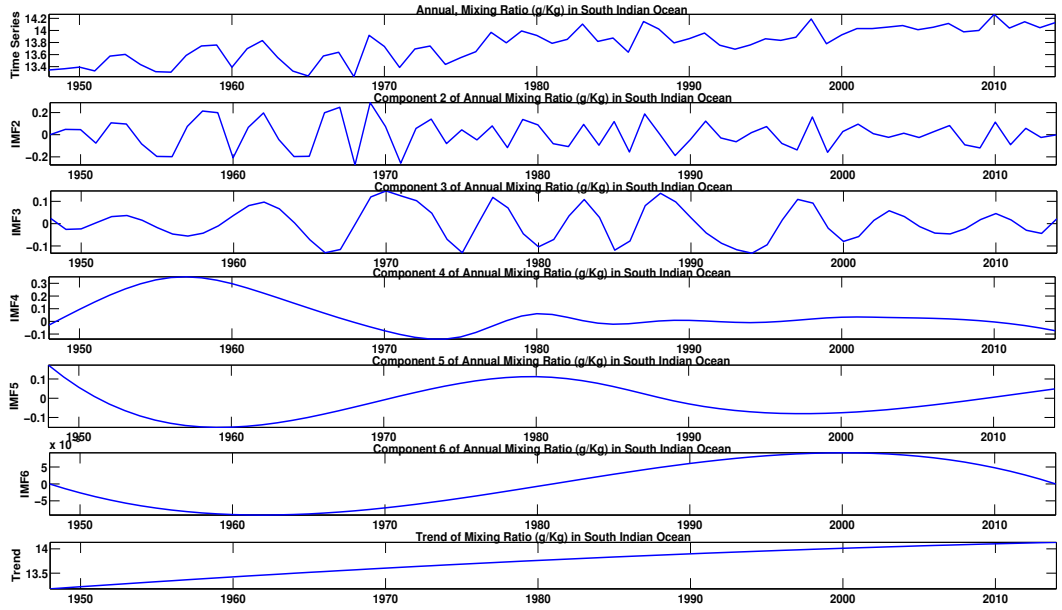

FIGURE A.28: EEMD of the MR in the South Indian Ocean.

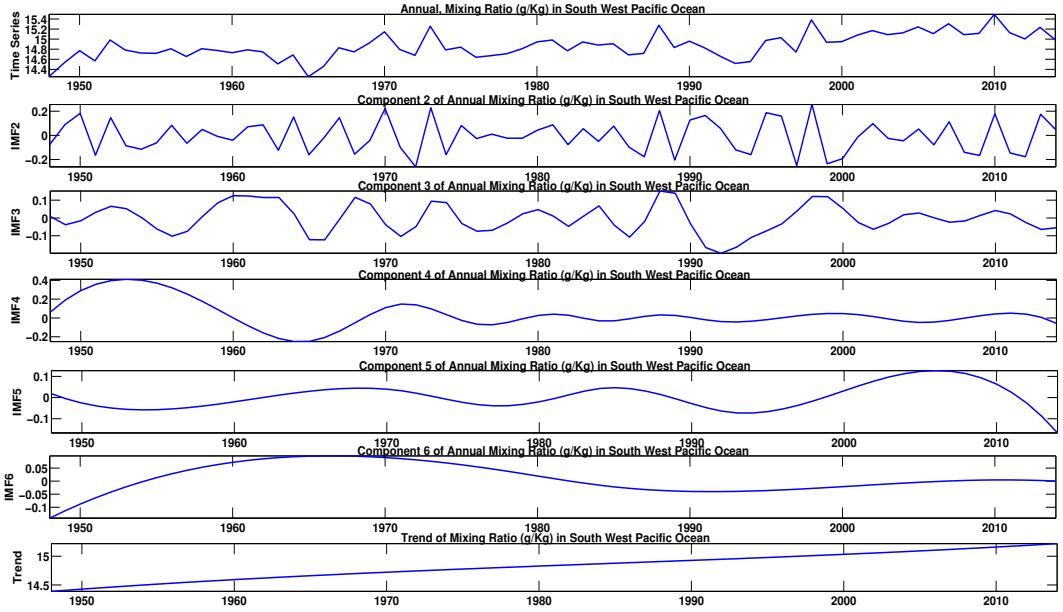

FIGURE A.29: EEMD of the MR in the South West Pacific Ocean.

Bibliography

Program COMET. https://www.meted.ucar.edu/tropical/textbook_2nd_edition/navmenu.php?tab=9&page=4.1.2, 2011.

Le Treut, R Somerville, U Cubasch, Y Ding, C Mauritzen, A Mokssit, T Peterson, M Prather, D Qin, M Manning, Z Chen, M Marquis, K B Averyt, and M Tignor. Historical overview of climate change science. In *Earth*, volume Chapter 1, pages 93–127. MeteoSat, 2007. ISBN 9780521880091. doi: 10.1016/j.soilbio.2010.04.001. URL http://www.meteosat.com/ipcc4/Ch01_SOD_Text_TSU_FINAL.pdf.

T.M. Smith, Reynolds R.W., C. Peterson Thomas, and Lawrimore Jay. Improvements to noaaś historical meprged land-ocean surface temperature analysis (1880-2006). *Journal of Climate*, 15, 2007.

COBE-NOAA. Cobe sea surface temperature analysis, provided by the noaa/esrl/psd, boulder, colorado, usa. http://www.esrl.noaa.gov/psd/data/gridded/data.cobe.html, 2015.

NOAA. Noaa optimum interpolation (oi) sst v2 data provided by the noaa/oar/esrl psd, boulder, colorado, usa, last accessed on 2014. http://www.esrl.noaa.gov/psd/data/gridded/data.noaa.oisst.v2.html, 2014.

William M. Connolley. *sst* errors in hadcm3 as when compared with era-15 (annual mean). https://en.wikipedia.org/wiki/General_Circulation_Model, June, 2005.

B. I. Miller. On the maximum intensity of hurricanes. *J. Meteor.*, 15:184–195, 1958.

G.J. Holland. The maximum paential intensity of tropical cyclones. *Journal Atmospheric Science*, 54:2519–2541, 1997a.

K. A. Emanuel. An air-sea interaction theory for tropical cyclones. part ii: Steady-state maintenance. *J. Atmos. Sci.*, 43:585–604, 1986.

K. A. Emanuel. Sensitivity of tropical cyclones to surface exchange coefficients and a revised steady-state model incorporating eye dynamics. *J. Atmos. Sci.*, 52:3969–3976, 1995.

Robert Mendelsohn, Emanuel Kerry, Chonabayashi Shun, and Laura Bakkensen. The impact of climate change on global tropical cyclone damage. *Nature climate change*, page 205–209, 2012. doi: 10.1038/nclimate1357.

Kevin J.E. Walsh, John L. McBride, Philip J. Klotzbach, Sethurathinam Balachandran, Suzana J. Camargo, Greg Holland, Thomas R. Knutson, James P. Kossin Tsz cheung Lee, Adam Sobel, and Masato Sugi. Tropical cyclones and climate change. *WIREs Clim Change 2015*, 2015. doi: 10.1002/wcc.371.

Robert Mendelsohn, Kerry Emanuel, Shun Chonabayashi, and Laura Bakkensen. The impact of climate change on global tropical cyclone damage. *Nature Climate Change*, January 2012. doi: doi:10.1038/nclimate1357.

Roger A. Pielke, Joel Gratz, Christopher W. Landsea, Douglas Collins, Mark A. Saunders, and Rade Musulin. Normalized Hurricane Damage in the United States: 1900–2005, 2008. ISSN 1527-6988.

Kerry Emanuel. Increasing destructiveness of tropical cyclones over the past 30 years. *Nature*, 436(7051):686–688, 2005a. ISSN 0028-0836.

R.A. Anthes. Tropical cyclones: Their evolution, structure and effects. *Meteor. Monogr., Amer. Meteor. Soc.*, 41, 1982.

M. Bister and K. A. Emanuel. Dissipative heating and hurricane intensity, 1998. ISSN 0177-7971.

JL Evans and IG Watterson, 1992.

A Henderson Sellers. Tropical cyclones and global climate change: A post-ipcc assessment. *Bull. Amer. Meteor. Soc.*, 79:19–38, 1998.

A Henderson Sellers and N Holbrook. Na. *Monthly Weather Review, journals.ametsoc.org*, 2000.

NHC. National hurricane center(nhc) report. http://www.earthlyissues.com/hurricanes.htm, 2014.

Kerry Emanuel. http://wind.mit.edu/~emanuel/geosys/node1.html#eq1, 2005b.

Philip J. Klotzbach. The madden–julian oscillation's impacts on worldwide tropical cyclone activity. *AMS*, 2014. doi: https://doi.org/10.1175/JCLI-D-13-00483.1.

Harry F. Hawkins and Stephen M. Imbembo. The Structure of a Small, Intense Hurricane—Inez 1966, 1976. ISSN 0027-0644.

Jia-Yuh Yu, Chou Chia, and Ping-Gin Chiu. A revised accumulated cyclone energy index. *GRL*, 36, 2009. doi: DOI:10.1029/2009GL039254.

Arctic Climatology and Meteorology. Definition for cyclogenesis, 2006.

William M. Gray. Global View Of The Origin Of Tropical Disturbances And Storms, 1968. ISSN 0027-0644.

S. J. Camargo, Sobel A. H., Barnston A. G., and P. J. Klotzbach. The influence of natural climate variabiility on tropical cyclones, and seasonal forecasts of tropical cyclone activity. in global perspectives on tropical cyclones: From science to mitigation. *World Scientific Pubslishing Co.*, page 325–360, 2010.

K. Tory and W. Frank. *Tropical cyclone formation. In Global Perspectives on Tropical Cyclones: From science to mitigation.* World Scientific Pubslishing Co., 2010.

T Palmen. On the formation and structure of tropical cyclones., 1948a.

Kopal Arora and Prasanjit Dash. Towards dependence of tropical cyclone intensity on sea surface temperature and its response in a warming world. *Climate*, 4, 2016. doi: doi:10.3390/cli4020030.

J.J. Cione. Ams 30th conference on hurricanes and tropical meteorology, ponte vedra, fl, 15-20 april 2012, 2012.

Stan Goldenberg. What is an extra-tropical cyclone?, frequently asked questions: Hurricanes, typhoons and tropical cyclones., 2008.

W.M. Gray. Tropical cyclone genesis. *University of Colorado, Atmospheric science*, 234:26–38, 1975.

Chris Landsea. How do tropical cyclones form?, frequently asked questions: Hurricanes, typhoons and tropical cyclones., 2006.

Lixion A. Avila and Richard J. Pasch. Atlantic Tropical Systems of 1993, 1995. ISSN 0027-0644.

Lisa M. Briegel and William M. Frank. Large-Scale Influences on Tropical Cyclogenesis in the Western North Pacific, 1997. ISSN 0027-0644.

G. J. Goni, P. Black, and J. Trinanes. Using satellite altimetry to identify regions of hurricane intesification, 2003.

University of Illinois. Hurricanes: a tropical cyclone with winds greater than 64 knots. http://ww2010.atmos.uiuc.edu/(Gh)/guides/mtr/hurr/grow/home.rxml, 2006.

M.E Nicholls and R. A. Pielke. A numerical investigation of the effect of vertical wind shear on tropical cyclone intensification. *Conference on Hurricanes and Tropical Meteorology of the American Meteorological Society. Colorado State University*, pages 339–341, April 1995.

Tang Brian and Kerry Emanuel. Midlevel Ventilation Constraint on Tropical Cyclone Intensity. *J. Atmos. Sci.*, 67:1817–1830, 2010. doi: doi:10.1175/2010JAS3318.1.

Linda A. Paterson, Barry N. Hanstrum, Noel E. Davidson, and Harry C. Weber. Influence of Environmental Vertical Wind Shear on the Intensity of Hurricane-Strength Tropical Cyclones in the Australian Region, 2005. ISSN 0027-0644.

Fuqing Zhang and Dandan Tao. Effects of vertical wind shear on the predictability of tropical cyclones. *Journal of the Atmospheric Sciences*, 70: 975–983, 2013. ISSN 0022-4928. doi: 10.1175/JAS-D-12-0133.1. URL http://journals.ametsoc.org/doi/abs/10.1175/JAS-D-12-0133.1.

Smith, Roger K., Montgomery, Michael T., Thomsen, and Gerald L. Sensitivity of tropical-cyclone models to the surface drag coefficient in different boundary-layer schemes. *Quarterly Journal of the Royal Meteorological Society*, 140(680):792–804, April 2014. ISSN 00359009. doi: 10.1002/qj.2057. URL http://doi.wiley.com/10.1002/qj.2057.

D. Harvey, J Gregory, M Hoffert, A Jain, M Lal, R Leemans, S Raper, T Wigley, and J de Wolde. An introduction to simple climate models used in the ipcc second assessment report. *IPCC Technical Paper II: Intergovernmental Panel on Climate Change, Geneva.*, page 47, 1997.

Matthew Collins, Ben B B Booth, B Bhaskaran, Glen R Harris, James M Murphy, David M H Sexton, and Mark J Webb. Climate model errors, feedbacks and forcings: a comparison of perturbed physics and multi-model ensembles. *Climate Dynamics*, 36(9-10):1737–1766, 2011. ISSN 0930-7575.

Kenneth Knapp R, Michael C Kruk, David H Levinson, Howard J Diamond, and Charles J Neumann. The international best track archive for climate stewardship (ibtracs) unifying tropical cyclone data. *Bulletin of the American Meteorological Society*, 91:363–376, 2010.

Amy Solomon and Matthew Newman. Reconciling disparate twentieth-century indo-pacific ocean temperature trends in the instrumental record. *Nature Climate Change*, 2(9):691–699, 2012.

Clara Deser, Adam S Phillips, and Michael A Alexander. Twentieth century tropical sea surface temperature trends revisited. *Geophysical Research Letters*, 37(10), 2010. ISSN 1944-8007.

N A Rayner, D E Parker, E B Horton, C K Folland, L V Alexander, D P Rowell, E C Kent, and A Kaplan. Global analyses of sea surface temperature, sea ice, and night marine air temperature since the late nineteenth century. *Journal of Geophysical Research: Atmospheres (1984–2012)*, 108(D14), 2003. ISSN 2156-2202.

Amy Solomon, Lisa Goddard, Arun Kumar, James Carton, Clara Deser, Ichiro Fukumori, Arthur M Greene, Gabriele Hegerl, Ben Kirtman, and Yochanan Kushnir. Distinguishing the roles of natural and anthropogenically forced decadal climate variability. *Bulletin of the American Meteorological Society*, 92 (2), 2011. ISSN 0003-0007.

G. A. Schmidt, J. H. Jungclaus, C. M. Ammann, E. Bard, P. Braconnot, T. J. Crowley, G. Delaygue, F. Joos, N. A. Krivova, R. Muscheler, B. L. Otto-Bliesner, J. Pongratz, D. T. Shindell, S. K. Solanki, F. Steinhilber, and L. E A Vieira. Climate forcing reconstructions for use in pmip simulations of

the last millennium (v1.1). *Geoscientific Model Development*, 5(1):185–191, 2012. ISSN 1991959X. doi: 10.5194/gmd-5-185-2012.

Donnera Leo J., Wymana Bruce L., Hemlera Richard S., Horowitza Larry W., Yi Minga, Zhaob Ming, Golaza Jean-Christophe, Paul Ginouxa, Lina S.-J., Schwarzkopfa M. Daniel, Austinb John, Alakac Ghassan, Cooked William F., Delwortha Thomas L., Freidenreicha Stuart M., Gordona C. T., Griffiesa Stephen M., Helda Isaac M., Hurlina William J., Kleine Stephen A., Knutsona Thomas R., Langenhorstd Amy R., Leed Hyun-Chul, Linb Yanluan, Magif Brian I., Malyshevf Sergey L., Millyg P. C. D., Naikd Vaishali, Natha Mary J., Pincush Robert, Ploshaya Jeffrey J., V. Ramaswamya, Semana Charles J., Shevliakovaf Elena, Sirutisa Joseph J., Sterna William F., Ronald J. Stouffera, Wilsona R. John, Wintona Michael, Wittenberga Andrew T., and Zenga Fanrong. The dynamical core, physical parameterizations, and basic simulation characteristics of the atmospheric component am3 of the gfdl global coupled model cm3. *AMS*, 2011. doi: http://dx.doi.org/10.1175/2011JCLI3955.1.

Griffies, Winton Stephen M., Michael, J. Donner Leo, Horowitz Larry W., M. Downes Stephanie, Farneti Riccardo, Gnanadesikan Anand, Hurlin William J., Lee Hyun-Chul, Liang Zhi, Palter Jaime B., Samuels Bonita L., Wittenberg Andrew T., Wyman Bruce L., Yin Jianjun, and Zadeh Niki. The gfdl cm3 coupled climate model: Characteristics of the ocean and sea ice simulations. *AMS*, 2011. doi: http://dx.doi.org/10.1175/2011JCLI3964.1.

Carl Schreck. The climate data guide: Ibtracs: Tropical cyclone best track data. https://climatedataguide.ucar.edu/climate-data/ibtracs-tropical-cyclone-best-track-data., 2013.

Jack Williams. Hurricane scale invented to communicate storm danger. *USA Today*, 2007.

Mark Saunders and Adam Lea. Summary of 2006 nw pacific typhoon season and verification of authors' seasonal forecasts" (pdf). tropical storm risk. *Archived from the original*, 2007.

Kerry Emanuel. Increasing destructiveness of tropical cyclones over the past 30 years. *Nature*, 436 (7051): 686–8, 2005c. doi: 10.1038/nature03906.

V. Misra. The track integrated kinetic energy of atlantic tropical cyclones. *AMS, J Atmos.*, 2013. doi: 10.1175/MWR-D-12-00349.1.

Powell Mark D and Reinhold Timothy A. The maximum sustained surface wind speed indicator. *BAMS*, 2007.

V. Misra, S. DiNapoli, and M. Powell. The track integrated kinetic energy of atlantic tropical cyclones, 2013.

Kalnay. The ncep/ncar 40-year reanalysis project. *Bull. Amer. Meteor. Soc.*, 77: 437–470, 1996. URL http://www.esrl.noaa.gov/psd/data/gridded/data.ncep.reanalysis.derived.html.

NOAA/NCAR Reanalysis. Specific humdity ncep/ncar reanalysis derived data provided by the noaa/oar/esrl psd, boulder, colorado, usa, from their web site, 2014. URL http://www.esrl.noaa.gov/psd/data/gridded/data.ncep.reanalysis.derived.html.

I.N. Levine. *Physical Chemistryand Phase rule, phase diagrams*, volume 4th ed. McGraw-Hill, New York, 1995.

Reynolds R.W., N.A. Rayner, T.M. Smith, and D.C. Stokes & W. Wang. An improved in situ and satellite sst analysis for climate. *J. Climate*, 2001.

Martin H Trauth. *MATLAB Recipies for Earth Sciences (3Ed)*. Springer. Springer, 2010. ISBN 978-3-642-12761-8.

NE. Huang, Z. Shen, Long SR, MLC Wu, and Shih NH. The empirical mode decomposition and the hilbert spectrum for nonlinear and non-stationary time series analysis. *Proceedings of the Royal Society of London Series A-Mathematical Physical and Engineering Sciences*, 454, 1998.

K. A. Emanuel. Environmental factors affecting tropical cyclone power dissipation. *Journal of Climate*, 20:5497–5509, 2007.

M. Bister and K. A. Emanuel. Low frequency variability of tropical cyclone potential intensity interannual to interdecadal variability. *J. Geophys. Res.*, 107:4801, 2002. doi: 10.1029/2001JD000776.

K. A. Emanuel. The maximum intensity of hurricanes. *J. Atmos. Sci.*, 45: 1143–1155, 1988.

J. Simpson, Elizabeth A. Ritchie, G. J. Holland, J. Halverson, and S. Stewart. Mesoscale Interactions in Tropical Cyclone Genesis. *Monthly Weather Review*, 125(10):2643–2661, 1997. ISSN 0027-0644. doi:

10.1175/1520-0493(1997)125lt2643:MIITCGgt2.0.CO;2. URL http://journals.ametsoc.org/doi/abs/10.1175/1520-0493(1997)125lt2643:MIITCGgt2.0.CO;2.

R. & K. A. Emanuel Rotunno. An air-sea interaction theory for tropical cyclones. part ii: Evolutionary study using a nonhydrostatic axisymmetric numerical model. *J. Atmos. Sci.*, 44:542–561, 1987.

J. Persing and M. T. Montgomery. Is environmental cape inportant in the determination of maximum possible hurricane intensity? *J. Atmos. Sci.*, 62: 542–550, 2005.

M. DeMaria and J. Kaplan. Sea surface temperature and the maximum intensity of atlantic tropical cyclones. *J. Climate*, 7:1324–1334, 1994.

Z Zeng, Wang Y, and Wu C-C. Environmental dynamical control of tropical cyclone intensity—an observational study. *Mon. Wea. Rev.*, 135:38–59, 2007.

L. D. Whitney and J. S. Hobgood. The relationship between sea surface temperatures and maximum intensities of tropical cyclones in the eastern north pacific. *J. Climate*, 10:2921–2930, 1997.

W. Shen, R. E. Tuleya, and I. Ginis. A sensitivity study of the thermodynamic environment on gfdl model hurricane intensity: Implications for global warming. *Climate*, 13:109–121, 2000.

G. J. Holland. The maximum potential intensity of tropical cyclones. *J. Atmos. Sci.*, 54:2519–2541, 1997b.

A. R. Saunders, M. A.; Harris. Statistical evidence links exceptional 1995 atlantic hurricane season to record sea warming. *Geophysical Research Letters*, pages 1255–1258, 1997.

T. Michael, Roger Montgomery, Smith K., and Nguyen Sang V. Sensitivity of tropical cyclone models to the surface drag coefficient. *Q.J.R. Meteorol. Soc.*, 136:1945–1953, 2010.

Mark D Powell, Peter J Vickery, and Timothy A Reinhold. Reduced drag coefficient for high wind speeds in tropical cyclones. *Nature*, 422(6929): 279–283, 2003. ISSN 00280836. doi: 10.1038/nature01481.

K. A. Emanuel. Increasing destructiveness of tropical cyclones over the past 30 years. *Nature Letters*, pages –, 2005d. doi: doi:10.1038/nature03906.

E. Palmen. On the formation and structure of tropical hurricanes. *Geophysica*, 3: 26–38, 1948b.

K A Emanuel. The power of a hurricane: An example of reckless driving on the information superhighway. *Weather*, 54:107–108, 1998.

Kerry Emanuel. A Statistical Analysis of Tropical Cyclone Intensity, 2000. ISSN 0027-0644.

A. H. Sobel, I. M. Held, and C. S Bretherton. The enso signal in tropical tropospheric temperature. *J. Clim.*, 15:2702–2706, 2002.

C. K. Folland and D. E. Parker. Correction of instrumental biases in historical sea surface temperature data. *Q. J. R. Meteorol. Soc.*, 121:319–367, 1995.

B. Efron and R. Tibshirani. *An Introduction to the Bootstrap*, volume ISBN 0-412-04231-2. Boca Raton, FL: Chapman and Hall/CRC., 1993.

T. Zhu and D. L. Zhang. The impact of the storm-induced sst cooling on hurricane intensity. *Advances in Atmospheric Sciences*, 23(1):14–22, 2006.

J. L. Davis, T. A. Herring, I. I. Shapiro, A. E. E. Rogers, and G. Elgered. Geodesy by radio interferometry: Effects of atmospheric modeling errors on estimates of baseline length. *Radio Science*, 20(6):1593–1607, 1985.

M. Bevis, S. Businger, T. Herring, C. Rocken, R. Anthes, and R Ware. Gps meteorology- remote sensing of atmospheric water vapor using the global positioning system. *Journal of Geophysical Research*, 97(D14):15787–15801, 1992.

Thomas M et. al. Smith. Improvements to noaa's historical merged land-ocean surface temperature analysis (1880-2006). *Journal of Climate*, 21(10): 2283–2296, 2008. ISSN 08948755. doi: 10.1175/2007JCLI2100.1.

R. W. Reynolds, N. A. Rayner, T. M. Smith, D. C. Stokes, and W. Q. Wang. An improved in situ and satellite sst analysis for climate. *Journal of Climate*, pages 1609–1625, 2002. doi: 15(13).

M. Martin, P. Dash, A. Ignatov, V. Banzon, H. Beggs, B. Brasnett, J.-F. Cayula, J. Cummings, C. Donlon, R. Gentemann, C.and Grumbine, S Ishizaki, E. Maturi, R. W. Reynolds, and J. Roberts-Jones. Group for high resolution sea surface temperature (ghrsst) analysis fields inter-comparisons. part 1: A ghrsst multi-product ensemble (gmpe). deep sea research part ii. *Topical Studies in Oceanography*, 77:21–30, 2012.

P. Dash, A. Ignatov, M. Martin, C. Donlon, B. Brasnett, R. W. Reynolds, V. Banzon, H. Beggs, J.F. Cayula, Y. Chao, R. Grumbine, E. Maturi, A. Harris, J. Mittaz, J. Sapper, T. M. Chin, J. Vazquez-Cuervo, E. M. Armstrong, C. Gentemann, J. Cummings, J.F. Piollé, E. Autret, J. Roberts-Jones, S. Ishizaki, J. L. Høyers, and D. Poulter. Group for high resolution sea surface temperature (ghrsst) analysis fields inter-comparisons. part 2: A ghrsst multi-product ensemble (gmpe). deep sea research part ii. *Topical Studies in Oceanography*, 77:31–43, 2012.

Sarah M. Kang and Richard Seager. Croll revisited: Why is the northern hemisphere warmer than the southern hemisphere? *Columbia University Academic Commons*, 2012. doi: https://doi.org/10.7916/D80R9XNQ. URL http://ocp.ldeo.columbia.edu/res/div/ocp/pub/seager/Kang_Seager_subm.pdf.

Ulrike Wissmeier and Roger K. Smith. Tropical cyclone convection: the effects of ambient vertical vorticity. *RMEts*, page 819, 2011. doi: DOI:10.1002/qj.

Theodore L Bergman, Adrienne S Lavine, and Frank P Incropera. Fundamentals of heat and mass transfer, 2011.

M. T. Montgomery, N. V. Sang, R. K. Smith, and J. Persing. Do tropical cyclones intensify by wishe? *Quarterly Journal of the Royal Meteorological Society*, 135(644):1697–1714, 2009.

C. W. Landsea, N. Nicholls, W. M. Gray, and L. A. Avila. Downward trends in the frequency of intense atlantic hurricanes during the past five decades. *Geophys. Res. Lett.*, 23:1697–1700, 1996.

Chan, Johnny C. L., and Jiu-en Shi. Long-term trends and interannual variability in tropical cyclone activity over the western north pacific, 1996. ISSN 0094-8276.

S. Levitus. Warming of the World Ocean, 2000. ISSN 00368075.

S. E. Strazzo, J. B. Elsner, and T. E. LaRow. Quantifying the sensitivity of maximum, limiting, and potential tropical cyclone intensity to sst: Observations versus the fsu/ coaps global climate model. *Journal of Advances in Modeling Earth Systems*, pages 1–21, 2015. doi: 10.1002/2015MS000432. URL http://scholar.google.com/scholar?hl=en&btnG=Search&q=intitle:Journal+of+Advances+in+Modeling+Earth+Systems#9.

Ming Zhao, Isaac M. Held, Shian Jiann Lin, and Gabriel A. Vecchi. Simulations of global hurricane climatology, interannual variability, and response to global warming using a 50-km resolution GCM. *Journal of Climate*, 22(24): 6653–6678, 2009. ISSN 08948755. doi: 10.1175/2009JCLI3049.1.

Thomas R Knutson and Robert E Tuleya. Impact of co2-induced warming on simulated hurricane intensity and precipitation: Sensitivity to the choice of climate model and convective parameterization. *AMS*, 2003.

Thomas R Knutson and Robert E Tuleya. Reply. *AMS*, 2005.

T.R. Knutson, Sirutis J. J, Garner S. T, Vecchi G. A, and Held I. Simulated reduction in atlantic hurricane frequency under twenty-first-century warming conditions. *Nat. Geosci.*, page 359 to 364, 2008.

Kerry Emanuel. Global warming effects on u.s. hurricane damage. *AMS*, 2011. doi: https://doi.org/10.1175/WCAS-D-11-00007.1.

Christensen Jens Hesselbjerg and Kanikicharla Krishna Kumar. Working group i contribution to the ipcc fifth assessment report climate change 2013: The physical science basis final draft underlying scientific-technical assessment https://www.ipcc.ch/pdf/assessment-report/ar5/wg1/drafts/fgd/WGIAR5_WGI-12Doc2b_FinalDraft_Chapter14.pdf, 2013.

Kerry a Emanuel. Downscaling CMIP5 climate models shows increased tropical cyclone activity over the 21st century. *Proceedings of the National Academy of Sciences of the United States of America*, 110(30):12219–24, 2013. ISSN 1091-6490. doi: 10.1073/pnas.1301293110. URL http://www.pubmedcentral.nih.gov/articlerender.fcgi?artid=3725040&tool=pmcentrez&rendertype=abstract.

Robert T. Merrill. An experiment in statistical prediction of tropical cyclone intensity change. *Noaa Technical Memorandum NWS NHC 34*, 1987. URL http://www.nhc.noaa.gov/pdf/NWS-NHC-1987-34.pdf.

James B Elsner, James P Kossin, and Thomas H Jagger. The increasing intensity of the strongest tropical cyclones. *Nature*, 455(7209):92–95, 2008. ISSN 0028-0836.

James B. Elsner, Robert E. Hodges, and Thomas H. Jagger. Spatial grids for hurricane climate research. *Climate Dynamics*, 39(1-2):21–36, 2012a. ISSN 09307575. doi: 10.1007/s00382-011-1066-5.

J. B. Elsner, J. C. Trepanier, S. E. Strazzo, and T. H. Jagger. Sensitivity of limiting hurricane intensity to ocean warmth. *Geophysical Research Letters*, 39 (17), 2012b. ISSN 00948276. doi: 10.1029/2012GL053002.

Thomas R. Knutson, Joseph J. Sirutis, Gabriel A. Vecchi, Stephen Garner, Ming Zhao, Hyeong Seog Kim, Morris Bender, Robert E. Tuleya, Isaac M. Held, and Gabriele Villarini. Dynamical downscaling projections of twenty-first-century atlantic hurricane activity: CMIP3 and CMIP5 model-based scenarios. *Journal of Climate*, 26(17):6591–6617, 2013. ISSN 08948755. doi: 10.1175/JCLI-D-12-00539.1.

Gabriele Villarini and Gabriel A. Vecchi. Projected increases in north atlantic tropical cyclone intensity from cmip5 models. *Journal of Climate*, 26(10): 3231–3240, 2013. ISSN 08948755. doi: 10.1175/JCLI-D-12-00441.1.

Shuyi S. Chen, James F. Price, Wei Zhao, Mark a. Donelan, and Edward J. Walsh. The cblast-hurricane program and the next-generation fully coupled atmosphere-wave-ocean models for hurricane research and prediction. *Bulletin of the American Meteorological Society*, 88(3):311–317, 2007. ISSN 00030007. doi: 10.1175/BAMS-88-3-311.

Abdi Herve. Partial least squares (pls) regression, 2003. ISSN 15315487.

B. Moore, WL. Gates, LJ. Mata, A. Underdal, JT Houghton, Y Ding, DJ Griggs, M Noguer, PJ van der Linden, X Dai, K Maskell, and CA (eds) Johnson. Climate change 2001: the scientific basis. contribution of working group i to the third assessment report of the intergovernmental panel on climate change, cambridge university press. *IPCC* 3rd *assessment report*, 2001.

M. Collins, B. Ben, B. Booth, B. Bhaskaran, R. Harris Glen, M. Murphy James, M. H. Sexton David, and J. Webb Mark. Climate model errors, feedbacks and forcings: a comparison of perturbed physics and multi-model ensembles. *Climate Dynamics*, 10.1007/s0038201008080, 2010.

Dominik Brunner. rh2mixr. https://svn.ssec.wisc.edu/repos/bennartz_group/LIBRARY/idl/std_libs/atmos_phys/rh2mixr.pro, 2001.

Karl E. Taylor, Ronald J. Stouffer, and Gerald A. Meehl. An overview of cmip5 and the experiment design. *AMS*, 2012.

Thomas L. Delworth, Anthony J. Broccolib, Anthony Rosatia, Ronald J. Stouffera, V. Balajic, John A. Beesleyd, and et.al William F. Cooke. Gfdl's cm2 global coupled climate models. part i: Formulation and simulation characteristics. *AMS*, 2006. doi: \url{DOI:http://dx.doi.org/10.1175/JCLI3629.1}.

Kerry Emanuel. Anthropogenic effects on tropical cyclone activity, 2006.

Sellers Henderson. Tropical cyclones and global climate change: A post-ipcc assessment. *Bulletin of the American Meteorological Society*, 19, 1998.

Montgomery M. T. and K. A. Emanuel. Air–sea enthalpy and momentum exchange at major hurricane wind speeds observed during cblast. *Journal of the Atmospheric Sciences*, 69and (11): 3197. Bibcode:2012JAtS...69.3197B., 2012. doi: doi:10.1175/JAS-D-11-0276.1.